Electronic Thesis and Dissertation Repository

4-11-2018 2:00 PM

Experimental Simulation of Density-Driven Thunderstorm Downbursts

Roghayyeh Babaei koli, *The University of Western Ontario*

Supervisor: Professor Eric Savory, *The University of Western Ontario*
A thesis submitted in partial fulfillment of the requirements for the Master of Engineering Science degree in Mechanical and Materials Engineering
© Roghayyeh Babaei koli 2018

Follow this and additional works at: https://ir.lib.uwo.ca/etd

Part of the Other Mechanical Engineering Commons

Abstract

Evaporative cooling of the precipitation within the thunderstorm cloud results in the formation of a mass of cold and dense air which moves toward the ground and after impingement turns into strong radial winds near the surface. In this study, an experimental approach was taken to investigate the downbursts. The two-fluid model was used, and the various features of the experimental setup of previous researchers were modified to incorporate the specifications of natural downbursts. First, two new release cylinders were manufactured and their capabilities in producing repeatable and symmetric outflows were examined. Then, the effects of cylinder wall design, density difference and release height on the downbursts were investigated. For the first time, the translation of storm and the velocity field of the ambient environment were considered in the experimental simulations of downbursts based on a density-driven model. In this regard, a hydraulic flume equipped with a trolley was employed.

Keywords

Co-Authorship Statement

This thesis is prepared according to the specifications of the integrated article format by the School of Graduate and Postdoctoral Studies (SGPS) at the University of Western Ontario. The co-authors of each article and their contributions are described as follows:

Chapter 2: Characterizing the Liquid Release Mechanism Performance in the Experimental Simulation of Density-Driven Thunderstorm Downbursts

The experiments were designed by Roghayyeh Babaei koli under the guidance of Professor Eric Savory. Kyle Graat and Calvin Chan assisted in conducting the experiments and preparing the schematic diagrams. All the literature review, data analysis and drafting the manuscript were carried out by Roghayyeh Babaei koli with the feedbacks and revisions of Professor Eric Savory.

Chapter 3: Experimental Simulation of Traveling Downbursts Using the Two-Fluid Model

The experiments were designed by Roghayyeh Babaei koli under the quidence of Professor Eric Savory. Calvin Chan prepared the schematic diagram of the setup. Kyle Graat helped in the set up of the hot wire anemometry system and conducting the release experiments. All the literature review, data analysis and drafting the manuscript were carried out by Roghayyeh Babaei koli with the feedbacks and revisions of Professor Eric Savory.

Acknowledgements

I would like to show my gratitude to my supervisor, Professor Eric Savory, for his invaluable support and guidance throughout this project.

I would also like to thank our laboratory manager Walid Altahan, Ron Struke at the electronics shop and Dan Sweiger at the UMS for their insight and help at different stages of this project.

I would also like to acknowledge the help and assistance I received from Kyle Graat, Calvin Chan, Noe Michel and Ben Cogswell in conducting the experiments.

I would also like to thank my examiners for taking time from their busy schedules to evaluate my thesis.

Table of Contents

List of Tables

List of Figures

Nomenclature

A	Area of the bright region in PLIF images	cm^2
$A_{cross-section}$	Cross-sectional area of the channel flow	m^2
a_p	Area of each pixel in the image	cm^2
B	Buoyancy force per unit mass	m/s^2
C	Concentration of each pixel in the captured image	mg/L
$C_{background}$	Concentration of the corresponding pixel in the background image	mg/L
$C_{maximum}$	Maximum concentration used in the experiments	mg/L
$C_{relative}$	Relative concentration	-
$\bar{C}_{relative}$	Average relative concentration	-
D	DC motor duty cycle	%
d_i	Release cylinder inside diameter	Cm
d_o	Release cylinder outside diameter	Cm
E	Hot film probe output voltage	Volts
f	Focal length of the combined lenses	Mm
f_1	Focal length of the first cylindrical lens	Mm
f_2	Focal length of the second cylindrical lens	Mm
g	Gravitational acceleration	m/s^2
H	Vortex front height	Cm
h	Ambient fluid depth in the hydraulic flume	Cm
H_0	Initial release height	Cm
h_i	Release cylinder inside height	Cm
h_o	Release cylinder outside height	Cm
h_{top}	Ambient fluid depth above the cylinder	Cm

I	Intensity of each pixel in the captured image	-
$I_{background}$	Intensity of the corresponding pixel in the background image	-
$I_{maximum}$	Intensity of the corresponding pixel in the average calibration image of the highest concentration	-
L_C	Length of the contraction part of the channel inlet	Mm
N	Number of release experiments in the flume	-
n	Refractive index	-
N_p	Number of pixels in the bright region of PLIF images	-
Q	Release cylinder volume	cm^3
Q_{pump}	Pump flow rate	L/s
R	Vortex radius in a static downburst	Cm
Re	Downburst Reynolds number	-
R_0	Downburst length scale	Cm
R_L	Left side radius in a traveling downburst	Cm
R_R	Right side radius in a traveling downburst	Cm
Re_x	Reynold number at distance x	-
t	Time	S
T_0	Downburst time scale	S
U	Free stream velocity of the ambient fluid in x-direction	cm/s
u	Ambient fluid velocity in x-direction	cm/s
$\bar{u}$	Average velocity of the ambient fluid in the hydraulic flume	cm/s
u_t	Translation velocity	cm/s
V_0	Downburst velocity scale	cm/s
V_g	Glycerol volume	m^3

V_w	Water volume	m^3
W	Outflow width	Cm
w	Concentration	% by mass
w_a	Ambient fluid concentration	% by mass
w_d	Dense fluid concentration	% by mass
x_{CP}	x-coordinate of the outflow central point	Cm
Δn	Refractive index difference	-
$\Delta \eta$	Dynamic viscosity difference	mPa s
$\Delta \rho$	Density difference	kg/m^3
δ_x	Boundary layer thickness at distance x	Cm
η	Dynamic viscosity	mPa s
η_a	Ambient fluid dynamic viscosity	mPa s
ν_a	Ambient fluid kinematic viscosity	m^2/s
ρ	Density	kg/m^3
ρ_a	Ambient fluid density	kg/m^3
ρ_d	Dense fluid density	kg/m^3
ρ_g	Glycerol density	kg/m^3
ρ_w	Water density	kg/m^3
$\overline{\frac{dR}{dt}}_{BT}$	Radial speed of a static downburst front before impacting on the ground	cm/s
$\overline{\frac{dR_L}{dt}}_{BT}$	Radial speed of the left side of a traveling downburst front before impacting on the ground	cm/s
$\overline{\frac{dR_R}{dt}}_{BT}$	Radial speed of the right side of a traveling downburst front before impacting on the ground	cm/s
$\overline{\frac{dR}{dt}}_{AT}$	Radial speed of a static downburst front after impacting on the ground	cm/s

Chapter 1

1   Introduction

In this chapter, first, a thunderstorm downburst is defined as a meteorological phenomenon and a high intensity wind event. Then, a brief review of previous downburst research studies is explained, this is followed by describing the motivations behind conducting the current research project. Finally, the general structure of the thesis and the content of each chapter are presented.

1.1   Downbursts: Origin and Characteristics

Downbursts are strong localized wind events that are typically associated with thunderstorms (Fujita 1976; Proctor 1988). The evaporative cooling due to microphysical processes within a thunderstorm cloud and the weight of precipitation lead to the downward acceleration of a negatively buoyant air mass, which after reaching the earth's surface, spreads radially away from the impact point and causes high intensity winds near the ground (Figure 1.1) (Wolfson 1988; Orf et al. 2014). The abruptly changed vertical and horizontal wind fields resulting from downbursts are primarily hazardous to aviation (especially to airplane takeoff and landing); high intensity winds in the radial spreading phase of downbursts (up to 75 m/s) can also pose a great threat to surface structures like electricity transmission lines (Figure 1.2(a)-(b)) (Fujita 1985; Alahyari and Longmire 1994; Shehata et al. 2005; Holmes 2008; Mara et al. 2016). Fatalities, injuries and capital costs of such high intensity wind events are well documented (Proctor 1988; Parsons 1990; Bluestein 2013).
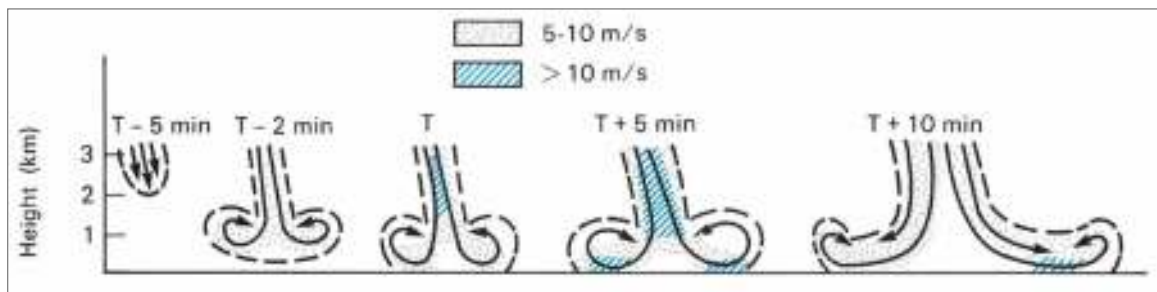
Figure 1.1: Schematic display of a thunderstorm downburst life cycle (adapted from Wolfson 1988)
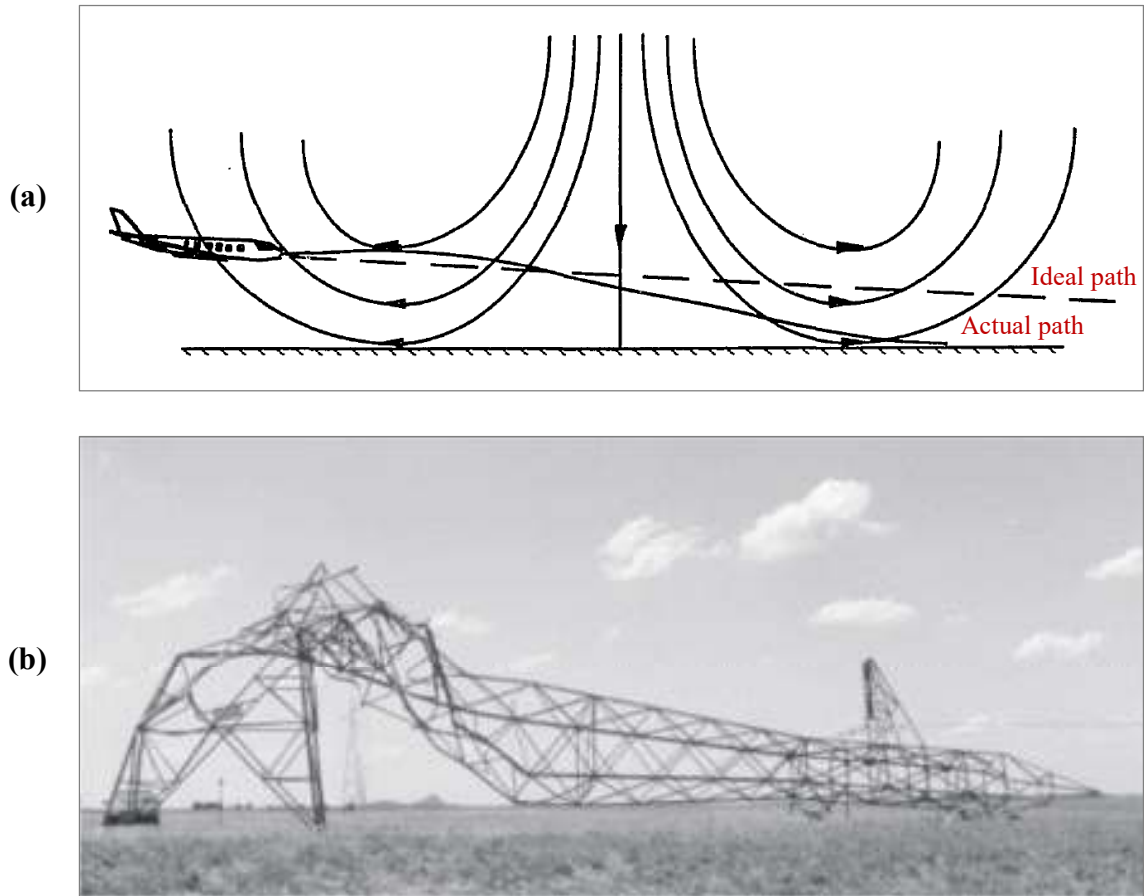
Figure 1.2: (a) Change in the landing path of an aircraft due to vertical and radial downburst winds (adapted from Alahyari 1995), (b) failure of an electricity transmission line exposed to high intensity winds of a downburst (adapted from Holmes 2008)

Downbursts were first identified by Ted Fujita in his investigations into an airplane crash at John F. Kennedy airport in New York City (Eastern Airlines Flight 66 on June 4, 1975) (Fujita 1986). Following Fujita's observations, several important downburst field studies were conducted: (1) Northern Illinois Meteorological Research on Downbursts (NIMROD) in the spring and summer of 1978, (2) Joint Airport Weather Studies (JAWS) in the Denver area during the summer of 1982, and (3) Microburst and Severe Thunderstorm (MIST) project in Huntsville, Alabama during the summer of 1986 (McCarthy et al. 1982; Eilts and Doviak 1987; Bluestein 2013). These field investigations helped in the primary definitions and characterizations of downbursts, the term downburst was initially used by Fujita who later subdivided it into microbursts and macrobursts. This division was based on the horizontal

extent of downburst wind fronts (Alahyari 1995): for events with horizontal winds extending from 4 km to tens of kilometers, the term macroburst was used, the duration of a typical macroburst is between 5 minutes to 30 minutes. On the other hand, microbursts are downbursts with horizontal extents less than 4 km and with an average lifecycle duration of 10 minutes. Downbursts can also be classified based on their precipitation content (Proctor 1988): dry downbursts that usually occur in dry atmosphere where the height of thunderstorm cloud base is relatively high, such conditions promote the possibility of evaporative cooling which results in the formation of downdrafts. Contrary to dry downbursts, wet downbursts are usually associated with moist atmosphere and low cloud base heights. In such conditions the downdrafts are primarily formed due to the high precipitation (water) content. Examples of dry and wet downbursts are shown in Figure 1.3(a)-(b).
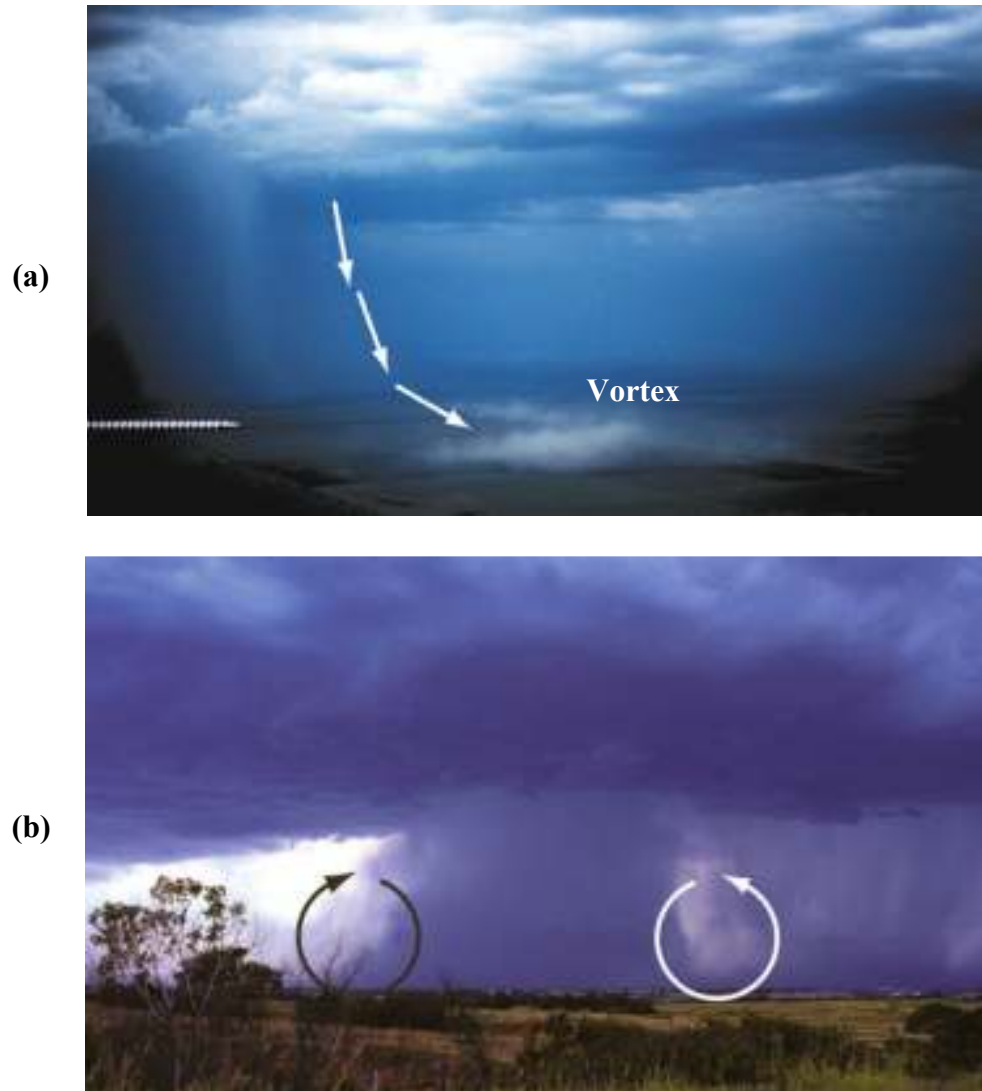
Figure 1.3: (a) A dry downburst in southwestern Kansas observed on May 31, 1994 (white arrows show the air motion path and the vortex ring carrying dust is visible near the ground), (b) a wet downburst in Oklahoma City observed on July 26, 1978 (circulation in the vortex ring is depicted by arrows in two sides of downdraft) (adapted from Bluestein 2013)

As the downdraft descends toward the ground, a baroclinically generated horizontal vorticity develops along its leading edge. Such ring vortices in downbursts can be mathematically defined using Equation (1.1) (Bluestein 2007).

$$\frac{D}{Dt}\left(\frac{\partial u}{\partial z} - \frac{\partial w}{\partial x}\right) = -\frac{\partial B}{\partial x} \qquad (1.1)$$

In this equation, the y-axis is assumed as the vertical direction and $\left(\frac{\partial u}{\partial z} - \frac{\partial w}{\partial x}\right)$ is the vorticity component parallel to the leading edge (horizontal vorticity about the y-axis). The term $\frac{\partial B}{\partial x}$ in the right side of this equation refers to the baroclinic generation where B is the buoyancy force per unit mass. A schematic display of downburst vortex is illustrated in Figure 1.4.
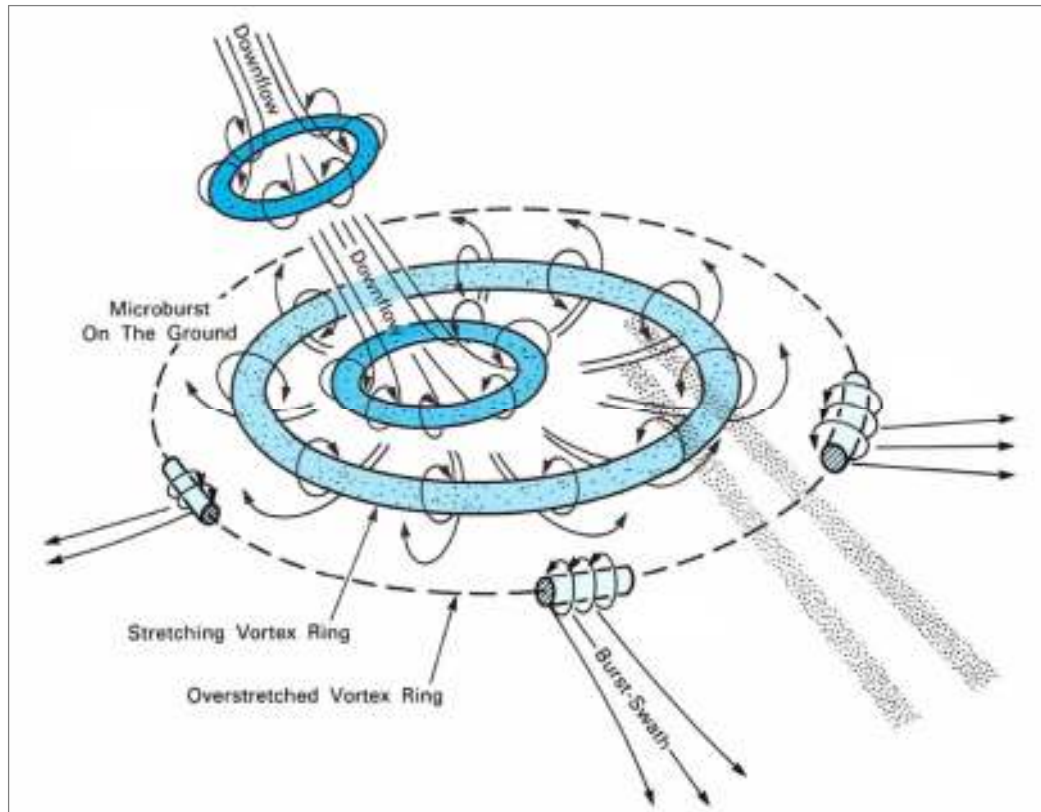
Figure 1.4: 3-D schematic view of a downburst vortex in different stages of its development (adapted from Wolfson 1988)

Horizontal vorticity is one of the major characteristics of thunderstorm downbursts and its presence can be detected by the rain and dust that are being displaced along the circulation of vortex (Figure 1.3(a)-(b)) (Bluestein 2013).

1.2   Literature review

Thunderstorm downbursts were first investigated as a meteorological phenomenon. As discussed in the previous section, downbursts were detected by Fujita in his quest to study the reasons behind an airplane crash. The efforts of early researchers who conducted major field

investigations (NIMROD, JAWS, MIST) led to the discovery and characterization of an interesting meteorological event with unique specifications that were distinctly different from other common weather events (like tornadoes and typical synoptic winds). Thus, it can be confidently claimed that these comprehensive field studies played the main role in obtaining a vivid picture of downbursts and provided first hand valuable information on the major aspects of these events (Alahyari 1995). Data from field investigations have been analyzed and documented in several old and new research studies (McCarthy et al. 1982; Eilts and Doviak 1987; Hjelmfelt 1987; Gunter and Schroeder 2015, Solari et al. 2015, Burlando et al. 2017). Since discovery and early characterizations, downbursts have remained the subject of numerous research projects in the fields of meteorology and wind engineering, the reason behind the interest of research community in this phenomenon can be divided into three categories (Bluestein 2013): (1) understanding and preparing for the potential dangers of downbursts to aviation, (2) designing wind-resistant structures by considering the unique profiles of horizontal downburst winds where high wind velocities occur in a region very close to the surface, and (3) studying the role of downbursts in the morphological structure of thunderstorms.

Although conducting direct measurements of real downbursts seems to be the most appropriate way in the study of these natural events, there are major operational and economical obstacles that demand alternative approaches in the study of downbursts. The short duration and unpredictable nature of downbursts, which is weakly correlated to environmental conditions, along with the expense and challenges of experimental measurements at natural scales are among the above-mentioned obstacles. Moreover, obtaining accurate and complete horizontal velocity data in the near ground region using Doppler radar measurements is not an easy and straightforward task (Alahyari and Longmire 1994).

Generally, two different downburst modeling approaches have been taken by researchers: impinging jet (IJ) model (Kim and Hangen 2007; Sengupta and Sarkar 2008; McConville et al. 2009; Zhang et al. 2013) and cooling source (CS) model (Mason et al. 2009; Vermeire et al. 2011; Zhang et al. 2013). The impinging jet model, which is popular among wind engineers, simplifies the complex driving force behind the formation of downdrafts and utilizes a downward facing forced momentum source placed above a surface (a circular impinging jet)

to resemble the downward motion of downbursts and its subsequent contact with the ground. Simplicity and scalability of this modeling approach encouraged numerous researchers to employ it in the experimental and numerical simulations of downbursts (Figure 1.5). Hjelmfelt (1987) who analyzed the downbursts of the JAWS project, averaged the normalized radial velocity profiles of several downbursts and showed how the average profile of natural events was similar to the velocity profile of a wall jet. However, since a major step in the early discovery of thunderstorm downburst was to identify the driving force of the event and the processes that lead to the initiation of it, completely neglecting the results of such efforts and substituting the negative buoyancy with an impulsively driven mass of air is unrealistic and unrepresentative of actual atmospheric conditions (Oreskovic 2016).
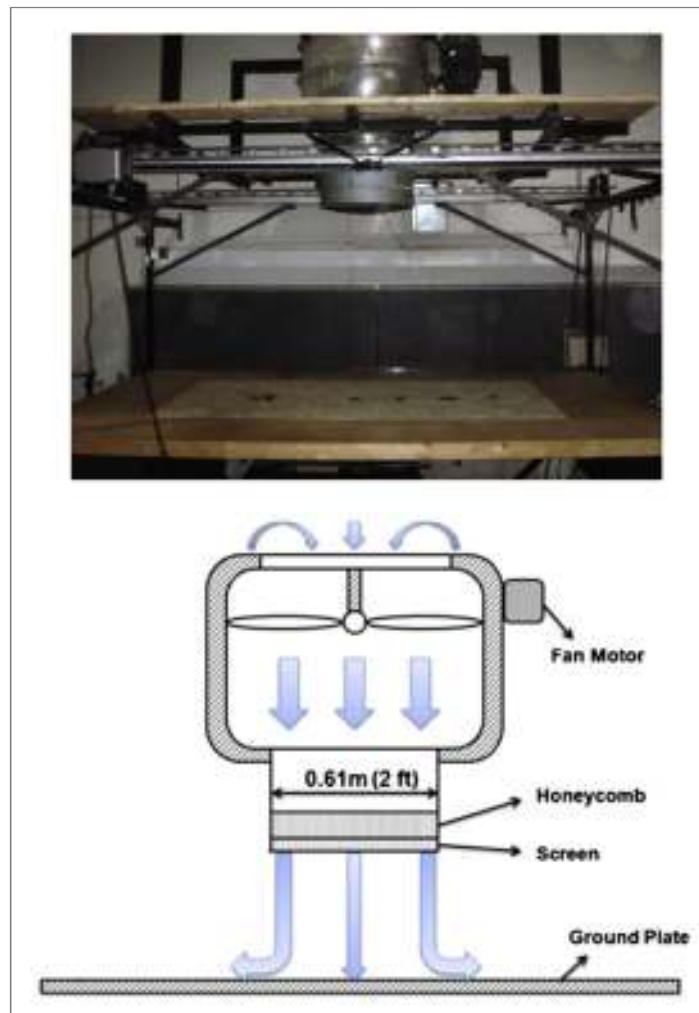
Figure 1.5: An example of experimental apparatus for the simulation of downbursts based on impinging jet model (adapted from Zhang et al. 2013)

The alternative approach, which uses the negative buoyancy as driving force, is the cooling source method. This method can be implemented both numerically and experimentally (Zhang et al. 2013). In the numerical simulations based on this method, a cooling source function is defined in a space which is assumed to be part of a full cloud domain (Anderson et al. 1992; Oreskovic 2016). This source function is used to mimic the thermodynamic cooling that occurs within the cloud, in other words, the heat loss due to the phase change of various types of precipitation in the domain is represented by the cooling function. In Figure 1.6, examples of results from downburst simulations using the cooling source method are presented. Although this approach does not consider the effect of microphysical processes and assumes a homogeneous atmosphere, employing the negative buoyancy as the real cause of downdraft creation is a significant improvement compared to the previously discussed impinging jet model.
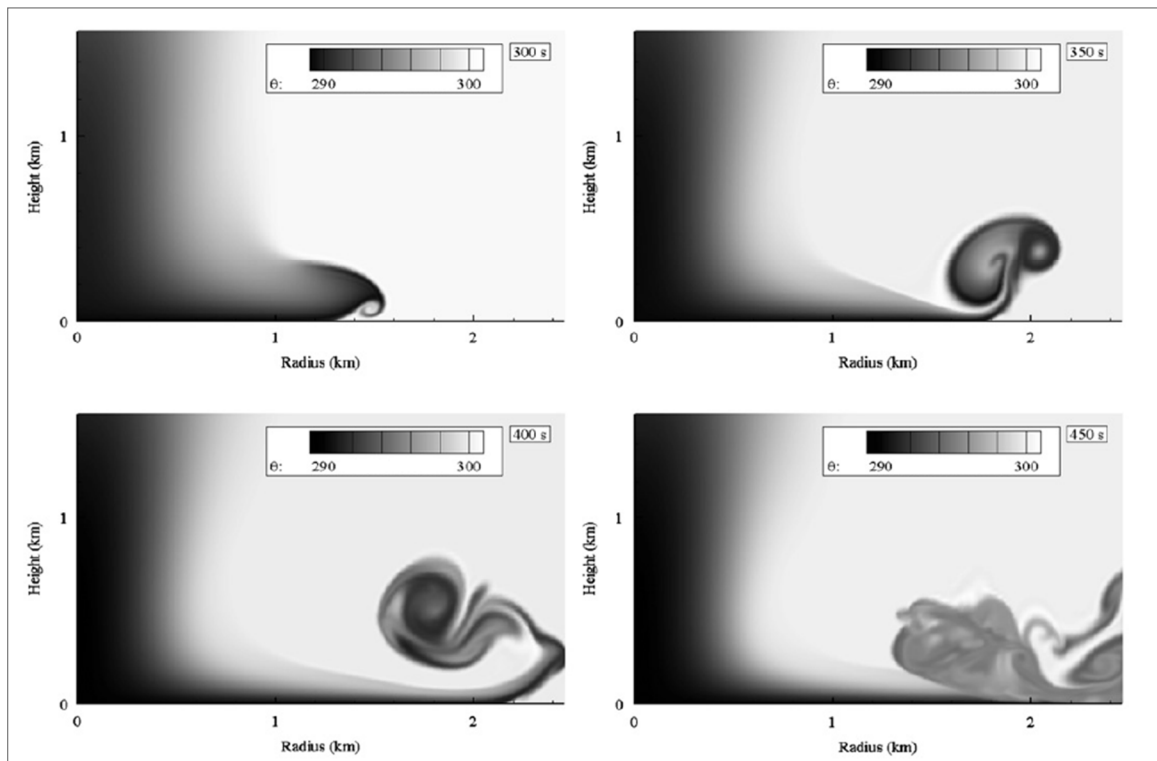
Figure 1.6: Temperature contours in the numerical simulation of downbursts based on cooling source model (adapted from Vermeire et al. 2011)

A more comprehensive, and complicated, approach for the numerical simulation of downbursts is the 3-D full cloud model which involves all the processes occurring within the thunderstorm

cloud, examines the influence of environmental conditions on the formation of downbursts and takes the effect of precipitation drag into account (Bryan and Fritsch 2002; Orf et al. 2012). Despite the capabilities of such models in producing detailed information on all aspects of downburst phenomenon, the high computational costs associated with them make it difficult to use them for engineering purposes (Zhang et al. 2013). Instead, sub-cloud models, with smaller physical domains, can be successfully used to simulate downbursts by introducing a cooling source function and employing negative buoyancy as the driving force of the event.

The experimental investigation of thunderstorm downbursts based on cooling source model was first introduced by Lundgren et al. (1992). To conduct experiments on the basis of thermodynamic cooling and negative buoyancy, they used two solutions with different densities and designed a simple setup to release a small volume of more dense solution (with the density of $\rho+\Delta\rho$) into a tank filled with the less dense solution (with the density of ρ). By creating small values of density difference between the two fluids and by employing the Boussinesq approximation, liquids substituted gases in the experimental implementation of cooling source model which was also called the two-fluid model. In Figure 1.7, the schematic diagram of the setup used by that research group is shown. The dense solution was held by a cylinder (coloured in grey) that was drilled at the top (to 50% solidity) and covered by an aged latex membrane at the bottom, and the release of dense fluid was accomplished by puncturing the membrane.

In fact, this experimental approach models a downburst event starting from the point that the mass of cold air accelerates toward the ground. Lundgren et al. (1992) used fresh water and salt water as the light and dense solutions, respectively, and employed the laser induced fluorescence (LIF) technique to visualise the flow field of simulated downbursts. Later, Alahyari (1995) focused on the selection of appropriate solutions for the two-fluid model. He examined different solution pairs and finally chose the aqueous solutions of glycerol and potassium dihydrogen phosphate as the ambient and downburst solutions because of their similar viscosity and refractive index values to ease the application of laser-based flow visualisation techniques.
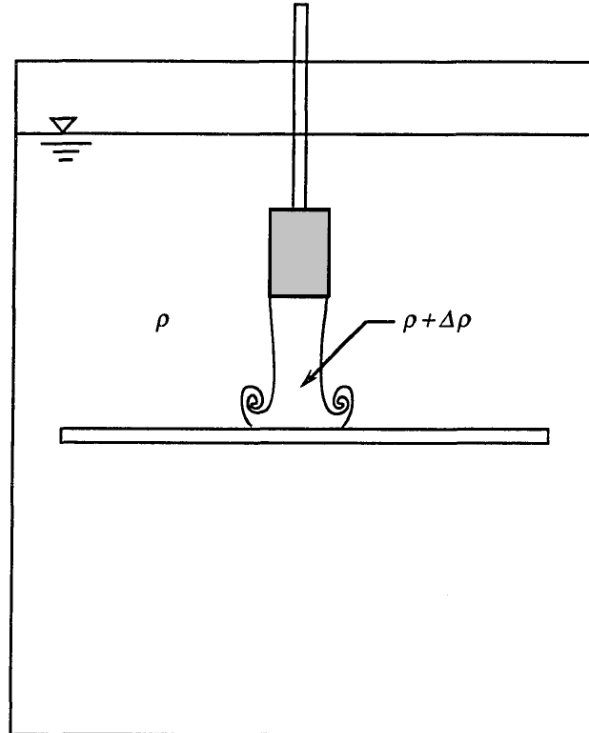
Figure 1.7: Experimental setup for the simulation of downbursts base on density-driven two-fluid model (adapted from Lundgren et al. 1992; Yao 1994; Alahyari and Longmire 1994; Alahyari 1995; Yao and Lundgren 1996)

To relate the small size of laboratory simulated two-fluid release experiments to natural downburst scales, Lundgren et al. (1992) defined length and time scales based on the geometry of cylinder holding the dense fluid and the density difference between the two solutions, respectively, these scaling parameters were also used to define a velocity scale. Unlike the impinging jet model, in which the initial driving force of the event (down facing jet velocity) had a linear relationship with the velocity of produced outflow, the Lundgren et al. (1992) scaling model suggests a non-linear relationship between the driving force (density difference) and the outflow velocity (Yao and Lundgren 1996; Kim and Hangan 2007). Oreskovic et al. (2018) assessed the validity of Lundgren et al. (1992) scaling rule by comparing the results of numerical simulations from a full cloud model (Large Eddy Simulations) and two-fluid model (Unsteady Reynolds-Averaged Navier-Stokes simulations). In the latter, 2-D axisymmetric numerical modeling was used to incorporate the experimental conditions of releasing a dense liquid into a lighter surrounding, employing the same geometrical dimensions as the two-fluid release apparatus. According to the results of this study, when the time variations of radial

velocity were normalized by the Lundgren et al. (1992) scaling parameters, both the full cloud model and the small scale two-fluid model displayed similar profiles. The study of Oreskovic et al. (2018), for the first time, demonstrated the scalability of simulations based on negative buoyancy rather than an unrealistic forced momentum source.

1.3   Thesis motivation

The current research study is a response to the lack of experimental investigations of thunderstorm downbursts based on the actual driving force of the event. Access to such experimental information is of great importance to further understanding of downbursts as high intensity wind events. Data from meticulously conducted experimental simulations can be used to validate the results from numerical studies and to gather information in the near ground region. Shortcomings of field investigations in acquiring proper measurements at low heights (as discussed in the previous part) and the substantial effect of initial and boundary condition assumptions on the results of numerical simulations in the near ground region cause problems in elucidating the behaviour of downbursts near the surface (Alahyari and Longmire 1994). Thus, the two-fluid method, which employs the density difference between two liquids to resemble the formation of a negatively buoyant air mass within the thunderstorm cloud, can be used to obtain reliable experimental data.

The very limited number of previous experimental investigations of downbursts using the two-fluid model was briefly discussed in the previous part (Lundgren et al. 1992; Yao 1994; Alahyari 1995). In these studies, a novel and scalable approach was introduced. However, the features of their experimental setup (Figure 1.7) were simplified and not representative of natural conditions of atmospheric downbursts. Problems associated with the experimental setup presented in Figure 1.7 can be categorized as follows: (1) design of the cylindrical volume that holds the dense solution, and (2) release of the dense fluid into the quiescent environment of the tank. The solid wall of the release cylinder imposes a boundary separating the dense and light solutions, but such boundary is absent in natural downbursts where the two fluids are in full contact with each other (Bluestein 2013). Moreover, puncturing a membrane diaphragm for sudden liquid release leads to problems with the clarity of evolving outflow boundaries and repeatability of experiments (Yao 1994; Alahyari 1995). On the other hand, releasing the dense fluid into a static environment is far from what happens in real events where

the thunderstorm cloud is not motionless and the environment in which the downdraft descends is not quiescent. In other words, most of the natural downbursts exhibit an embedded flow pattern and asymmetric flow field because of the storm motion and environmental shear. Indeed, the term traveling downburst is used to describe this group of downbursts (Hjelmfelt 1987; Orf and Anderson 1998; Holmes and Oliver 2000).

Solving the above-mentioned issues and designing an experimental apparatus that implements real downburst release conditions are complicated and challenging tasks (it should be noted that numerical studies of traveling downbursts are also very limited and incomplete.). The current research study, for the first time, aims to re-design the entire two-fluid model experimental setup and address the two general problems described above. In this way, a reliable setup, which uses the negative buoyancy as the primary cause of downburst phenomenon, can be designed and used for exploring many aspects of downbursts that are difficult, expensive and time-consuming to characterize in field investigations and numerical simulations.

1.4   Thesis Organization

This thesis is presented in the integrated article format and includes two articles. In the first article (Chapter 2), the process of designing two new release cylinders (Cylinder 1 with a solid wall and Cylinder 2 with a partially eliminated wall) is described in detail and primary experiments for testing the applicability of the Lundgren et al. (1992) scaling are presented. In addition, the capability of new cylinders in producing repeatable outflows is discussed, and the impacts of cylinder wall elimination and altering the release height are detailed.

The second article (Chapter 3) is focused on a re-designed experimental setup that allows the implementation of storm translation and environmental flow conditions. This includes detailed explanations of a flow circuit including a hydraulic flume, a reservoir tank and a pumping system. For the first time, this chapter presents the results of experimental simulations of traveling downbursts and shows how their footprints are different from downbursts in quiescent environment.

Finally, in Chapter 4, the findings of current research work are summarized and recommendations for future applications of the new setup in downbursts studies are discussed.

1.5 References

Alahyari AA (1995) Dynamics of laboratory simulated microbursts. PhD Dissertation, University of Minnesota

Alahyari AA, Longmire EK (1994) Particle image velocimetry in a variable density flow: application to a dynamically evolving microburst. Exp Fluids 17:434-440

Anderson JR, Orf LG, Straka JM (1992) A 3-D model system for simulating thunderstorm microburst outflows. Meteorol Atmos Phys 49:125-131

Bluestein HB (2007) Advances in applications of the physics of fluids to severe weather systems. Rep Prog Phys 70:1259-1323

Bluestein HB (2013) Severe Convective Storms and Tornadoes, Observations and Dynamics. Springer Praxis, Chichester, UK

Bryan GH, Fritsch JM (2002) A benchmark simulation for moist nonhydrostatic numerical Models. Mon Wea Rev 130:2917-2928

Burlando M, Romanic D, Solari G, Hangan H, Zhang S (2017) Field data analysis and weather scenario of a downburst event in Livorno, Italy, on 1 October 2012. Mon Wea Rev 145:3507-3527

Eilts MD, Doviak RJ (1987) Oklahoma downbursts and their asymmetry. J Climate Appl Meteor 26:69-78

Fujita TT (1976) Spearhead echo and downburst near the approach end of a John F. Kennedy Airport runway, New York City (SMRP research paper). Satellite & Mesometeorology Research Project, Department of the Geophysical Sciences, University of Chicago, USA

Fujita TT (1985) The downburst. The University of Chicago Press, Chicago, USA

Fujita TT (1986) DFW downburst. The University of Chicago Press, Chicago, USA

Gunter WS, Schroeder JL (2015) High-resolution full-scale measurements of thunderstorm outflow winds. J Wind Eng Ind Aerodyn 138:13-26

Hjelmfelt MR (1987) Structure and life cycle of microburst outflows observed in Colorado. J Appl Meteorol 27:900-927

Holmes JD (2008) Recent developments in the specification of wind loads on transmission lines. J Wind Eng 5:8-18

Holmes JD, Oliver SE (2000) An empirical model of a downburst. Eng Struct 22:1167-1172

Kim J, Hangan H (2007) Numerical simulations of impinging jets with application to downbursts. J Wind Eng Ind Aerodyn 95:279-298

Lundgren TS, Yao J, Mansour NN (1992) Microburst modelling and scaling. J Fluid Mech 239:461-488

Mara TG, Hong HP, Lee CS, Ho TCE (2016) Capacity of a transmission tower under downburst wind loading. Wind Struct 22:65-87

Mason MS, Wood GS, Fletcher DF (2009) Numerical simulation of downburst winds. J Wind Eng Ind Aerodyn 97:523-539

McCarthy J, Wilson JW, Fujita TT (1982) The joint airport weather studies project. Bull Amer Meteor Soc 63:15-22

McConville AC, Sterling M, Baker CJ (2009) The physical simulation of thunderstorm downbursts using an impinging jet. Wind Struct 12:133-149

Oreskovic C (2016) Numerical investigation of full scale thunderstorm downbursts: a parametric study and comparison to meteorological model. MESc dissertation, University of Western Ontario

Oreskovic C, Savory E, Porto J, Orf LG (2018) Evolution and scaling of a simulated downburst-producing thunderstorm outflow. Wind Struct 26:147-161

Orf LG, Anderson JR (1998) A numerical study of traveling microbursts. Mon Wea Rev 127:1244-1258

Orf LG, Kantor E, Savory E (2012) Simulation of a downburst-producing thunderstorm using a very high-resolution three-dimensional cloud model. J Wind Eng Ind Aerodyn 104-106:547-557

Orf LG, Oreskovic C, Savory E, Kantor E (2014) Circumferential analysis of a simulated three-dimensional downburst-producing thunderstorm outflow. J Wind Eng Ind Aerodyn 135:182-190

Parsons DB (1990) Dynamics and fine structure of a microburst. J Atmos Sci 47:1674-1692

Proctor FH (1988) Numerical simulations of an isolated microburst. Part I: dynamics and structure. J Atmos Sci 45:3137-3160

Sengupta A, Sarkar PP (2008) Experimental measurement and numerical simulation of an impinging jet with application to thunderstorm microburst winds. J Wind Eng Ind Aerodyn 96: 345-365

Shehata AY, El Dammatty AA, Savory E (2005) Finite element modeling of transmission line under downburst wind loading. Finite Elem Anal Des 42:71-89

Solari G, Burlando M, De Gaetano P, Repetto MP (2015) Characteristics of thunderstorms relevant to the wind loading of structures. Wind Struct 20:763-791

Vermeire BC, Orf LG, Savory E (2011) Improved modelling of downburst outflows for wind engineering applications using a cooling source approach. J Wind Eng Ind Aerodyn 99:801-814

Wolfson MM (1988) Characteristics of microbursts in the continental United States. Lincoln Lab J 1:49-74

Yao J (1994) Experiments on microbursts. PhD Dissertation, University of Minnesota

Yao J, Lundgren TS (1996) Experimental investigation of microbursts. Exp Fluids 21:17-25

Zhang Y, Hu H, Sarkar PP (2013) Modeling of microburst outflows using impinging jet and cooling source approaches and their comparison. Eng Struct 56: 779-793

Chapter 2

2 Characterizing the Liquid Release Mechanism Performance in the Experimental Simulation of Density-Driven Thunderstorm Downbursts

Thunderstorm downbursts cause strong and potentially hazardous vertical and horizontal wind flows. This meteorological phenomenon has been the subject of numerous field studies, experimental explorations and numerical simulations. This research work, for the first time, aimed to challenge the drawbacks of previous experimental studies. Novel release mechanisms were designed for the visualization of density-driven downbursts using the two-fluid model. The ability of these new designs in producing repeatable flow fields was examined and the influence of introducing openings into the release cylinder wall, for minimizing the wall effects, was tested. Various density differences were employed to investigate the validity of previously developed scaling parameters. Finally, experiments with different initial release heights were conducted to analyze the effect of this parameter on the simulated downbursts. The planar laser induced fluorescence (PLIF) technique was utilized to visualize the flows and to provide quantitative scalar field data.

2.1   Introduction

A thunderstorm downburst is a strong downward movement of cold and dense air which is followed by extreme horizontal outflow winds after its impact on the ground (Fujita 1985). This descending air mass is primarily produced by losing heat through thermodynamic phenomena occurring within a thunderstorm cloud (e.g. evaporation of rain, melting of hail, and sublimation of snow). The resultant decrease in temperature makes this air parcel heavier than its surroundings and leads to its acceleration toward the ground along with some form of precipitation (Vermeire et al. 2011a; Orf et al. 2014). The precipitation can induce drag effects that further contribute to the downward movement of this cold air mass (Orf et al. 2012).

The sudden, diverging and high-speed winds caused by downbursts are distinct from typical synoptic wind fields and can cause serious damage to surface structures like electricity transmission lines (Kim et al. 2007; Darwish and El Damatty 2011; Mara et al. 2016). Moreover, the abruptly changed vertical and horizontal wind speeds make downbursts

problematic to aircraft during their takeoff and landing (Hjelmfelt 1987; Alahyari 1995). Hence, downbursts have been of great interest among both meteorologists and wind engineers; obtaining realistic and representative data about these natural events can make a significant contribution to lowering their economic and human costs. Several numerical (Orf et al. 1996; Orf and Anderson 1998; Mason et al. 2010; Vermeire et al. 2011a-b; Orf et al. 2014; Roberto et al. 2014; Aboshosha et al. 2015), experimental (Lundgren et al. 1992; Alahyari and Longmire 1994; Yao and Lundgren 1996), and field studies (McCarthy et al. 1982; Eilts and Doviak 1987; Hjelmfelt 1987) have been conducted in this regard. The two most common modelling approaches are the transient impinging momentum jet (IJ) model (Kim and Hangen 2007; McConville et al. 2009; Zhang et al. 2013) and the density-driven cooling source (CS) model (Mason et al. 2009; Vermeire et al. 2011a; Zhang et al. 2013). In the first approach, the density difference (one of the primary driving mechanisms in a real event) is replaced by a downward momentum source. The latter method introduces a cooling source which represents the key factors (the result of the above mentioned thermodynamic processes) producing the temperature and density differences, giving rise to baroclinic vorticity generation (Bluestein 2007). Although this method is more realistic, it usually assumes a vertically homogeneous atmosphere. Moreover, it fails to consider the phase change occurring during the event and the drag force imposed by precipitation, problems that are also associated with the IJ model (Orf et al. 2012).

One major shortcoming in downburst research is the lack of representative experimental data which are essential for validating the numerical results, especially in the near ground region. Among numerous empirical attempts that delved into the study of this phenomenon, some used the IJ approach which by its nature denies the primary driving force of the event (Sengupta and Sarkar 2008; McConville et al. 2009), and some others used the two-fluid model to mimic the density difference between the descending and ambient fluids (Lundgren et al. 1992; Alahyari and Longmire 1994; Yao and Lundgren 1996). The experimental studies that were conducted based on the two-fluid model used a dense fluid that was held within a cylinder submerged in a tank containing ambient fluid. The sudden dense fluid release was performed by puncturing a membrane covering the bottom of cylinder. These experiments successfully simulated different stages of the life cycle of a downburst (Lundgren et al. 1992; Yao 1994; Alahyari and Longmire 1994) and, by proposing a scaling law, allowed the resultant flow fields to be

compared to those of numerical investigations and field studies (Lundgren et al. 1992). The problem was that the experimental setup used in these studies did not sufficiently represent the real event because the introduction of cylinder wall induced wall shear and, hence, additional vorticity generation (as also occurs within the nozzle in an IJ simulation) which is absent in nature. Moreover, because of the arbitrary nature of the membrane puncturing, there was a lack of repeatability in the experiments. Also, the experimental setup was simplified such that the downbursts essentially originated from a stationary cloud and fell into a still environment.

Thus, it can be concluded that a realistic experimental data set representing downbursts must meet the following conditions: (1) using the negative buoyancy as the main mechanism for initiating the downward movement of fluid, (2) making the dense fluid release conditions as close to reality as possible, (3) repeatability and (4) performing experiments based on real event specifications (such as storm translation (Orf and Anderson 1998) and the occurrence of multiple events forming downburst lines (Orf et al. 1996; Vermeire et al. 2011b)). By noticing the failure of previous studies to address these criteria, the necessity of taking a novel experimental approach becomes clear.

The current study focused on the first three issues and is related to the design and performance evaluation of novel dense fluid release mechanisms to be later employed in further experiments with a high degree of reliability. In this regard, the setup used by previous experimental studies was chosen as the base, and its features were enhanced. The influence of the cylindrical container wall on the produced vortex was examined by employing two different designs of release cylinder and the effects of altering the values of density difference and initial release height were also investigated. The resultant flow field was inspected using the non-intrusive planar laser induced fluorescence (PLIF) technique in order to quantify the scalar fields.

2.2   Experimental details

In this section, first, the aqueous solutions used for the two-fluid density-driven experiments and their properties are introduced. Then, the application of the scaling law of Lundgren et al. (1992) for the current study is discussed and, the dimensions of the experimentally simulated downbursts are compared to those of real events. The rest of this section provides information on the experimental setup, visualization and calibration methods, and experimental procedure, respectively.

2.2.1   Selection of appropriate solutions

For simulation of a downburst event using the two-fluid model in the laboratory, several assumptions were made: (1) initial density variation in the flow field, between the dense and ambient fluids, was considered to be sharp rather than continuous, (2) the flow and environment were assumed to be respectively incompressible and unstratified, and (3) the density difference between the two fluids was specified as being very small, such that, based on the Boussinesq approximation, the value of this difference is more important than the densities of each fluid (Lundgren et al. 1992). These assumptions allow gases to be replaced by liquids of the same density difference for experimental purposes.

The next step was the selection of appropriate solutions for creating the desired density difference. In the experimental studies of Lundgren et al. (1992) and Yao (1994), fresh water and salt water were used as light and dense fluids, respectively. Later, Alahyari (1995) comprehensively examined the advantages and disadvantages of various liquid pairs and chose aqueous solutions of glycerol and potassium dihydrogen phosphate as the less and more dense fluids, respectively. The similarity of refractive indices, minimal difference between viscosities, transparency, non-volatility, cost and easy handling were the most important criteria considered in the selection of these two solutions (Alahyari 1995).

The values of dense and ambient fluid concentrations (w_d and w_a, expressed as a mass percentage), and the difference between densities ($\Delta\rho$), dynamic viscosities ($\Delta\eta$), and refractive indices (Δn) for the solutions used in different tests are presented in Table 2.1 (Alahyari and Longmire 1994; Rumble 2017).

2.2.2   Scaling parameters

In this study, the scaling parameters developed by Lundgren et al. (1992) (Equations (2.1)-(2.3)) were employed.

$$R_0 = \left(\frac{3Q}{4\pi}\right)^{1/3} \tag{2.1}$$

$$T_0 = \left(\frac{R_0}{g\left(\frac{\Delta\rho}{\rho_a}\right)}\right)^{1/2} \tag{2.2}$$

$$V_0 = \frac{R_0}{T_0} \tag{2.3}$$

The Reynolds number can also be calculated using Equation (2.4):

$$Re = \frac{R_0 V_0}{\nu_a} \tag{2.4}$$

It was demonstrated by Lundgren et al. (1992) that the dimensionless flow field of downbursts becomes Reynolds number independent for $Re > 3000$.

In these equations, R_0, T_0, V_0, Q and g represent the length scale (radius of an equivalent spherical volume holding the dense fluid), time scale, velocity scale, volume of the dense fluid and gravitational acceleration, respectively. The values of scaling parameters and Reynolds number for each test are also presented in Table 2.1, together with the initial release height (H_0) and the release mechanism used (Cylinder 1 and Cylinder 2, as described in section 2.3).

By considering the downburst event that caused the crash of Delta Airline Flight 191 (DL 191) as the reference (Fujita 1986; Lundgren et al. 1992), with a R_0 of 700 m, it can be said that the simulated downbursts in this study are around 16,000 times smaller than a real event.

Table 2.1: Characteristics of different release experiments

	Test 1	Test 2	Test 3	Test 4	Test 5	Test 6
w_d (% by mass)	7	7	5	10	7	7
w_a (% by mass)	7	7	7	7	7	7
$\Delta\rho/\rho_a$ (%)	3.37	3.37	1.95	5.51	3.37	3.37
$\Delta\eta/\eta_a$ (%)	3.89	3.89	8.20	3.15	3.89	3.89
Δn	0.0001	0.0001	0.0024	0.0033	0.0001	0.0001
R_0 (cm)	4.42	4.42	4.42	4.42	4.42	4.42
T_0 (s)	0.37	0.37	0.48	0.29	0.37	0.37
V_0 (cm/s)	12.09	12.09	9.20	15.46	12.09	12.09
Release height (H_0) (cm)	14.4	14.4	14.4	14.4	16.0	10.7
H_0/R_0	3.26	3.26	3.26	3.26	3.62	2.42
Re	4565	4565	3474	5837	4565	4565
Release mechanism	Cylinder 1	Cylinder 2	Cylinder 2	Cylinder 2	Cylinder 2	Cylinder 2

2.2.3 Experimental apparatus

Figure 2.1 illustrates the schematic diagram of the experimental setup utilized for performing the release tests. This setup consists of a rectangular glass tank (L × W × H = 58.7 cm × 30.3 cm × 38.6 cm and wall thickness = 0.4 cm) containing glycerol solution and a release cylinder holding potassium dihydrogen phosphate solution. The release cylinder was fully submerged in the ambient fluid and the height of fluid above the top of the cylinder was set to 9.0 cm ($\approx 2R_0$). Since different release heights were used in different tests (Table 2.1), the depth of the ambient fluid was adjusted for every test to satisfy this condition.

The length and width of the glass tank are around 13 and 7 times the characteristic length of the downburst (R_0), respectively. With these dimensions, it could be argued that the wall blockage effect may influence the flow field, especially after the ground impingement. However, since the major focus of this study was to compare the performance of the two release mechanisms in the initial stages of the vortex development, the confinement effect can be neglected since it is the same for all the experiments.
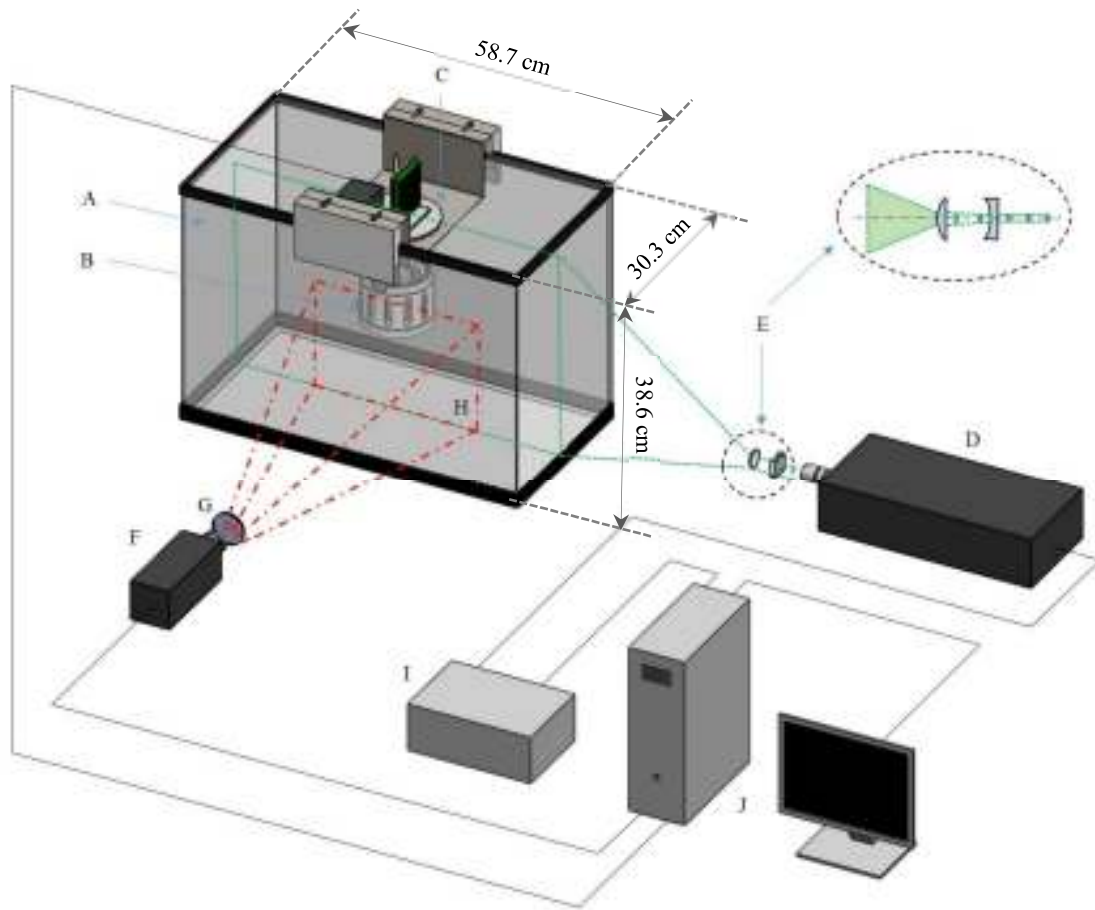
Figure 2.1: Schematic diagram of the experimental setup (A: Tank, B: Release cylinder, C: Cylinder support apparatus, D: Laser, E: Laser sheet optics, F: Camera, G: Filter, H: Field of view, I: Synchronizer, J: Computer system)

Figures 2.2 to 2.4 show two different designs of the release mechanism. The overall dimensions of these cylinders are the same, but their wall designs are different. As discussed in the introduction section, in a real downburst event, there is no boundary separating the dense and lighter fluids; but implementing this condition is not possible in the laboratory (Roberto et al. 2014). Thus, an attempt was made to partially eliminate the wall and investigate how this modification influences the resultant flow field.

Various components of each release cylinder are shown in Figure 2.2. In Figure 2.3, the two-dimensional view of the assembled cylinders along with the key dimensions are presented, it should be noted that the size of the cylinders was chosen to be similar to the size of those employed in previous experimental studies (Lundgren et al. 1992; Alahyari 1995) along with some adjustments that were made to embody the specifications of new

designs. Figure 2.4 illustrates the release mechanisms in their fully closed and fully open positions.

Cylinder 1   **Cylinder 2**
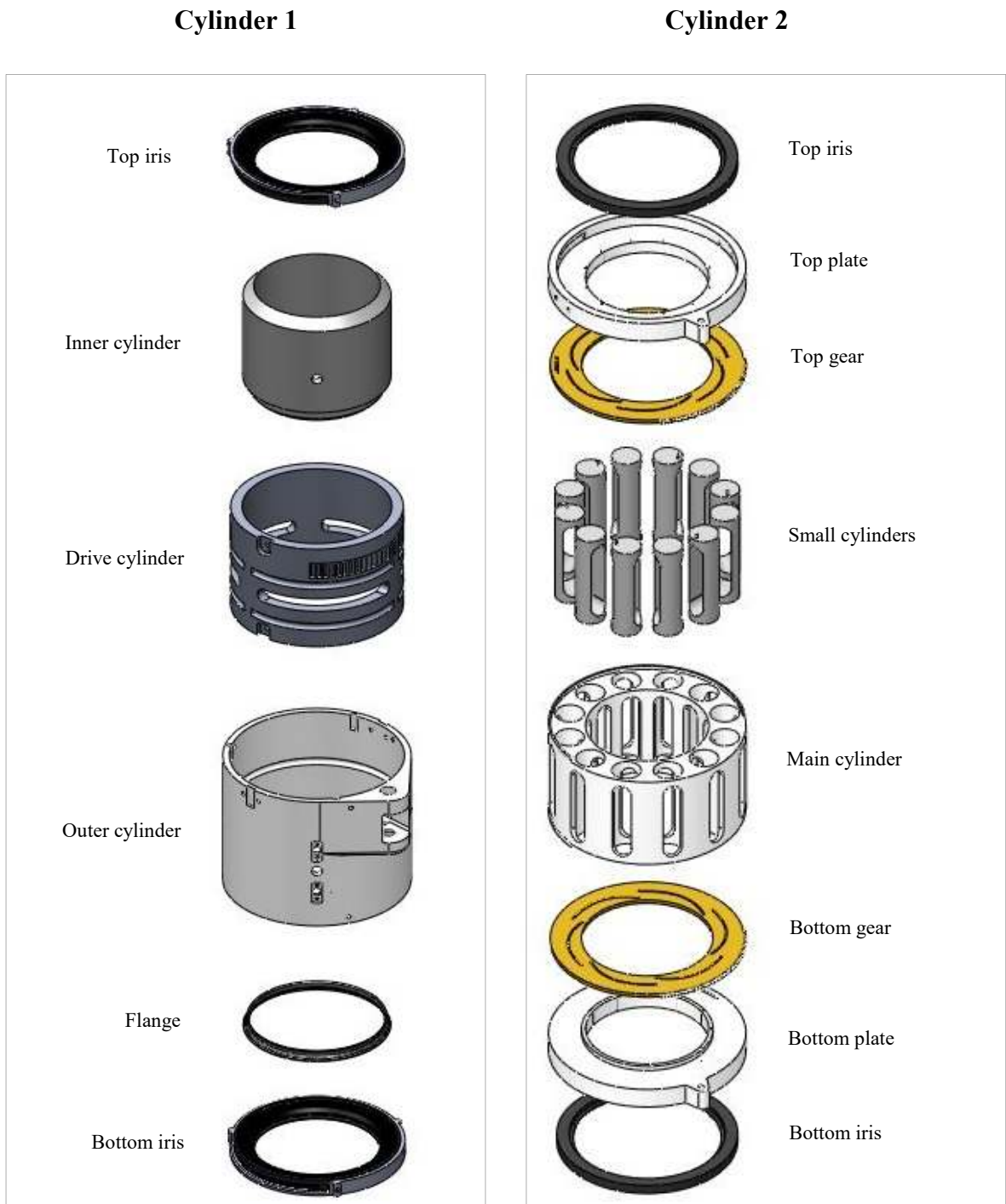
Figure 2.2: Different parts of the two designs of dense fluid release mechanism

These new designs were manufactured by a selective laser sintering (SLS) 3D printer using nylon. Two iris gates were used at the top and bottom of the cylinders to separate the dense and light fluids before the start of release experiments; these top and bottom irises respectively replaced the drilled top plate and the puncturable membrane utilized in previous experimental studies (Lundgren et al. 1992; Yao 1994; Alahyari 1995).

An Oriental Motor stepper motor system (CSK266-AT) was employed to fully open the irises simultaneously and very quickly (in 0.50 seconds). The motion of the motor shaft was translated into the irises using a pinion shaft connected to a gear system. As can be seen in these figures, for Cylinder 1, one pinion was used at the top and its motion was translated to the irises using a drive cylinder. For Cylinder 2, two pinion and gear sets were employed at the top and bottom. The shaft motion, in addition to opening the irises, also rotates the 12 small cylinders inside the main cylindrical structure, each of which includes a slot that opens or closes the openings of the main cylindrical body. The top and bottom of these small cylinders are in contact with the top and bottom gears using very short pins which allow them to rotate with the rotation of these gears through a cam slot. For choosing the shape, size and number of slots in the design of Cylinder 2, three factors were considered: (1) a high value of wall porosity (opening area divided by the total wall area), (2) uniform distribution of openings throughout the cylindrical wall, and (3) a high discharge coefficient to allow the ambient fluid to easily enter the cylinder following the opening of the mechanism.

Cylinder 1　　　　　**Cylinder 2**　　　　　**Small cylinders**
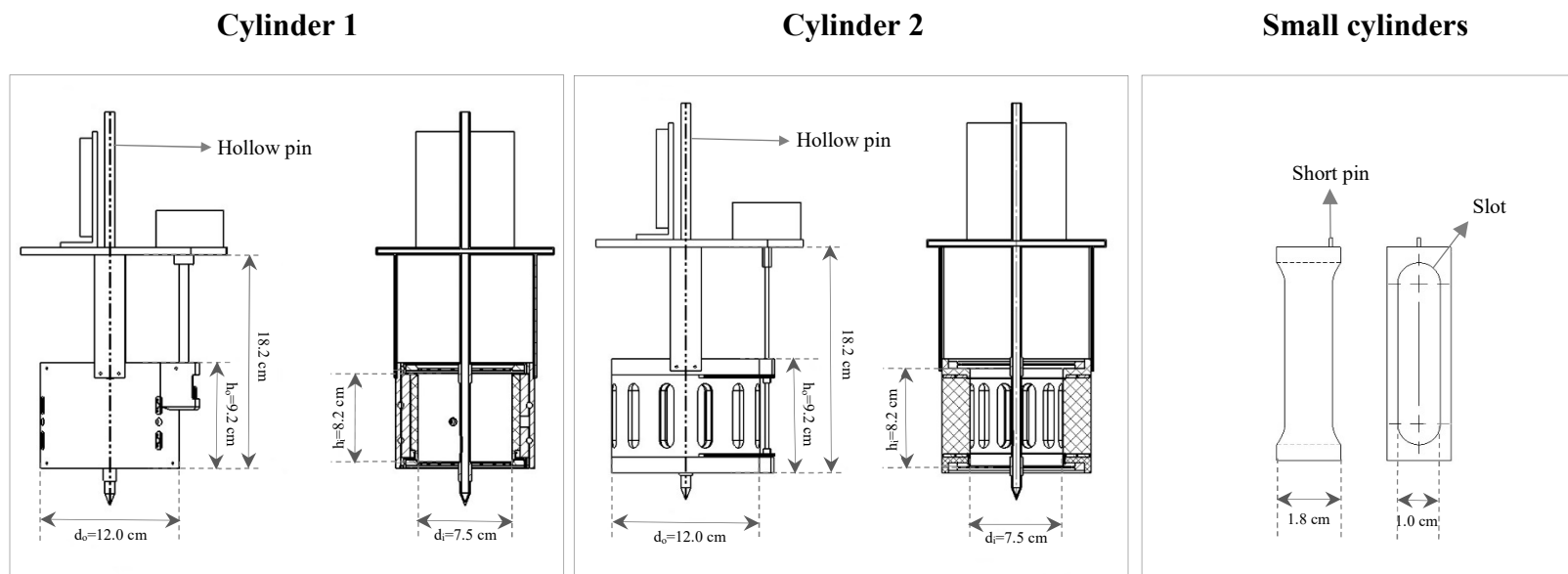
Figure 2.3: Sectional view of the two designs of dense fluid release mechanism (d_i: inside diameter, d_0: outside diameter, h_i: inside height, h_0: outside height)

The top structures of both release mechanism designs provided a platform to mount the stepper motor and its driver and keep them separated from the liquid. These structures have larger diameters and can be used for secure positioning of the cylinders in the support apparatus (Figure 2.1). It should be noted that a LabVIEW code (Appendix 1) was developed to generate the pulse train that operates the stepper motor and so the opening and closing of the cylinders can be remotely triggered.

Since the iris gates cannot fully close, a hollow cylindrical pin (inside diameter = 0.5 cm) with two large openings along its wall was utilized to seal them. Further prevention of leakage was obtained by using two pieces of latex rubber attached to each pin (Figure 2.3). These pins were attached to the centre of the top structures and were also used for filling the cylinders with the dense solution. Before the start of each release test, the mechanism was closed and then filled with 362 millilitres ($Q = h_i \frac{\pi d_i^2}{4}$) of potassium dihydrogen phosphate aqueous solution, using a funnel attached to the hollow pin. The large openings in the lower end of this pin allowed the quick filling of the cylinder. Next, the cylinder was placed in the support apparatus and immersed in the glycerol aqueous solution inside the tank.
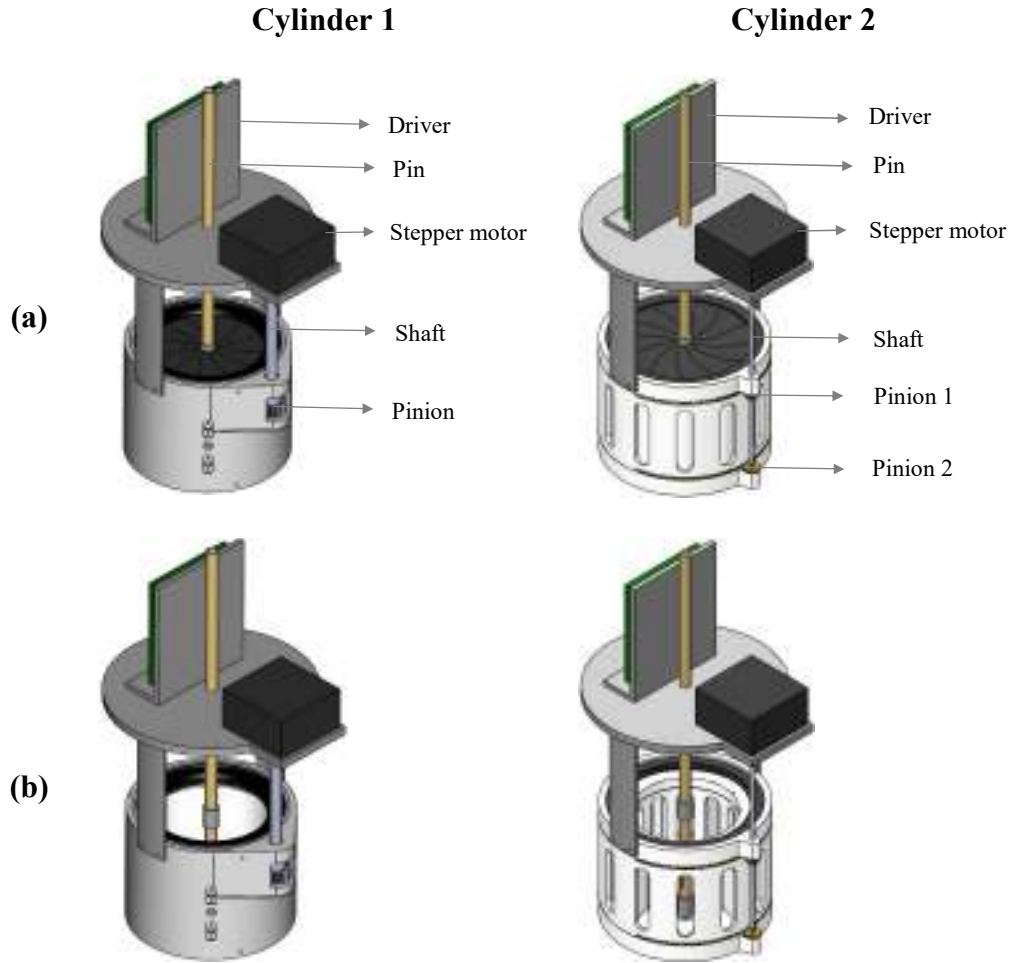
Figure 2.4: Release cylinders in (a) fully closed and (b) fully open positions

Upon quick opening of the irises, the dense fluid falls out as a single mass and, because of the full submergence of the cylinder, ambient fluid enters from the top and replaces the dense fluid inside the cylinder (in Cylinder 2, the ambient fluid can enter through the wall openings as well (porosity = 25%)). These conditions resemble the sudden acceleration of a cold air mass toward the ground in real downburst events. Moreover, since the irises open at the same speed and in the same manner each time, the inherent randomness associated with the membrane breakage was eliminated and the issue of repeatable opening was addressed. It is worth nothing that this kind of experiment requires the amount of leakage, diffusion and mixing of the two miscible solutions to be as low as possible. In these new designs, these challenges were successfully addressed by using the irises, closing hollow

pins and the latex rubber pieces; for Cylinder 2, the introduction of slots to the wall did not cause any leakage while the mechanism was fully closed.

2.2.4   Measurement technique

The PLIF method was utilized for visualization of the flow field (Ferrier et al. 1993), using an Nd:YAG laser system with a wavelength of 532 nm and a pulse frequency of 6 Hz. By a combination of cylindrical (-25 mm) and spherical (1000 mm) lenses, the laser beam formed a vertical sheet passing through the middle of the tank (Figure 2.1); the thickness (2.69 mm) and Raleigh length (21.3 m) for this laser sheet were calculated using the formulae developed by Crimaldi (2008).

As an indication of the evolution of the scalar field of the downburst event, a fluorescent dye (Rhodamine B) was added to the dense fluid and its concentration was followed after the release. This dye absorbed part of the laser energy and, after excitation, emitted light with a higher wavelength (around 590 nm) (Alahyari 1995; Arratia and Muzzio 2004). Then a 1.4 MP PowerView camera, oriented perpendicular to the laser sheet and equipped with a long-pass filter (cut-off frequency = 545 nm), was used to capture sequential images of the fluorescence emissions at 6 Hz. Each test was recorded for 25 seconds and 150 images were captured; it should be noted that the duration of each release event was much shorter than this but since capturing started before the opening of the iris gates and lasted until the dense fluid touched the side walls, using such long recording times was necessary.

A target plane was utilized to perform the two dimensional and perspective calibrations for the captured images. The size of the field of view was: $L \times H = 386.52$ mm $\times$ 287.64 mm, resulting in an image resolution of 280.9 μm/pixel.

In Figure 2.1, the major components of the PLIF system are depicted. The synchronizer was responsible for coordinating the laser pulse and image capturing. The INSIGHT 3G^{TM} software (TSI Inc. 2008, Shoreview, USA) was used to acquire, analyze and display the captured PLIF images.

2.2.5 PLIF calibration

The intensity of the fluorescent emission is a function of the incident laser intensity and the concentration of fluorescent dye (Alahyari 1995). The energy level of the laser pulses was kept constant (100 mJ/pulse) for all the calibration and release experiments. However, since the laser intensity varies throughout the vertical sheet, a set of calibration experiments was conducted to correlate the fluorescent intensity with the location within the laser sheet and the dye concentration. The results of such a calibration process can be used to determine the scalar concentration of the fluorescent dye at every pixel of the sequential images taken during the release experiments (Crimaldi and Koseff 2001; Crimaldi 2008).

In this regard, a narrow glass box (L × W × H = 52.2 cm × 2.4 cm × 35.5 cm) was placed inside the main tank in a way that its largest face covered the entire field of view of the camera and the narrow side walls were aligned with the vertical laser sheet. Seven different aqueous solutions of Rhodamine B (with the concentrations of 0, 0.05, 0.1, 0.15, 0.2, 0.25, 0.3 mg/L) were used inside the glass box and, for every concentration, five calibration images were taken and averaged to produce a reference image for that concentration. The average image for the solution with the concentration of zero was used as the background image.

It should be emphasized that all measurement conditions and camera settings were kept the same as those for the actual release experiments. The maximum concentration used for the calibration (0.3 mg/L) was equal to the concentration of Rhodamine B in the dense fluid inside the cylinder (which was the same for all release tests), and the camera aperture was adjusted in a way to achieve the highest pixel intensity for this concentration (around 4000 for the 12-bit camera). The mean intensities of the average calibration images were correlated to the corresponding concentrations and a linear relationship was obtained ($R^2 =$ 0.994).

The relative concentration of Rhodamine B at every pixel of the sequential images can be calculated using Equation (2.5):

$$C_{relative} = \frac{C - C_{background}}{C_{maximum} - C_{background}} \qquad (2.5)$$

In this equation, C, $C_{background}$ and $C_{maximum}$ represent the concentration of each pixel in the captured image, the concentration of the corresponding pixel in the background image (which is zero), and the maximum concentration used in the experiments (the initial concentration of the fluorescent dye in the dense fluid, 0.3 mg/L), respectively. Because of the above-mentioned linear relationship between the concentration and the fluorescence intensity, the relative concentration can also be expressed as Equation (2.6) (Ferrier et al. 1993; Crimaldi and Koseff 2001).

$$C_{relative} = \frac{I - I_{background}}{I_{maximum} - I_{background}} \qquad (2.6)$$

I, $I_{background}$ and $I_{maximum}$ respectively refer to the intensity of each pixel in the captured image, the intensity of the corresponding pixel in the background image (which is not zero and can be obtained from the average background image), and the intensity of the corresponding pixel in the average calibration image of the highest concentration used (0.3 mg/L). It is obvious that the value of the relative concentration varies between 0 and 1.

The INSIGHT 3G^{TM} software provided a platform to process the calibration images and display the sequential PLIF pictures based on the relative concentration of each pixel instead of the fluorescent intensity. The unique features of this calibration platform allowed the reference images to be corrected for the possible errors including: pulse-by-pulse laser energy variations, attenuation of the laser energy due to absorption, and reflection and scattering effects. The effects of other error sources like camera noise and photobleaching were assumed to be negligible.

2.2.6 Experimental design

The specifications of different release experiments conducted in this study are presented in Table 2.1. These tests, based on the motives for conducting them, can be divided into three groups:

(1) Test 1 and Test 2: the purpose was to investigate how different wall designs influence the flow field of the simulated downbursts; thus, all experimental conditions, other than the release mechanism, were kept the same.

(2) Test 2, Test 3 and Test 4: this group of tests was aimed at examining the validity of the Lundgren et al. (1992) scaling parameters for the current setup. In this regard, the same release mechanism, initial release height and ambient fluid concentration were used in all the tests. Various concentrations of the heavy fluid were employed and, consequently, different values for $\Delta\rho/\rho_a$ were obtained: 1.95, 3.37 and 5.51%. Then, the resultant scaled flow fields were compared.

As described in the introduction, choosing a small density difference value was necessary for the application of the Boussinesq approximation. Thus, these three small quantities, which are similar to those used in the previous two-fluid experiments (Yao 1994; Alahyari 1995) and also to the average values calculated for the CS numerical simulations (Oreskovic 2016), were selected.

(3) Test 2, Test 5 and Test 6: these tests were conducted with the same release mechanism and density differences; the only distinction between them is their initial release height which refers to the distance between the lower end of the cylinder (bottom iris gate) and the tank floor (H_0). This value was adjusted using the cylinder support apparatus which allowed three different values of H_0/R_0: 2.42, 3.26 and 3.62. These ratios are similar to those used in the experimental studies by Lundgren et al. (1992) and Yao (1994); the results of their investigations demonstrated that such ratios are in agreement with the typical height of a thunderstorm cloud base (1830 m) at the time of the downburst event (Fujita 1986).

To avoid the variations of ambient fluid concentration in different release tests, a large volume of glycerol solution was prepared, and a portion of it was used for each test. In this way, a constant value of concentration (and density) were maintained throughout the experiments. The same method was applied for the dense fluids in Tests 1, 2, 5, and 6 which had similar concentrations of potassium dihydrogen phosphate (Table 2.1). In this case, Rhodamine B was also added to this large volume of dense fluid (to a concentration of 0.3 mg/L) to keep a consistent fluorescent dye concentration and avoid errors arising from its variations for different experiments.

One major source of uncertainty in the previous experimental studies of downbursts was the unpredictable breakage of the membrane covering the bottom of the cylinder at the time of release. This problem added a randomness factor to the way the dense fluid fell out each time. Moreover, the disturbance caused by the membrane puncturing using a needle led to the creation of an obscure interface between the dense and light fluids in the very early stages of the fall out (Yao 1994; Alahyari 1995). The current design, by replacing the membrane with the bottom iris gate which opens in a consistent manner and speed, eliminated this randomness factor and resolved all the uncertainties associated with the opening.

Another issue in previous studies was the uncertainty in the concentration of dense fluid prior to the release. For example, Yao (1994) and Lundgren et al. (1992) first submerged the cylinder in the ambient fluid and then used a hollow tube to fill it with the dense solution by displacing the ambient fluid which was already inside the cylinder. Alahyari and Longmire (1994) and Alahyari (1995) also used the same cylinder design, but filled it outside the main tank and slowly lowered it to immerse it in the ambient fluid. It is apparent that both these methods introduce a significant error in the initial dense fluid concentration because of all the diffusion and mixing that may occur. The features of the new release mechanisms, as discussed in 2.3, considerably minimize the mixing, leakage, diffusion and, consequently, any change in the concentration and density of the dense solution.

2.3 Results and discussion

2.3.1 Downburst simulation

In Figure 2.5, calibrated PLIF images illustrate the qualitative evolution of the downburst flow field for one of the release tests. In these sequential images, various stages of the life cycle of a simulated downburst (including acceleration toward the ground, formation of the vortex ring, impact upon the ground, and the outflows following this touchdown) can be clearly seen. Cylinder 2 was used as the release mechanism in this experiment and a line representing the tank floor was added to the calibrated images. Other specifications of this release test are provided in Table 2.1.

t = 0 s

t = 2.17 (5.92 T_0) s

t = 0.50 (1.37 T_0) s

t = 2.83 (7.75 T_0) s

t = 1.00 (2.73 T_0) s

t = 3.67 (10.03 T_0) s

t = 1.67 (4.56 T_0) s

t = 4.33 (11.85 T_0) s

$C_{relative} = 0$ $C_{relative} = 1$
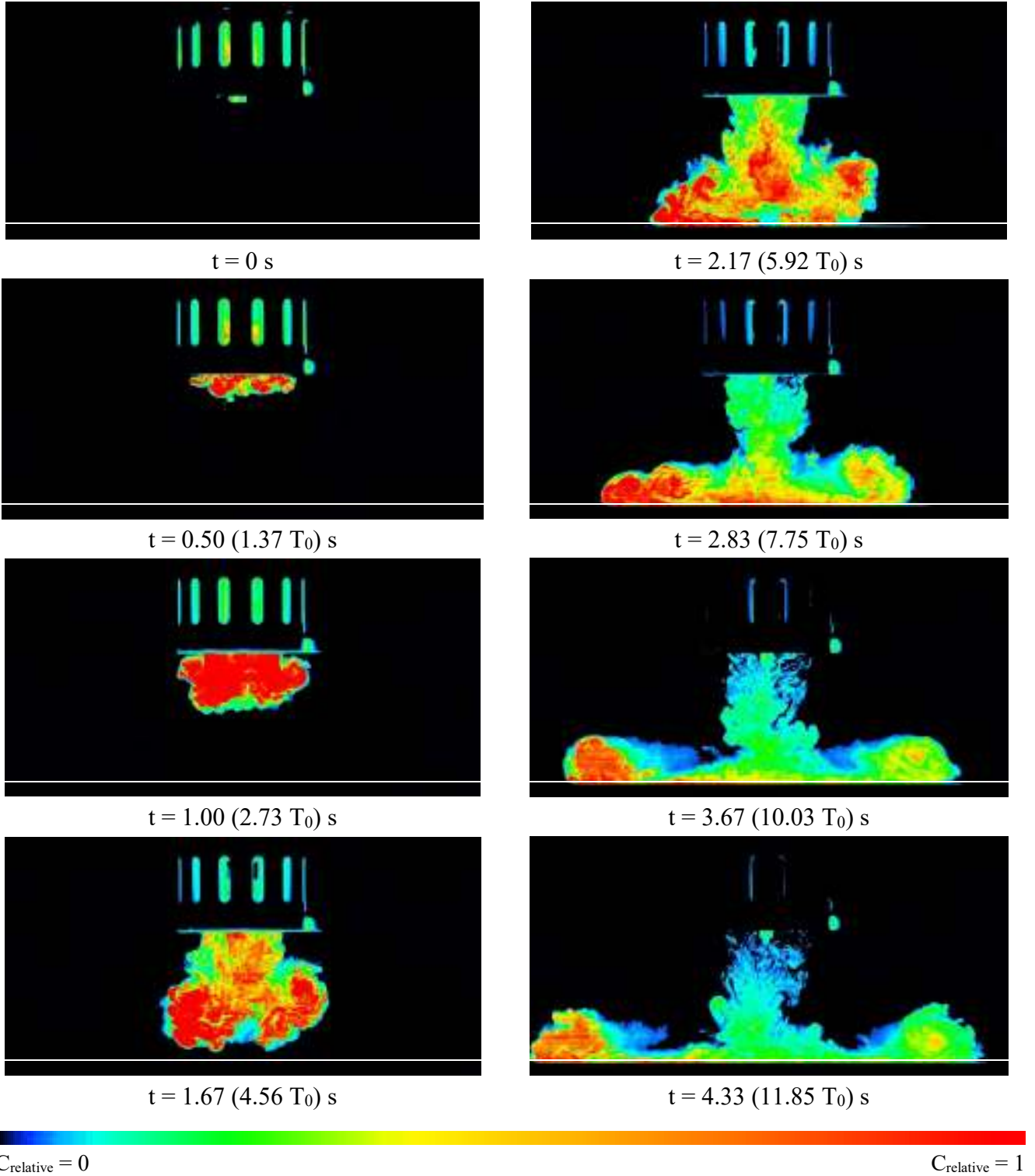
Figure 2.5: Time series of the calibrated PLIF images captured during Test 6

In this figure, t = 0 s refers to the time at which the release mechanism was fully open, but the dense fluid was still inside it. According to the experimental details, the time required to open the irises and wall slots was 0.50 s; this was calculated via dividing the inside diameter of the irises by the opening speed, which was specified in the LabVIEW code. In Figure 2.6, the process of quick opening of the release cylinder is demonstrated using the calibrated PLIF images taken prior to t = 0 s.

t = -0.50 s (triggering the stepper motor)

t = -0.33 s

t = -0.17 s

t = 0 s
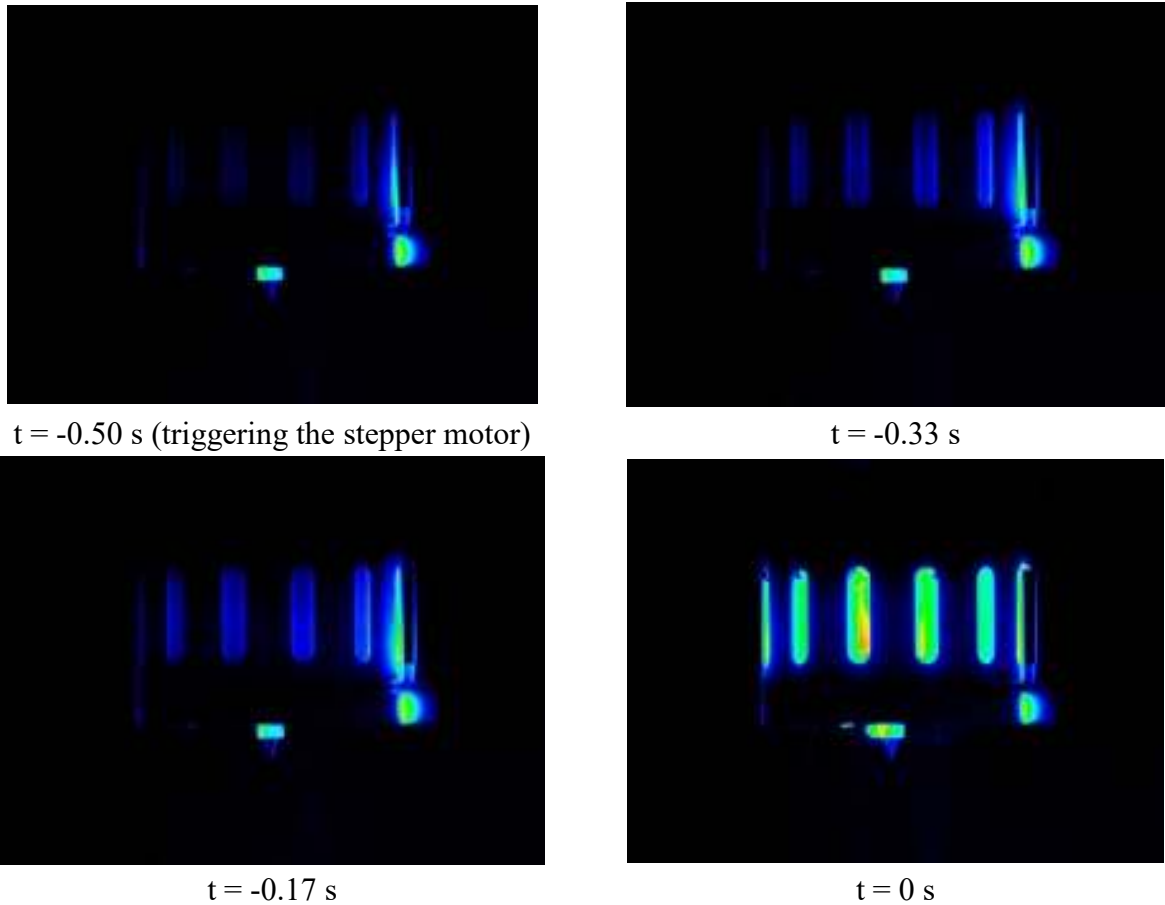
Figure 2.6: Opening stages of Cylinder 2 in 0.50 s

In order to evaluate the performance of the new release cylinders with regard to repeatability, Test 2 was repeated three times and variations of intensity at certain pixels were tracked during each repetition. Figure 2.7(a) shows the physical locations of these selected pixels within the field of view of the camera. (P2, P3) and (P4, P5) are in symmetrical positions and P1 is located under the centre of the lower iris. In Table 2.2, the

coordinates of these points are given. Roberto et al. (2014) computationally investigated the two-fluid downburst experiments, using the Unsteady Reynolds-Averaged Navier-Stokes (URANS) model, and found the locations of points where the peak radial velocity occurs to be at $2.55R_0$ from the cylinder axis and $0.2R_0$ from the ground; in Figure 2.7(a), P2 and P4 represent these peak radial velocity points.

Table 2.2: Coordinates of the selected pixels in the PLIF images

	Pixel position in the image (X, Y)	r [a] (cm)	z [a] (cm)
P1	(674,500)	0	14.7
P2	(274,993)	-11.3	0.9
P3	(48,980)	-17.6	1.2
P4	(1074,993)	11.3	0.9
P5	(1300,980)	17.6	1.2

[a] r and z are defined in Figure 2.7(a)

In Figure 2.7(b), the time variations of pixel intensity at P1, P2 and P3 for all the repetitions are presented in one graph. Moreover, for investigating the symmetry of the flow field, pixel intensities at P3 and P5 are compared in Figure 2.7(c). R in the graph legends refers to the repetition test number.

For P1, P2 and P3, the standard deviation (σ) and coefficient of variation (CV) of the three repetitions were calculated at each time. The highest values obtained for these parameters are 260 and 0.19, respectively. These numbers, along with the data presented in Figure 2.7(c), suggest a very good agreement between the repetitions and support the claim that the current experimental setup has the capability to produce repeatable and symmetric flow fields.
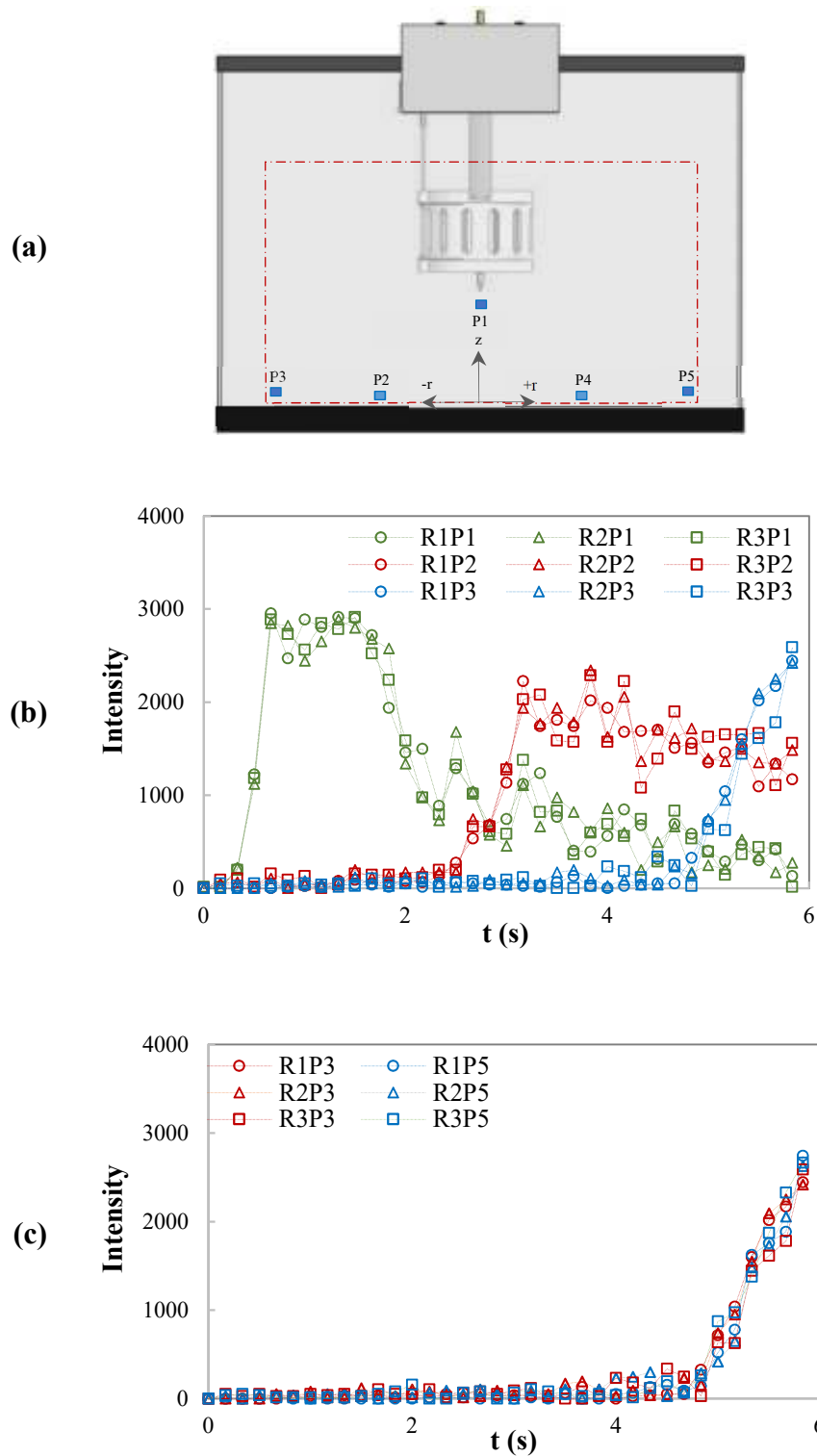
Figure 2.7: (a) Positions of the selected pixels, (b) time series of pixel intensity for all the repetitions, (c) time series of pixel intensity at the two sides of release cylinder

For comparing the effect of different parameters examined in this study (cylinder wall design, density difference and initial release height), variations of the shape of the descending dense fluid parcel with time was monitored during each release test. In this regard, two variables were defined: (1) the average radius of the vortex ring that is half of the maximum horizontal width of the outflow (R), and (2) the distance between the downburst front and the ground (H). Figure 2.8 displays the methods of measuring these parameters. For this purpose, an image analysis software (Digimizer) was utilized; first, a known length value was specified as a scale factor, and then the diameter of the vortex ring (W = 2R) and its frontal height were computed by the software (based on the scale factor). The boundary of the outflow was clearly distinguishable from the surroundings and was determined by eye. Both defining the scale factor for each image and specifying the boundaries are subject to personal error. Thus, an uncertainty of ±2% for detection of the outflow boundaries and ±1% for assigning the scale factor were considered and, by applying the total uncertainty formula (Coleman and Steele 2009), a value of ±2.2% was obtained for the uncertainty in the measurement of R and H.
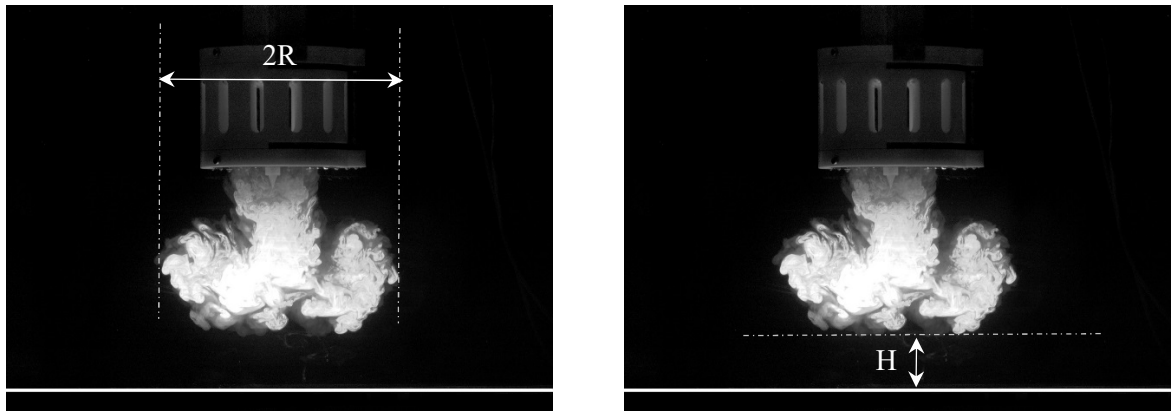
Figure 2.8: Calculation of R and H for a simulated downburst

Variations of these parameters with time for the three repetitions of Test 2 are presented in Figures 2.9(a)-(b). Following the quick opening of the irises and wall slots, a shear layer forms between the falling liquid parcel and the ambient fluid and the dense fluid rolls up to create a horizontal vortex. The radius of this vortex ring increases at a constant rate until impacting on the ground (H = 0 cm at t = 2.67 s), whereupon its rate of change increases. These figures also show how the vortex dimensions are the same for all of the repetitions

and support the finding that the new design of release mechanism can successfully produce repeatable results, the maximum value of standard deviation for R and H are 0.27 cm ($\approx$ $0.04d_i$) and 0.23 cm ($\approx 0.03d_i$), respectively. By replacing the membrane with the iris gate, the initial disturbances caused by membrane breakage, as reported by Yao (1994), were eliminated and a clear interface between the two fluids was obtained, making the initial measurements of R and H more reliable.

(a)   (b)
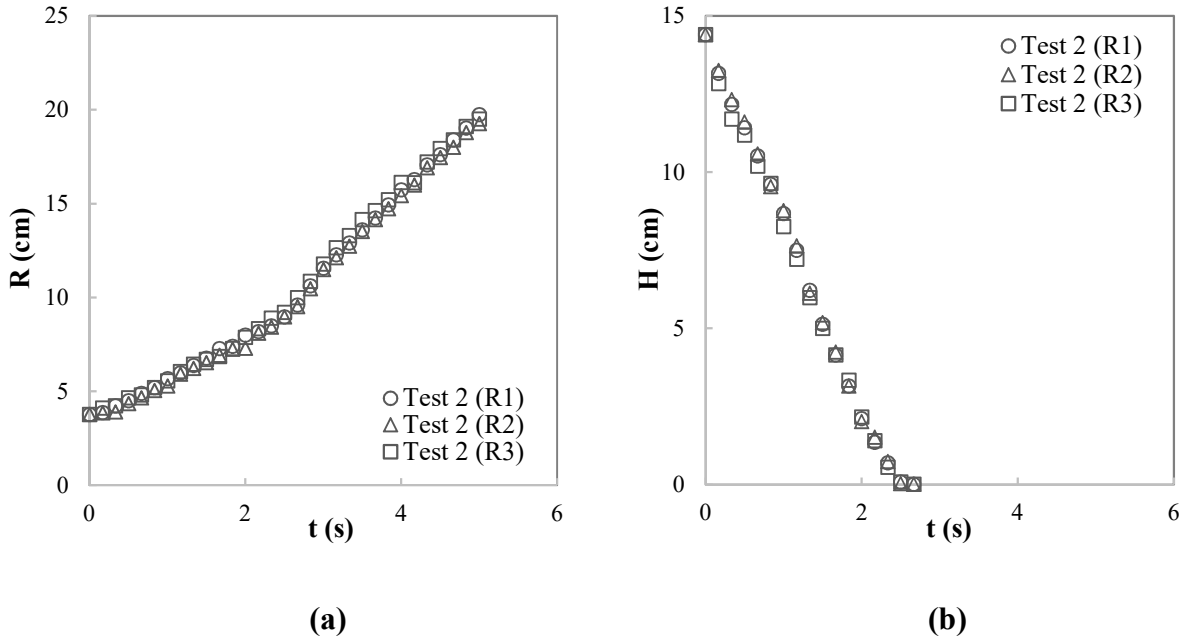
Figure 2.9: Variations of (a) R and (b) H with time for the three repetitions of Test 2

The average radial speed ($\overline{\frac{dR}{dt}}$) and the average vertical speed ($\overline{\frac{dH}{dt}}$) of the outflow front were calculated using the data in Figures 2.9(a)-(b). These speeds can also be expressed in dimensionless forms (Equations (2.7) and (2.8)).

$$\overline{\frac{d(R/R_0)}{d(t/T_0)}} = \frac{T_0}{R_0}\overline{\frac{dR}{dt}} = \frac{1}{V_0}\overline{\frac{dR}{dt}} \tag{2.7}$$

$$\overline{\frac{d(H/R_0)}{d(t/T_0)}} = \frac{T_0}{R_0}\overline{\frac{dH}{dt}} = \frac{1}{V_0}\overline{\frac{dH}{dt}} \tag{2.8}$$

In Table 2.3, all these values are presented for Test 2.

Table 2.3: Radial and vertical speeds of the simulated downburst outflow in Test 2

$\dfrac{d\overline{R}}{dt}_{BT}$ (cm/s)	2.21
$\dfrac{d\overline{R}}{dt}_{AT}$ (cm/s)	4.10
$\left\|\dfrac{d\overline{H}}{dt}\right\|$ (cm/s)	5.71
R_0 (cm)	4.42
T_0 (s)	0.37
V_0 (m/s)	12.09
$\dfrac{1}{V_0}\dfrac{d\overline{R}}{dt}_{BT}$	0.183
$\dfrac{1}{V_0}\dfrac{d\overline{R}}{dt}_{AT}$	0.339
$\left\|\dfrac{1}{V_0}\dfrac{d\overline{H}}{dt}\right\|$	0.472

2.3.2   The effect of cylinder wall design on the flow field

For analyzing the influence of the cylinder wall openings on the simulated downburst, the results of Tests 1 and 2 are compared to each other in Figures 2.10(a)-(b). In these graphs, the shape parameters and time were normalized by the characteristic length (R_0) and time (T_0), respectively, to make them dimensionless. The value of R_0 is constant for all of the release tests and, because the density difference is the same in Tests 1 and 2, the value of T_0 is also the same (Table 2.1).

(a)   **(b)**
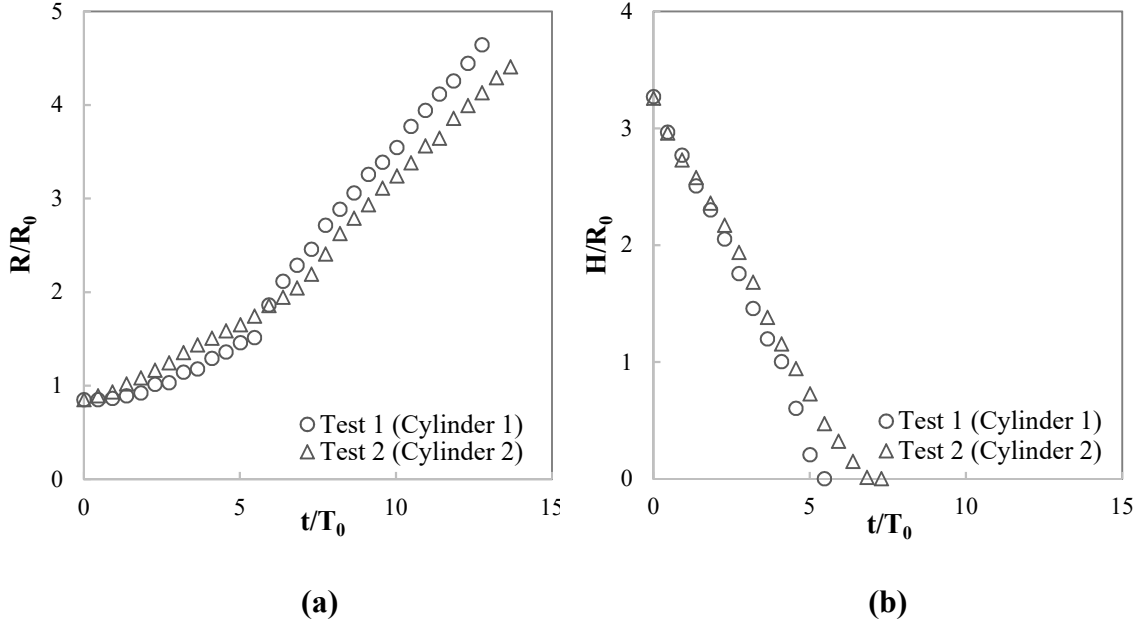
Figure 2.10: Time variations of dimensionless shape parameters for different release mechanisms

Figure 2.10(b) shows that the dense fluid parcels in Test 1 and Test 2 reached the ground at t = 2 s (t/T_0 = 5.47) and t = 2.67 s (t/T_0 = 7.29), respectively. For Test 1, the values of $\overline{\frac{d(R/R_0)}{d(t/T_0)}}$ for the before and after-touchdown periods are 0.131 and 0.408, respectively. By comparing these numbers to the corresponding values in Test 2 (Table 2.3), it can be said that prior to impacting on the ground, the maximum downburst radius and its growth rate in Test 1 are lower than those in Test 2. However, after the impact, both the magnitude of the radius and its rate of increase are higher. In other words, the difference between the rates of change of radius before and after the ground touchdown is more significant in Test 1 (Figure 2.10(a)). The average value of the dimensionless vertical speed ($\overline{|\frac{d(H/R_0)}{d(t/T_0)}|}$) for Test 1 (0.596) is also higher than that in Test 2 (0.472).

Figure 2.11 clearly displays the above-mentioned differences between these two tests prior to ground impingement. It can be observed that after equal times have elapsed following the opening of the release mechanism, the dense fluid volume leaving Cylinder 1 travels a greater distance in comparison to that leaving Cylinder 2. The higher downburst radius values in Test 2 can also be seen from these images. Another obvious difference between

these experimental simulations is that the dense fluid in Cylinder 1 falls as a more uniform mass unlike that in Cylinder 2 which falls as a non-uniform and mixed volume. Since the only distinction between these tests is the design of the cylinder wall, it can be inferred that the introduction of 12 slots into the wall results in a higher degree of mixing between the lighter and heavier liquids. For two-fluid downburst simulations, it is well established, by Lundgren et al. (1992), that the light fluid penetrates the vortex from above and becomes mixed with the dense fluid as the vortex descends. This phenomenon occurs in both Test 1 and Test 2, but it can be said that for Cylinder 2, additional mixing forces act prior to the formation of the shear layer between the light and dense fluids which leads to a lower average density of the falling mass and, consequently, a slower movement toward the ground.

Cylinder 1   **Cylinder 2**

$t = 0.83$ (2.28 T_0) s $t = 0.83$ (2.28 T_0) s

$t = 1.33$ (3.65 T_0) s $t = 1.33$ (3.65 T_0) s

$C_{relative} = 0$ $C_{relative} = 1$
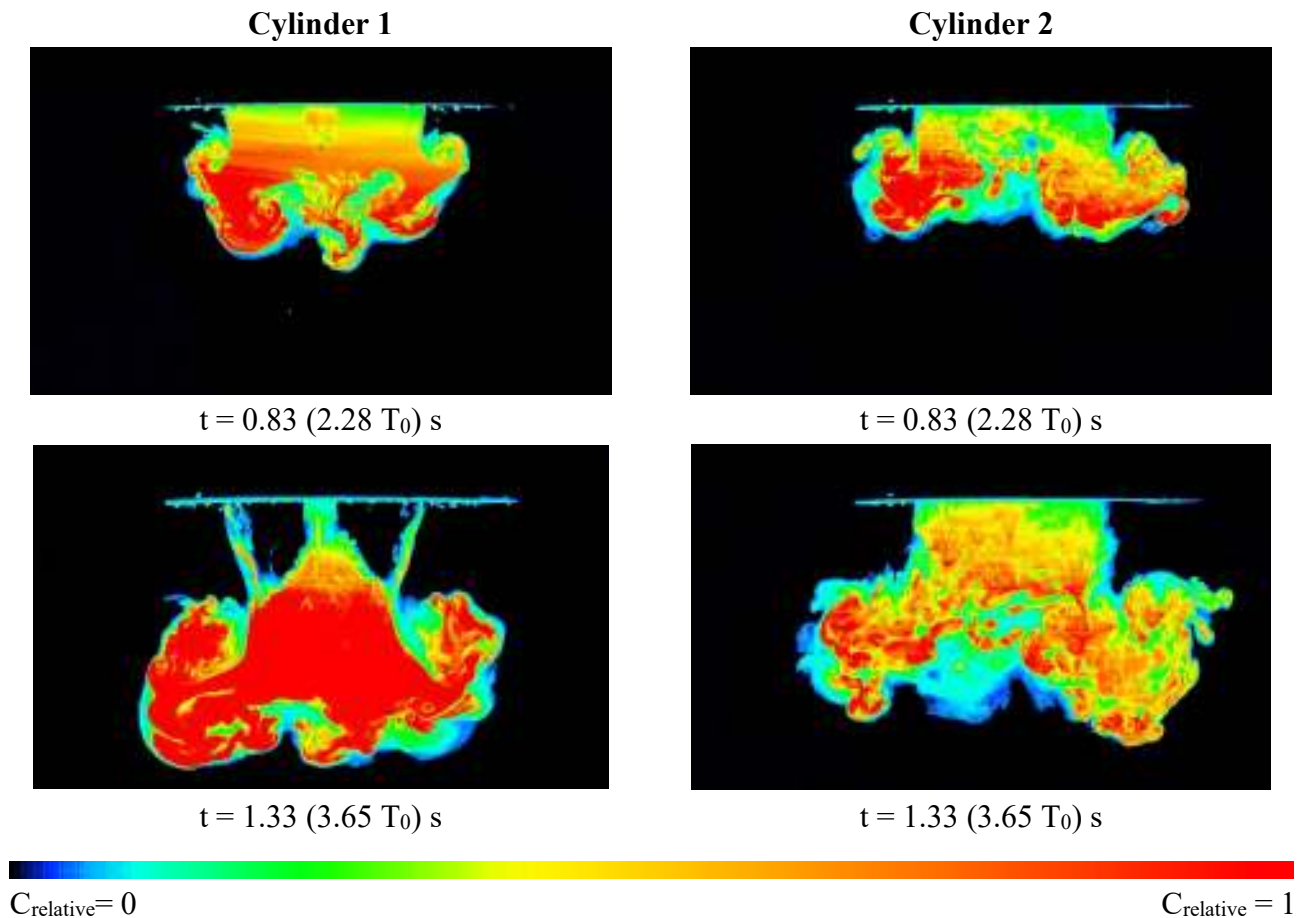
Figure 2.11: The effect of release cylinder wall design on the shape of vortex

In Figure 2.12(a)-(b), the dimensionless radius and height of the downbursts in Tests 1 and 2 are compared to the published data (Lundgren et al. 1992; Alahyari 1995). The key experimental specifications of each data series are presented in Table 2.4.

(a)   (b)
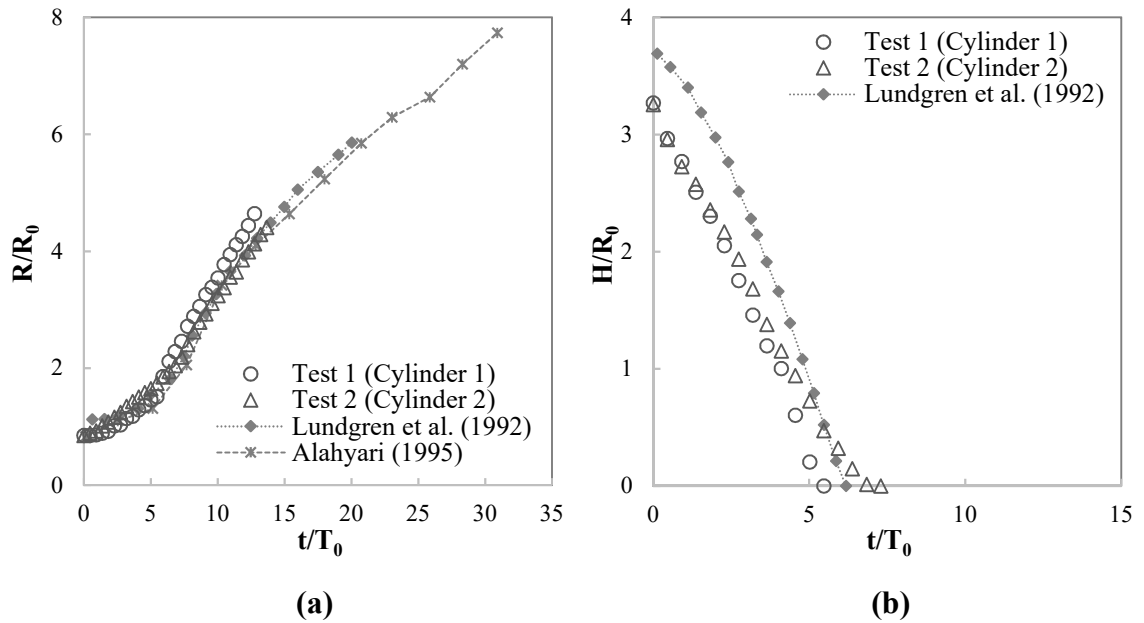
Figure 2.12: Comparison of the dimensionless flow fields of the present work (Tests 1 and 2) with the literature data

Table 2.4: Key parameters used in the experimental studies of Figure 2.12

	Lundgren et al. (1992)	Alahyari (1995)	Tests 1	Test 2
Ambient fluid	Fresh water	Glycerol solution	Glycerol solution	Glycerol solution
Dense fluid	Salt water	Potassium dihydrogen phosphate solution	Potassium dihydrogen phosphate solution	Potassium dihydrogen phosphate solution
Cylinder wall design	Solid wall	Solid wall	Solid wall	Wall with 12 slots
Cylinder height to diameter ratio	1	1.37	1.09	1.09
R_0 (cm)	3.40	3.88	4.42	4.42
H_0/R_0	3.81	3.81	3.26	3.26
h_{top}/R_0	5.3	2	2	2
$\Delta\rho/\rho_a$ (%)	5	5	3.37	3.37

Based on these figures, it can be said that the general trends of change of the scaled geometrical parameters are in good agreement. Lundgren et al. (1992) quantified the radial spread of the downburst front and reported a linear speed of $0.16V_0$ prior to the ground impact. For the after-touchdown period, they reported an initial maximum radial front speed of $0.5V_0$ which then decreased to a constant value of $0.2V_0$. The average value of vertical front speed in their study was calculated to be $0.64V_0$. These numbers are comparable to the corresponding values in Test 1; it should be noted that, with respect to the wall design, the cylinder used by Lundgren et al. (1992) was more similar to Cylinder 1 which was used in Test 1. Another important point is that, the size of the ambient fluid tank used by Lundgren et al. (1992) and Alahyari (1995) was bigger than the one used in this study. Thus, the radius values were monitored for a longer time period and the deceleration phase ($0.5V_0$ to $0.2V_0$) was recorded; but for the current setup, only a short period of time was captured following the ground touchdown.

2.3.3 The effect of density difference on the flow field

One of the goals of this study was to examine the effectiveness of the Lundgren et al. (1992) scaling parameters for the setup utilized to conduct the current release experiments. Based on this scaling law, as long as the only difference between the release tests is the value of density difference, the resultant dimensionless flow field should remain unchanged. The reason for such behaviour is that the influence of $\Delta\rho/\rho_a$, g and R_0 are considered in the calculation of time scale (Equation (2.2)).

As discussed in the experimental design, the release tests in the second group (Tests 2, 3 and 4) meet the above conditions. The concentration of ambient fluid is the same for all of these experiments, but different concentrations were used for the dense fluid resulting in different $\Delta\rho/\rho_a$ and T_0 values (Table 2.1). Figures 2.13(a)-(b) illustrate the effect of the density difference on the time variations of R and H. These figures show that by increasing the value of density difference between the two fluids, the rate of evolution of the outflow also increases. For instance, the time required for the downdraft front to reach the ground for the density differences of 1.95%, 3.37% and 5.51% are 3.50 s, 2.67 s and 2.00 s, respectively. As another example, the value of R, at t = 2.00 s, for these density differences are 6.82 cm ($1.54R_0$), 7.71 cm ($1.74R_0$) and 9.60 cm ($2.17R_0$), respectively.
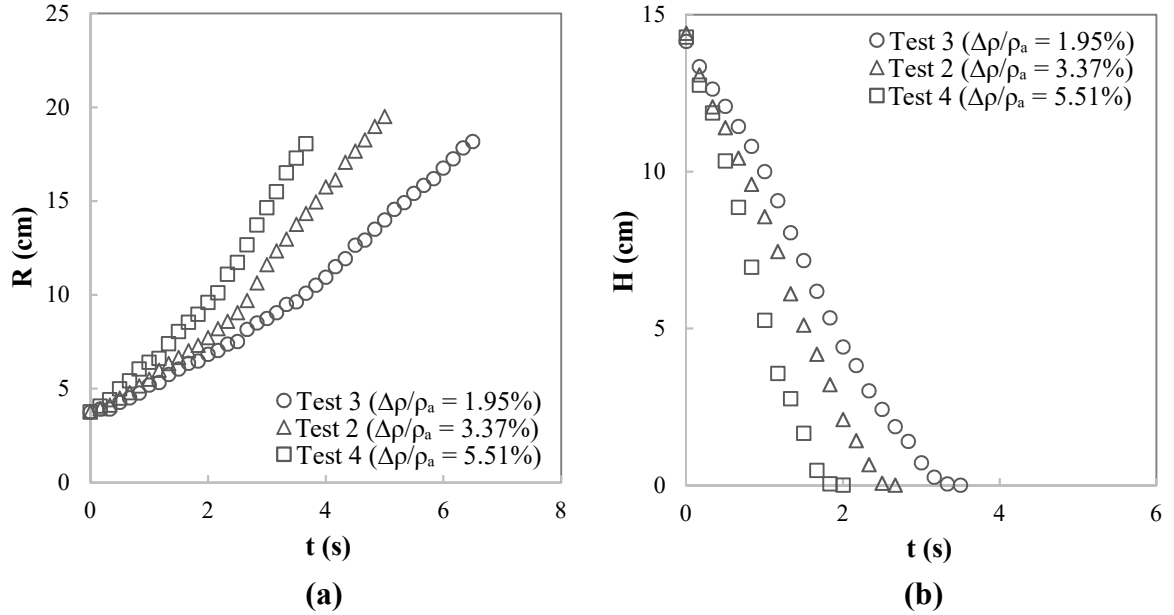
Figure 2.13: Time variations of shape parameters for various density differences

To calculate the dimensionless flow field for each density difference, the values of R, H and t were divided by the corresponding R_0 and T_0, and Figures 2.14(a)-(b) were obtained.
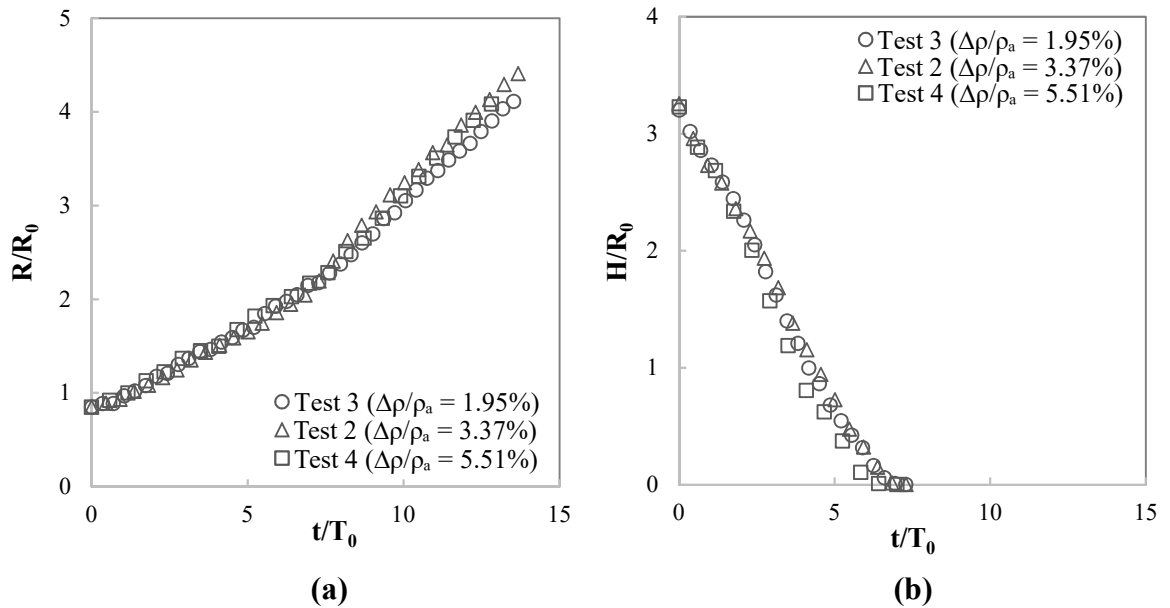
Figure 2.14: Time variations of dimensionless shape parameters for various density differences

In Table 2.5, the radial and vertical speeds of the downburst outflow are presented for various density differences.

Table 2.5: Radial and vertical speeds of the downburst front for the three density differences

	Test 3	Test 2	Test 4
$\Delta\rho/\rho_a$ (%)	1.95	3.37	5.51
V_0 (cm/s)	9.20	12.09	15.46
$\frac{dR}{dt}_{BT}$ (cm/s)	1.75	2.21	2.95
$\frac{dR}{dt}_{AT}$ (cm/s)	2.88	4.10	5.27
$\left\|\frac{dH}{dt}\right\|$ (cm/s)	4.41	5.71	7.79
$\frac{1}{V_0}\frac{dR}{dt}_{BT}$	0.190	0.183	0.191
$\frac{1}{V_0}\frac{dR}{dt}_{AT}$	0.313	0.339	0.341
$\left\|\frac{1}{V_0}\frac{dH}{dt}\right\|$	0.479	0.472	0.504

Based on Figure 2.14 and Table 2.5, it can be said that the dimensionless flow field of release experiments with different $\Delta\rho/\rho_a$ values are in a good agreement with each other, confirming the validity of the scaling rule, developed by Lundgren et al. (1992), for the current setup.

2.3.4   The effect of release height on the flow field

To investigate the role of initial release height (H_0) on the simulated downbursts, all experimental conditions except the release height were kept the same. The results of Tests 2, 5 and 6 were used in this regard (the third group of release tests in the experimental design). In Figures 2.15(a)-(c), the dimensionless flow field of these release experiments are compared.
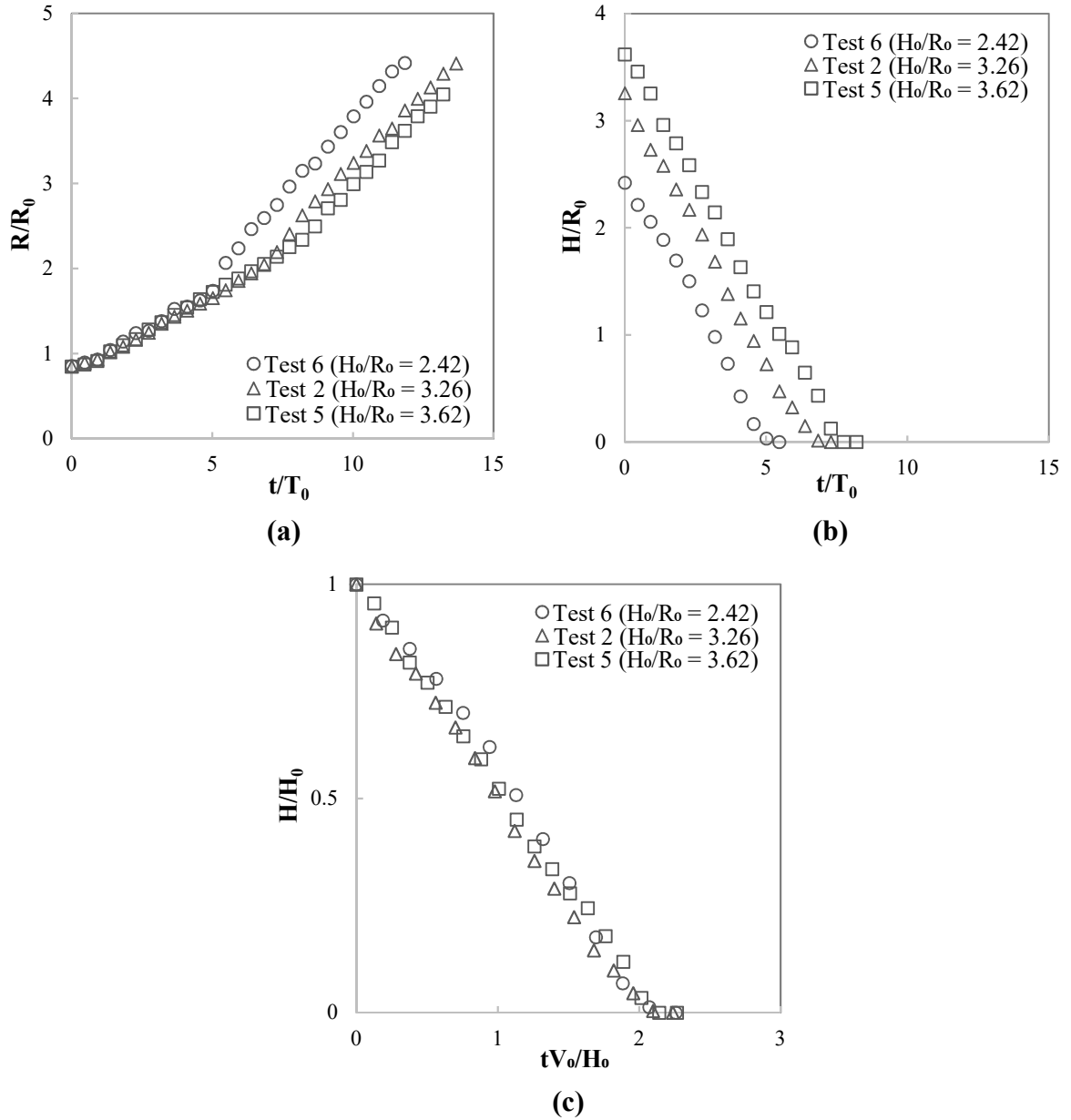
Figure 2.15: Time variations of dimensionless shape parameters for different release heights

From these graphs, it is clear that by decreasing the release height, the time required for the dense fluid to touch the ground decreases while the rate of change of radius for the after-touchdown period remains the same for all the three release heights (Table 2.6). Moreover, Figure 2.15(c) shows how multiplying the vertical and horizontal axes in Figure 2.15(b) by R_0/H_0 results in the collapse of data for experiments with different H_0 values.

Table 2.6 Dimensionless radial and vertical speeds of the downburst front for different release heights

	Test 6	Test 2	Test 5
H_0/R_0	2.42	3.26	3.62
$\dfrac{1}{V_0}\dfrac{d\overline{R}}{dt}_{BT}$	0.201	0.183	0.188
$\dfrac{1}{V_0}\dfrac{d\overline{R}}{dt}_{AT}$	0.372	0.339	0.343
$\left|\dfrac{1}{V_0}\dfrac{d\overline{H}}{dt}\right|$	0.480	0.472	0.466

These observations are in agreement with the results of related experimental and numerical investigations which suggest that by formation of a fully-developed vortex, the after-touchdown flow field becomes release height independent (Lundgren et al. 1992; Yao 1994; Alahyari 1995). According to the literature, the descending and spreading phases for release experiments with $H_0/R_0 > 1.9$ are similar. As can be seen from Table 2.6, all the initial release heights used in this study were greater than $1.9R_0$, thus the speed and manner of propagation following the ground impingement was not affected by different H_0 values.

2.4   Summary

In this study, thunderstorm downbursts were successfully simulated in the laboratory using the two-fluid model. The major focus was on the design of a novel facility to hold the dense fluid and the evaluation of its performance in addressing the issue of repeatability and wall effect reduction. These improvements were made in two stages: in the first design, the thin membrane, used in previous studies, was replaced by quickly opening iris diaphragms at both ends of the release cylinder and a second design added porosity to the cylindrical wall.

Aqueous solutions of glycerol and potassium dihydrogen phosphate were used as light and dense fluids, respectively, whilst the addition of a fluorescent dye (Rhodamine B) to the dense fluid allowed the application of the PLIF method for quantifying the resultant scalar field within the downburst. The different stages of downburst evolution were identified and the variations of downburst radius and frontal height with time were tracked using the calibrated PLIF images.

Three trials of a single test were carried out and it was demonstrated that the iris gates can produce repeatable and symmetric results. An evident difference was observed between the flow fields of the two release mechanisms; the mixing caused by the introduction of cylinder wall slots resulted in a lighter and non-uniform descending fluid mass, longer touchdown times and slower growth rates for the radius of downburst after impacting on the ground. By creating various density differences and employing the Lundgren et al (1992) scaling parameters, the dimensionless flow fields were compared and the results showed a collapse of the data. Different values of initial release height were tested and a similar propagation behaviour was observed within the after-touchdown period.

Since the main purpose of this research work was to introduce a new design of release facility for the two-fluid model, the experiments were conducted in a small tank. The next step of this project will be dedicated to the application of these release mechanisms in a large hydraulic flume to eliminate the wall confinement issue associated with a small tank and also to implement thunderstorm translation by traversing the release mechanisms at the same freestream speed as the ambient flume flow.

2.5   References

Aboshosha H, Bisuamlak G, El Damatty A (2015) Turbulence characterization of downbursts using LES. J Wind Eng Ind Aerodyn 136:44-61

Alahyari AA (1995) Dynamics of laboratory simulated microbursts. PhD Dissertation, University of Minnesota

Alahyari AA, Longmire EK (1994) Particle image velocimetry in a variable density flow: application to a dynamically evolving microburst. Exp Fluids 17:434-440

Arratia PE, Muzzio FJ (2004) Planar laser-induced fluorescence method for analysis of mixing in laminar flows. Ind Eng Chem Res 43:6557-6568

Bluestein HB (2007) Advances in applications of the physics of fluids to severe weather systems. Rep Prog Phys 70:1259-1323

Coleman HW, Steele W (2009) Experimentation, validation, and uncertainty analysis for engineers, 2nd edn. Wiley, New York, USA

Crimaldi JP (2008) Planar laser induced fluorescence in aqueous flows. Exp Fluids 44:851-863

Crimaldi, JP, Koseff, JR (2001) High-resolution measurements of the spatial and temporal scalar structure of a turbulent plume. Exp Fluids 31:90-102

Darwish MM, El Damatty AA (2011) Behaviour of self-supported transmission line towers under stationary downburst loading. Wind Struct 14:481-498

Eilts MD, Doviak RJ (1987) Oklahoma downbursts and their asymmetry. J Climate Appl Meteor 26:69-78

Ferrier AJ, Funk DR, Roberts PJW (1993) Application of optical techniques to the study of plumes in stratified fluids. Dyn Atmos Oceans 20:155-183

Fujita TT (1985) The downburst. The University of Chicago Press, Chicago, USA

Fujita TT (1986) DFW downburst. The University of Chicago Press, Chicago, USA

Hjelmfelt MR (1987) Structure and life cycle of microburst outflows observed in Colorado. J Appl Meteorol 27:900-927

Kim J, Hangan H (2007) Numerical simulations of impinging jets with application to downbursts. J Wind Eng Ind Aerodyn 95:279-298

Kim J, Hangan H, Ho TCE (2007) Downburst versus boundary layer induced wind loads for tall buildings. Wind Struct 10:481-494

Lundgren TS, Yao J, Mansour NN (1992) Microburst modelling and scaling. J Fluid Mech 239:461-488

Mara TG, Hong HP, Lee CS, Ho TCE (2016) Capacity of a transmission tower under downburst wind loading. Wind Struct 22:65-87

Mason MS, Wood GS, Fletcher DF (2009) Numerical simulation of downburst winds. J Wind Eng Ind Aerodyn 97:523-539

Mason MS, Fletcher DF, Wood GS (2010) Numerical simulation of idealised three-dimensional downburst wind fields. Eng Struct 32:3558-3570

McCarthy J, Wilson JW, Fujita TT (1982) The joint airport weather studies project. Bull Amer Meteor Soc 63:15-22

McConville AC, Sterling M, Baker CJ (2009) The physical simulation of thunderstorm downbursts using an impinging jet. Wind Struct 12:133-149

Oreskovic C (2016) Numerical investigation of full scale thunderstorm downbursts: a parametric study and comparison to meteorological model. MESc dissertation, University of Western Ontario

Orf LG, Anderson JR, Straka JM (1996) A three-dimensional numerical analysis of colliding microburst outflow dynamics. J Atmos Sci 53:2490-2511

Orf LG, Anderson JR (1998) A numerical study of traveling microbursts. Mon Wea Rev 127:1244-1258

Orf LG, Kantor E, Savory E (2012) Simulation of a downburst-producing thunderstorm using a very high-resolution three-dimensional cloud model. J Wind Eng Ind Aerodyn 104-106:547-557

Orf LG, Oreskovic C, Savory E, Kantor E (2014) Circumferential analysis of a simulated three-dimensional downburst-producing thunderstorm outflow. J Wind Eng Ind Aerodyn 135:182-190

Roberto M, Oreskovic C, Porto J, Savory E (2014) Unsteady RANS modelling of density driven experimental thunderstorm downbursts. In: 25th Canadian Congress of Applied Mechanics, London, Canada, 4 June

Rumble JR (ed) (2017) CRC handbook of chemistry and physics, 98th edn. CRC press, Boca Raton, USA

Sengupta A, Sarkar PP (2008) Experimental measurement and numerical simulation of an impinging jet with application to thunderstorm microburst winds. J Wind Eng Ind Aerodyn 96: 345-365

Vermeire BC, Orf LG, Savory E (2011a) Improved modelling of downburst outflows for wind engineering applications using a cooling source approach. J Wind Eng Ind Aerodyn 99:801-814

Vermeire BC, Orf LG, Savory E (2011b) A parametric study of downburst line near-surface outflows. J Wind Eng Ind Aerodyn 99:226-238

Yao J (1994) Experiments on microbursts. PhD Dissertation, University of Minnesota

Yao J, Lundgren TS (1996) Experimental investigation of microbursts. Exp Fluids 21:17-25

Zhang Y, Hu H, Sarkar PP (2013) Modeling of microburst outflows using impinging jet and cooling source approaches and their comparison. Eng Struct 56: 779-793

Chapter 3

3 Experimental Simulation of Traveling Downbursts Using the Two-Fluid Model

In this experimental research study, thunderstorm downbursts are simulated in the laboratory using the two-fluid model. In the previous chapter, the focus was on the design and testing of a new release mechanism to be used in the density-driven downburst simulations. In this study, the experimental setup was re-designed to implement the conditions of storm translation and sheared environment in which the downburst occurs. In the following sections, a review of the related literature, details of the experimental apparatus, measurement techniques and the results of downburst simulations in the new setup are presented, respectively.

3.1 Introduction

Thunderstorm downbursts are short-lived extreme weather events characterized by a descending mass of cold and dense air that originates from a thunderstorm cloud base (Fujita 1985). Heat loss due to microphysical processes occurring within the cloud and leading to the creation of a negatively buoyant mass is considered to play the main role in the initiation of such downdrafts. In some cases, the drag force associated with the accompanying precipitation also contributes to the downward movement of the colder air volume (Orf et al. 2012). Upon impinging the ground, the air parcel radially spreads away from the impact point and causes high intensity winds in the near ground region. The suddenly changed vertical and horizontal wind fields pose a substantial threat to aviation and also to trees, powerlines and other surface structures (Shehata et al. 2005; Elawady and El Damatty 2016). Based on the extent of the affected area, downbursts can be divided into two groups: microbursts (< 4 km extent) and macrobursts (> 4 km extent). Depending on their precipitation content, they can be further described as dry or wet (> 0.25 mm of precipitation at the ground level) downbursts (Alahyari 1995).

Some fundamental information about these meteorological phenomena (including morphology, size, duration and the resultant wind velocities) were collected by observations and direct measurements during real downbursts; the Northern Illinois Meteorological Research on Downbursts (NIMROD) and the Joint Airport Weather Studies (JAWS) are two

of the most important projects in this regard (Fujita 1986; Eilts and Doviak 1987; Hjelmfelt 1987). But the unpredictable nature of downbursts, their short duration and the high costs and difficulty of conducting field investigations make it almost impossible to study every aspect of these events by direct field measurements (Alahyari and Longmire 1994). Numerical simulations have also helped in further understanding of downburst flow fields although the assumptions for initial and boundary conditions have a noticeable impact on the results, making it difficult to interpret the actual dynamics of the downburst outflows (Orf et al. 1996; Mason et al. 2009; Vermeire et al. 2011; Zhang et al. 2013). There have also been several research attempts to experimentally simulate downbursts in the laboratory; such experimental approaches are of great importance for both validating the numerical simulations and providing reliable information for the behaviour of downbursts in the near ground region.

The experimental simulations of downbursts have been conducted based on either the impinging jet model (Chay and Letchford 2002; Letchford and Chay 2002; Mason et al. 2005) or the two-fluid model (Lundgren et al. 1992; Yao 1994; Alahyari and Longmire 1994; Alahyari 1995; Yao and Lundgren 1996). In the latter method, density difference, as the real driving force of the event, was used for the simulation purposes (Lundgren et al. 1992), while the former approach replaces the negative buoyancy with a forced momentum source to resemble the downward motion of one fluid through another (Sengupta and Sarkar 2008). There can be a strong argument that employing the actual cause for the acceleration of a downburst toward the ground is a major factor in performing representative experimental investigations; thus, the two-fluid model can be considered as a more appropriate option. It should be noted that downbursts are complicated meteorological phenomena and their experimental simulation conditions cannot fully represent the natural event, the two-fluid model, despite its limitations (as discussed in Chapter 2 (part 2.2.1)), presents a more realistic approach for the experimental downburst studies. In this method, a small volume of dense liquid is released into a less dense ambient liquid (Alahyari 1995). In Chapter 2, the design of two novel dense fluid release mechanisms and their primary testing were discussed in detail. Moreover, the Lundgren et al. (1992) scaling parameters for relating the size of a laboratory scale simulation to the real downbursts were thoroughly explained and examined for the new experimental setup.

The purpose of the work reported in Chapter 2 was to address the shortcomings of other two-fluid experimental simulations by re-designing the dense fluid release mechanism and making it more representative of the real conditions of the cold air downfall. In the current study, the whole experimental setup was re-designed to implement other important features of actual downbursts. A significant portion of the downbursts observed during the NIMROD and JAWS projects demonstrated asymmetric intensive directional flows which were clearly distinguishable from the more symmetric ones (Hjelmfelt 1987; Holmes and Oliver 2000). This behaviour was attributed to the thunderstorm translation and the sheared environment in which the downburst occurs. Such events were referred to as traveling downbursts and they exhibited a displaced flow field with stronger radial winds in the direction of environmental shear and weaker winds in the opposite direction. This important aspect of downbursts has been widely neglected in the literature concerning both numerical and experimental simulations. Hjelmfelt (1987) separately analyzed the influence of storm translation and environmental wind field on the patterns of NIMROD and JAWS downbursts and concluded that the strong directional divergences in the traveling downbursts were mostly a result of high speed low level environmental flows. In other words, the role of sub-cloud environmental flows in the creation of asymmetric downbursts is more important than the effect of thunderstorm cloud translation. Orf and Anderson (1998) performed numerical modelling, using the cooling source technique, in simplified sheared environments with velocity decaying linearly in the vertical direction. Their results illustrated a clear difference between the flow field of static and traveling downbursts. On the experimental side, Letchford and Chay (2002) used an impinging jet to incorporate the storm translation condition and evaluated the effect of jet movement on the pressure distribution on a cube. In addition to the disadvantages of an impinging jet compared to the two-fluid model, their study also did not use an environmental shear and only translated the jet apparatus on a rail inside a wind tunnel.

Implementation of all these conditions (storm translation and sub-cloud environmental shear) in the laboratory imposes additional challenges and expense (Mason et al. 2009). The current study, for the first time, takes a comprehensive approach to experimentally investigate traveling downbursts in a sheared environmental flow using the two-fluid model. In this regard, a hydraulic flume equipped with a trolley was utilized to incorporate the above-mentioned conditions. Different thunderstorm speeds were examined and the resultant flow fields and

affected areas were quantitatively measured and compared to those of a static downburst. The primary characterization of the ambient flow velocity in the hydraulic flume was conducted by using a hot film anemometer (HFA), and the planar laser-induced fluorescence (PLIF) technique was employed to visualize the simulated downbursts and measure their scalar fields.

3.2   Experimental details

This section is focused on the detailed explanations of fluid properties, components of the new experimental setup, measurement techniques (HFA and PLIF), and experimental procedure, respectively.

3.2.1   Solutions used in the two-fluid model

The fundamentals and assumptions of the experimental simulation of downbursts based on the two-fluid model were discussed in Chapter 2. By application of the Boussinesq approximation, liquids were used instead of gases to create the desired density difference in the domain (Lundgren et al. 1992; Yao and Lundgren 1996). Table 3.1 summarizes the properties of the aqueous solutions of glycerol ($C_3H_8O_3$) and potassium dihydrogen phosphate (KH_2PO_4) which were, respectively, used as the less and more dense fluids.

Table 3.1: Characteristics of solutions used in the experiments (Rumble 2017)

	Ambient fluid ($C_3H_8O_3$ solution)	Downburst fluid (KH_2PO_4 solution)
Concentration: w (% by mass)	7	7
Density: ρ (kg/m^3)	1014.4	1048.6
Dynamic viscosity: η (mPa s)	1.207	1.160
Refractive index: n	1.3412	1.3411
$\Delta\rho/\rho_a$ (%)	3.37	
$\Delta\eta/\eta_a$ (%)	3.89	
Δn	0.0001	

Various solutions were analyzed by Alahyari (1995) and the above-mentioned pair was selected mainly based on the proximity of their refractive indices and their close viscosities. Matching the refractive indices of the two fluids is very important in the proper application of optical measurement methods to avoid the bending of the scattered light as it passes through

different regions within the domain; the difference between viscosities also need to be very small to reflect the real atmospheric conditions (Alahyari and Longmire 1994).

3.2.2 Experimental apparatus

As discussed in the introduction, the key contribution of the current study is to implement the storm translation and environmental flow conditions in the laboratory. In Chapter 2, the two designs of release cylinders (Cylinder 1 and Cylinder 2) were described and their performances were compared. Both of those mechanisms were demonstrated to be capable of producing symmetric and repeatable outflows in the quiescent ambient fluid inside a tank. This was achieved by replacing the retaining membrane at the bottom of cylinder, used in earlier studies (Alahyari 1995; Yao and Lundgren 1996), with iris gates that always operate in the same way. The only difference between the two cylinders is their wall design which in one case consists of 12 slots and, by partial elimination of the solid wall, helps in approaching the real conditions where there is no boundary separating the two fluids. The inclusion of these wall openings was shown to have a significant influence on the dynamics of the resultant flow fields. Thus, in this study, the preferred release mechanism (Cylinder 2) was utilized for the simulations of traveling downbursts. In this regard, the tank containing ambient fluid was substituted by a hydraulic flume. In Figure 3.1(a)-(b), the schematic of the new experimental facility is presented.

A: Storage tank
B: Pump
C: Electromagnetic flow meter
D: Piping system
E: Inlet chamber
F: Flow straightener
G: Trolley system
H: Weir gate
I: Outlet
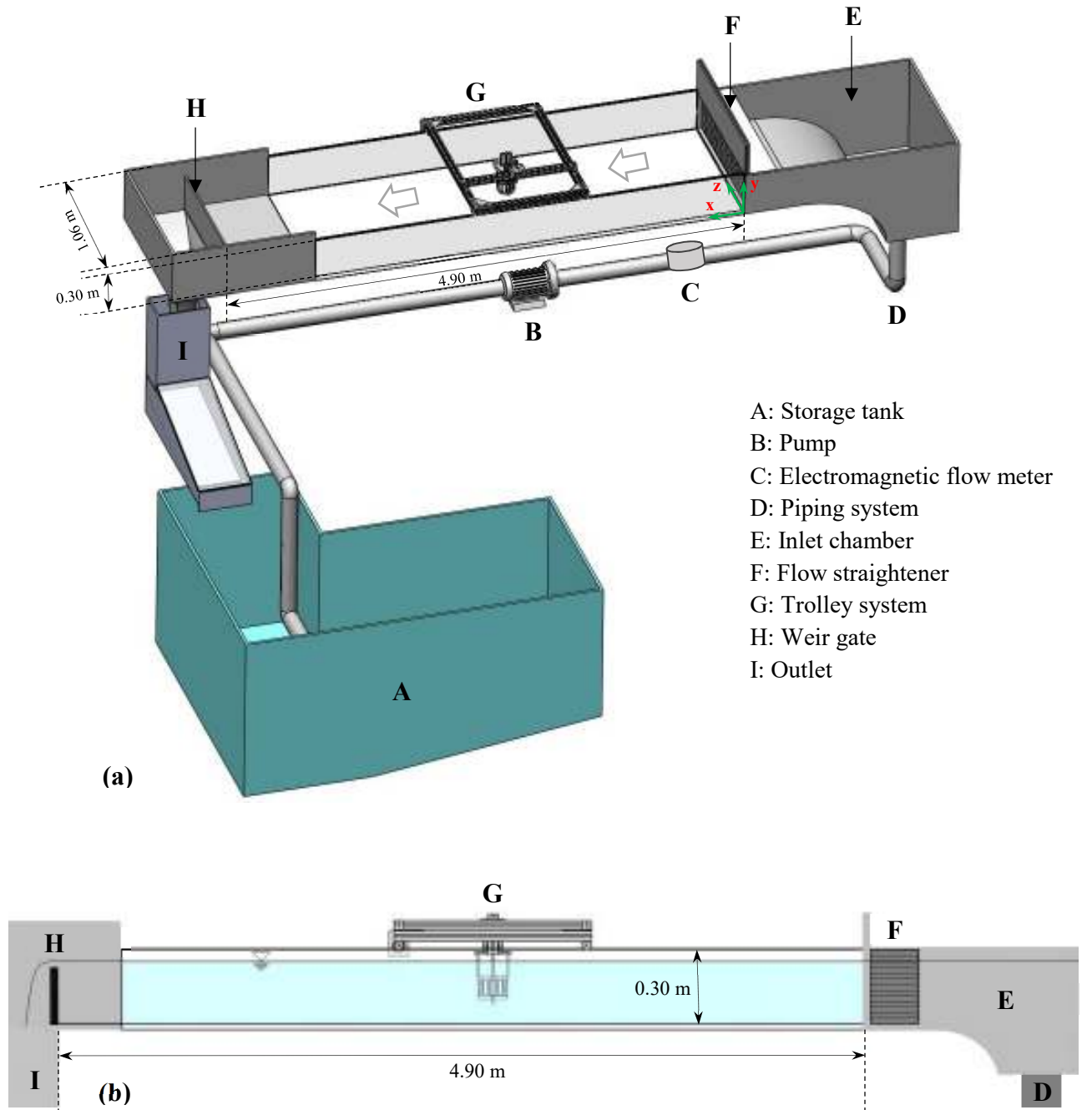
Figure 3.1: Schematic diagram of the experimental apparatus: (a) 3-D view, (b) 2-D view

In the following sections, various components of this setup are described.

3.2.2.1 Hydraulic flume

The working section of this hydraulic flume is of rectangular shape with length, width and depth of 4.90 m, 1.06 m and 0.30 m, respectively (side and bottom walls are built of 1.8 cm

thick regular tempered glass and the top is open to atmosphere). This channel is part of a flow circuit that involves the following sections:

(1) An underground 3 m³ concrete reservoir tank for storing the glycerol solution. The floor and walls of this tank were coated by a pool liner paint and its top was covered using a heavy lid. The underground location helps in keeping the ambient fluid away from the direct exposure to sunlight and other pollution sources, thereby minimizing the potential for algae growth.

(2) An Armstrong pump (4380 series, 1800 RPM) and a piping system (inside diameter = 100 mm) for transferring the ambient fluid from the tank to the inlet chamber of the flume.

(3) Channel inlet section equipped with an aluminum honeycomb flow straightener (with a length of 15 cm and approximate cell size of 0.5 cm) at the downstream end. The geometry of the contraction part of the inlet chamber can be defined using the following elliptic (Equation (3.1)) and cubic (Equation (3.2)) equations and by assuming the upstream end of the contraction as the origin (x, y and z are, respectively, the longitudinal, vertical and horizontal coordinates (in mm)). Using the cubic horizontal profiles helps in avoiding flow separation and sudden pressure drop as the fluid passes through the contraction (Rouse and Hassan 1949). In Figure 3.2(a) and (b), the top and side views of the inlet section are illustrated, the cubic and elliptic curves are shown in red and green colours, respectively. The grey points in Figure 3.2(a) show the inflection positions (x = 415.29 mm) in which the two cubic curves meet, the distance between these points and the upstream end of the contraction is 60% of the total contraction length (L_C = 692.15 mm).

$$y = 352.4\sqrt{1 - \left(\frac{x}{692.15} - 1\right)^2} \tag{3.1}$$

$$z = 1.581 \times 10^{-6} x^3 \qquad 0 \leq x \leq 415.29 \tag{3.2(a)}$$

$$z = 188.8 + 3.558 \times 10^{-6} (x - 692.15)^3 \qquad 415.29 \leq x \leq 692.15 \tag{3.2(b)}$$
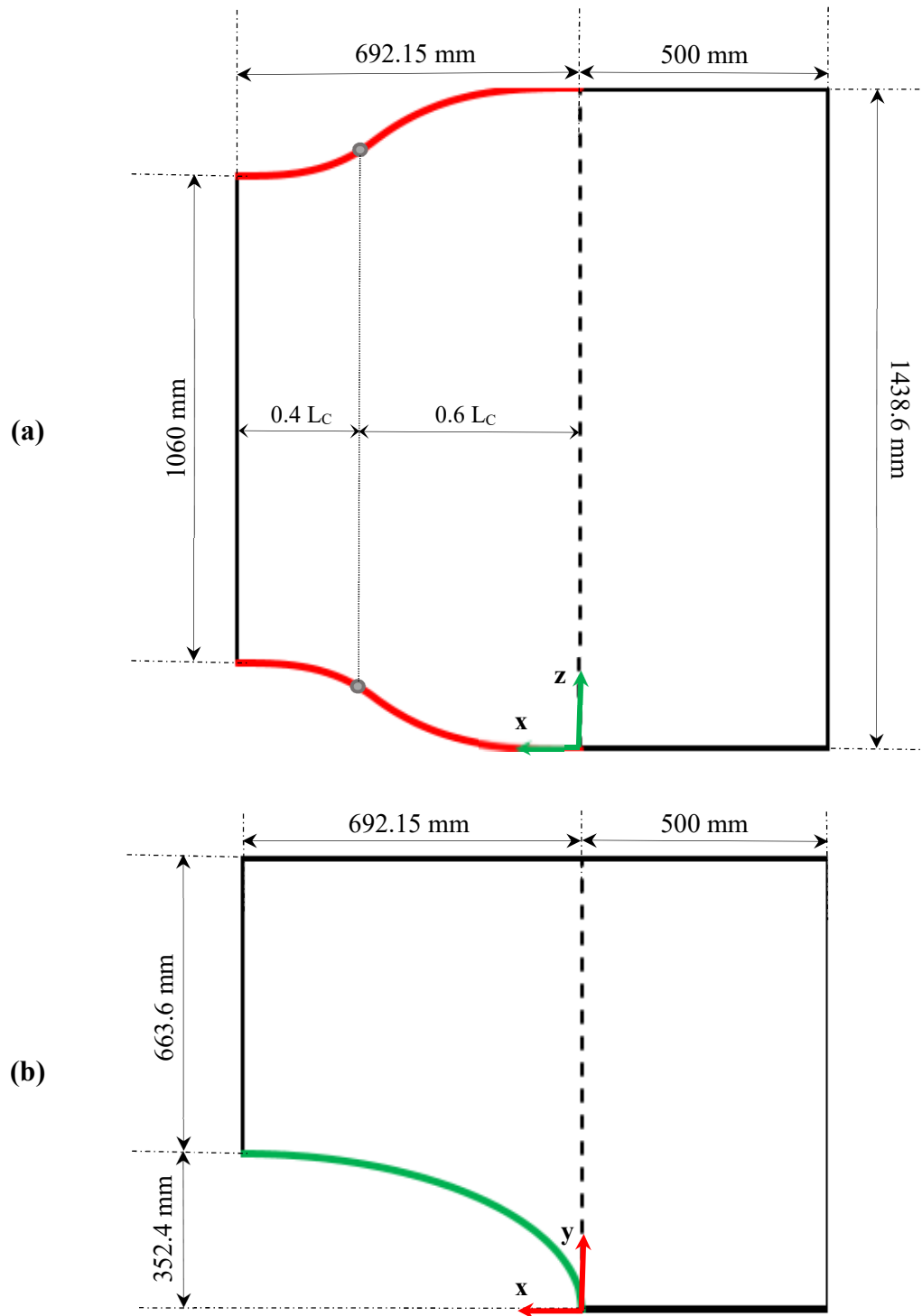
Figure 3.2: Top (a) and side (b) views of the inlet section

(4) The outlet section equipped with a weir gate with the thickness of 1.2 cm, made of a zinc-based alloy, and a return line back to the underground reservoir tank. The depth of the flow in the channel was controlled by adjusting the weir gate height.

All the non-glass parts of the hydraulic channel (the inlet and outlet sections) were laser cut, formed and welded from 304 stainless steel.

3.2.2.2 Trolley system

The flow of glycerol solution in the channel represents the sub-cloud environmental flow. In order to simulate the translation of the thunderstorm cloud in the new experimental setup, a trolley system was designed and manufactured from extruded aluminum tracks. The top view of this system is shown in Figure 3.3(a). The release mechanism containing potassium dihydrogen phosphate solution was securely positioned in a holder apparatus which was attached to the trolley (Figure 3.3(b)). By adjusting the vertical position of the release cylinder in the holder apparatus, the initial downburst release height (distance between the bottom iris and the flume floor) was controlled.

A compact round-face DC gearmotor (161 RPM at 2.64 Nm torque) and four plastic wheels were utilized to translate the trolley system along the flume in the direction of ambient fluid flow. The speed of this translation was controlled through a LabVIEW code (Appendix 1) by inputting different motor duty cycle (D) values; each value leads to a specific trolley speed that can be calculated using the data from a position tracking encoder attached to the trolley. This LabVIEW code can also be used to specify the desired distance at which the release mechanism drops the dense fluid.
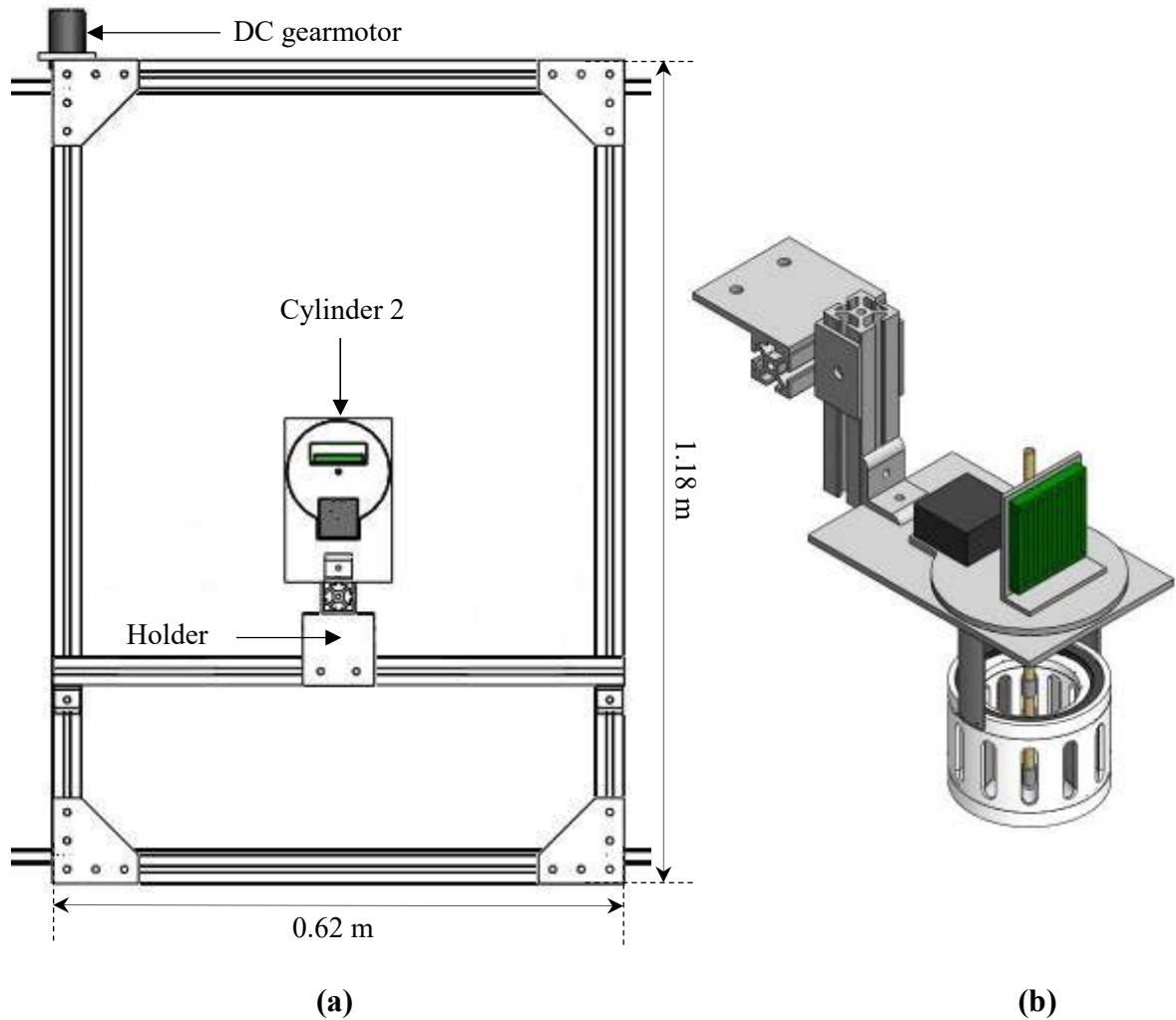
Figure 3.3: (a) Plan view of the trolley system used for traversing the dense fluid release mechanism and (b) release cylinder (Cylinder 2)

3.2.3   Measurement techniques

3.2.3.1   Velocity measurement using a HFA

Before the start of traveling downburst experiments, it was necessary to characterize the velocity field of ambient fluid in the channel for various pump flow rates. In this regard, a single hot film anemometer (HFA) was utilized. This velocity measurement system consists of a Dantec heavy coating straight fiber-film probe (55R11) (Figure 3.4(a)) and a miniature Constant Temperature Anemometer (miniCTA, 54T30) (Figure 3.4(b)). The thin film sensor is of cylindrical shape (70 μm diameter and 1.25 mm long with 2 μm quartz coating) and its axis must be perpendicular to the flow direction.

This sensor is heated to a constant temperature higher than that of ambient fluid and as the glycerol solution passes over it, the film temperature decreases due to forced convection heat transfer (ambient fluid temperature = 20.6 ℃, sensor temperature = 37.0 ℃, overheat ratio = 0.79, sensor resistance = 6 Ω). The temperature drop is compensated by sending a voltage to the probe to return it back to the specified constant value (Bruun 1995). By defining the relationship between flow velocity, heat transfer rate, temperature fall and the required voltage, a calibration scheme can be developed to mathematically express the velocity magnitude in terms of the voltage.

(a)   (b)
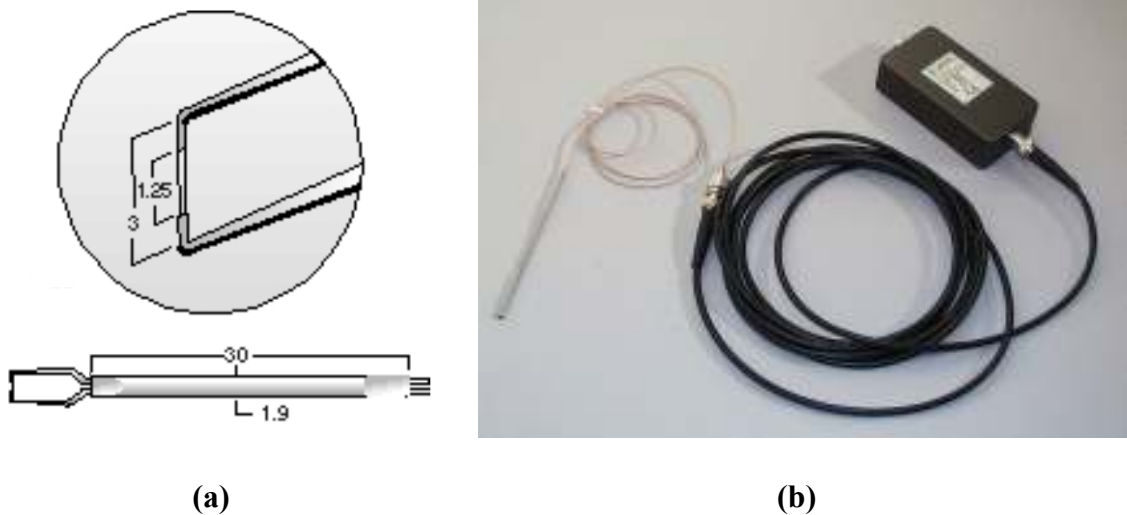
Figure 3.4: (a) Fiber-film probe (dimensions are in mm) and (b) miniCTA system
(www.dantecdynamics.com)

For calibration purposes, a set of known velocities is required. Such values were obtained by attaching the hot film probe to the trolley via a holder system and translating it inside the hydraulic channel while there was no flow (the flume was filled with ambient solution, the weir gate was closed and the pump was turned off). Then, a LabVIEW code was used to record the voltage data, with a frequency of 1000 Hz, for a trolley displacement of 100 cm. By averaging the voltages over this distance, a single value can be associated to each sensor speed, which is equal to the trolley speed.

After obtaining the calibration equation, the hot film probe can be used to measure the velocity at desired positions for different pump flow rates. The longitudinal, horizontal and vertical positions of the probe in the channel can be easily adjusted by moving the trolley along the

flume, changing the probe attachment location across the flume and altering the probe height through its holder system, respectively. In the calibration tests, probe was moving and the fluid was quiescent, but for the actual velocity measurements, the probe was stationary with the flow passing over it and the voltage data was gathered for 60 s.

3.2.3.2 Scalar field characterization by the PLIF technique

Flow fields of the simulated traveling downbursts were visualized using the PLIF technique, Figure 3.5 illustrates the various components of the PLIF system.
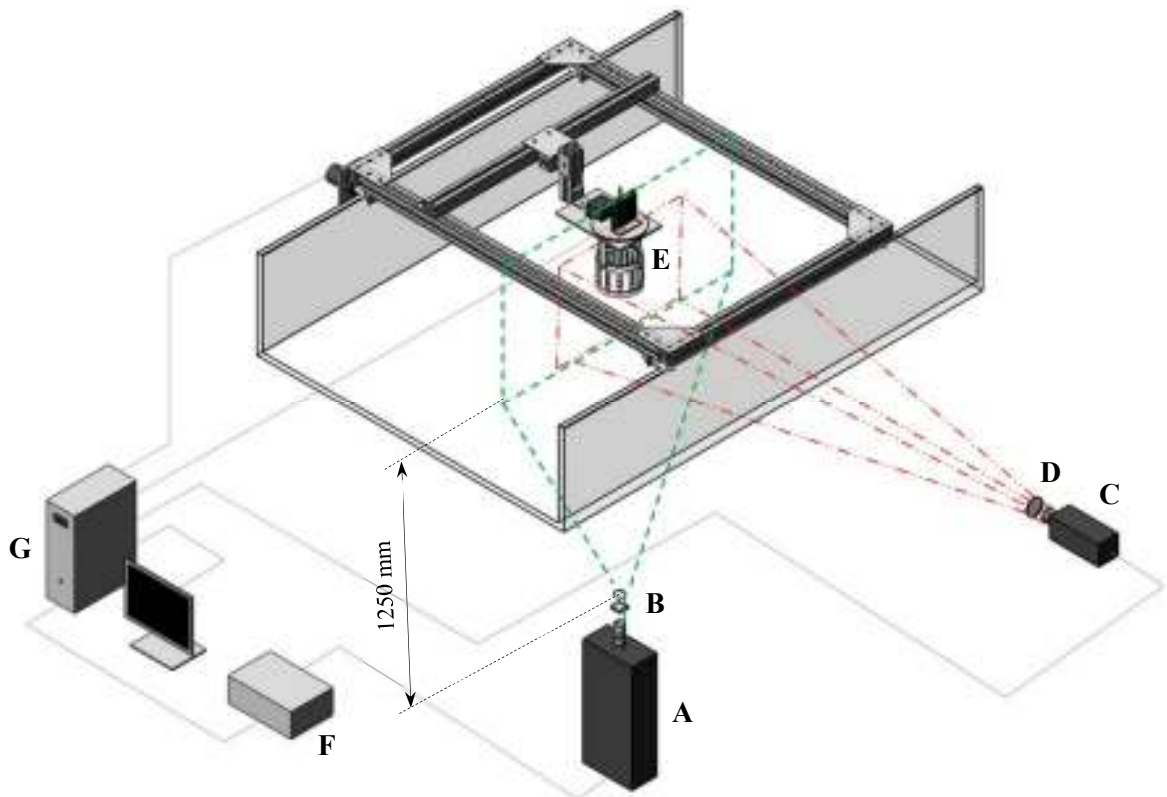
Figure 3.5: PLIF measurement system (A: Laser, B: Laser sheet optics, C: Camera, D: Filter, E: Field of view, F: Synchronizer, G: Computer system)

All details on the principles of the PLIF method, its application in measuring the concentration field and the PLIF calibration procedure were described in Chapter 2. Since in the current setup, the vertical laser sheet passed through the bottom of the channel (Figure 3.5), it was necessary to have a wide enough sheet to cover the entire camera field of view. Thus, a cylindrical lens, with short focal length, was required to expand the laser beam and obtain a

higher divergence angle; in this regard, a combination of cylindrical lenses was employed (Equation (3.3)).

$$\frac{1}{f} = \frac{1}{f_1} + \frac{1}{f_2} \qquad\qquad f = -9.375 \text{ mm} \qquad\qquad (3.3)$$

In this equation, f_1 (= -25 mm) and f_2 (= -15 mm) are the focal lengths of each cylindrical lens and f is the focal length of the combined lenses. In Table 3.2, the important specifications of the PLIF setup, used in the current study, are presented. The thickness of laser sheet and Raleigh length were computed using the equations of Crimaldi (2008).

Table 3.2: PLIF measurement technique specifications

Laser beam wavelength	532 nm
Laser beam diameter	6.3 mm
Laser pulse frequency	10 Hz
Laser pulse energy	100 mJ/pulse
Cylindrical lens focal length	-9.375 mm
Spherical lens focal length	1000 mm
Laser sheet thickness	2.69 mm
Raleigh length	21.3 m
Fluorescence emission wavelength	590 nm
Camera resolution	1.4 MP
Camera filter cut-off frequency	545 nm
Image capturing frequency	10 Hz
Image capturing duration [a]	40 s
Number of images captured	400
Size of camera field of view	L × H = 509.84 mm × 379.41 mm
Captured image resolution	370.5 μm/pixel
Image resolution/R_0	8.38×10^{-8}

[a] Duration of a release test is 8 s in average, but recording was started before the cylinder entered the field of view of the camera and lasted until both ends of the vortex left the field of view.

3.2.4   Experimental procedure

Values of the Lundgren et al. (1992) scaling parameters for the experimental simulations of traveling downbursts are presented in Table 3.3 (definitions of these parameters are given in part 2.2.2 of Chapter 2).

Table 3.3: Scaling parameters for downburst simulations using the two-fluid model

Release cylinder inside diameter: d_i	7.5 cm
Release cylinder inside height: h_i	8.2 cm
Release cylinder volume: Q	362 cm^3
Density difference: $\Delta\rho/\rho_a$ (%)	3.37
Length scale (R_0)	4.42 cm
Time scale (T_0)	0.37 s
Velocity scale (V_0)	12.09 cm/s
Reynolds number (Re)	4565

Table 3.4 provides information on the various features of each release experiment conducted in this study. Before the start of release tests, the velocity field of the hydraulic flume (for each pump flow rate and flow depth) was characterized. Having such velocity profiles can help in understanding the behaviour of traveling downbursts embedded in a sheared ambient environment. Moreover, the vertical velocity profiles were used to adjust the trolley speed in a way that at the time of release, the translational speed of the cylinder equalled the ambient fluid velocity at the release point. Thus, for each test in Table 3.4, a corresponding value of motor duty cycle was specified in the LabVIEW program to achieve the desired speed. The results of Test 1 in each group represented a stationary downburst.

Table 3.4: Experimental settings for different traveling downburst tests

	Group 1			
H_0 (cm)	14.5			
H_0/R_0	3.28			
h (cm)	28			
h_{top} (cm)	5.3			
$A_{cross-section}$ (m²)	0.2968			
	Test 1	**Test 2**	**Test 3**	**Test 4**
Q_{pump} (L/s)	0	9.15	14.70	19.10
$\bar{u}$ [a] (cm/s)	0	3.08	4.95	6.42
	Group 2			
H_0 (cm)	12.5			
H_0/R_0	2.83			
h (cm)	26			
h_{top} (cm)	5.3			
$A_{cross-section}$ (m²)	0.2756			
	Test 1	**Test 2**	**Test 3**	**Test 4**
Q_{pump} (L/s)	0	9.15	14.70	19.10
$\bar{u}$ [a] (cm/s)	0	3.32	5.33	6.91
	Group 3			
H_0 (cm)	10.5			
H_0/R_0	2.38			
h (cm)	24			
h_{top} (cm)	5.3			
$A_{cross-section}$ (m²)	0.2544			
	Test 1	**Test 2**	**Test 3**	**Test 4**
Q_{pump} (L/s)	0	9.15	14.70	19.10
$\bar{u}$ [a] (cm/s)	0	3.60	5.78	7.49

[a] $\bar{u}$ is the average flow velocity and is calculated by dividing the pump flow rate (Q_{pump}) by the cross-sectional area ($A_{cross-section}$ = channel width × h).

The purpose of conducting three groups of traveling downburst simulations was to investigate the influence of initial release height (H_0). This value is a representation of the thunderstorm cloud base height at the time of downburst acceleration toward the ground. By assuming the length sale (R_0) of a typical natural downburst to be around 0.7 km, these three groups of experiments represent the 2.3 km, 2.0 km and 1.7 km cloud base heights, respectively, it should be noted that the value of 0.7 km is the characteristic length of the downburst in Delta Airline Flight 191 accident and is just an instance of the size of natural downbursts (Hjelmfelt 1987; Lundgren et al. 1992; Yao 1994). The average velocity of the channel flow in Table 3.4 varies in the range of 3.08-7.49 cm/s. To relate these values to the average wind velocity in the sub-cloud region of the real traveling downbursts, a scaling rule was used (Equation (3.4)).

$$\left(\frac{\bar{u}}{V_0}\right)_{\text{laboratory scale}} = \left(\frac{\bar{u}}{V_0}\right)_{\text{natural scale}} \tag{3.4}$$

According to this rule, the ratio of average velocity to the velocity scale (V_0) was assumed to be constant at different downburst scales. Thus, by having the scaling parameters in simulated and natural downbursts, the corresponding average environmental wind speeds can be calculated. The results of such scaling are presented in Table 3.5, the calculated magnitudes (3.88-9.41 m/s) are in agreement with the typical low-level wind speeds measured during the NIMROD and JAWS projects (Hjelmfelt 1987) and the values reported in more recent field studies (Pistotnik et al. 2010; Burlando et al. 2017). Orf and Anderson (1998), who numerically modeled the traveling downbursts, also used the range 3-15 m/s in their simulations.

Table 3.5: Application of the velocity scaling to the natural and experimental traveling downbursts

	Downbursts in flume	Downbursts in nature
R_0 (m)	0.0442	700
$\Delta\rho/\rho_a$ (%)	3.37	3.37
T_0 (s)	0.37	46
V_0 (m/s)	0.1209	15.2
$\dfrac{\bar{u}}{V_0}_{\text{minimum}}$	0.255	0.255
$\dfrac{\bar{u}}{V_0}_{\text{maximum}}$	0.619	0.619
$\bar{u}_{\text{minimum}}$ (m/s)	0.0308	3.88
$\bar{u}_{\text{maximum}}$ (m/s)	0.0749	9.41

It should be noted that the experimental setup used in this study is a batch system (Figure 3.1), this means that following each release test, the dense fluid inside the release cylinder gets mixed with the light fluid in the flow circuit. Thus, the value of initial density difference is expected to decrease after each trial, because the density of downburst solution remains constant while the density of ambient fluid increases. In part 2.2.6 of Chapter 2, the preparation process of the dense and light fluids and also the considerations for avoiding the variations of dense fluid density in different release tests were explained. To quantify the influence of mixing on the variations of the density difference ($\Delta\rho/\rho_a$), the time scale (T_0) and velocity scale (V_0) with the number of trials, an equation was developed to calculate the density of glycerol solution before conducting the Nth release experiment (Equation (3.5)).

$$\rho_{a(\text{for Nth trial})} = \frac{\rho_g V_g + \rho_w V_w + (N-1)Q\rho_d}{V_w + V_g + (N-1)Q} \tag{3.5}$$

In this equation, ρ_a, ρ_g, ρ_w and ρ_d are the density of ambient solution, glycerol, water and dense solution, respectively. V_g and V_w represent the volume of glycerol and water used for the preparation of initial glycerol solution (3 m³ solution with concentration of 7% by mass), and Q is the volume of the release cylinder.

By knowing the density of ambient fluid for each release test, the values of $\Delta\rho/\rho_a$, T_0 and V_0 can also be determined. In Figure 3.6, the variations of these parameters with the number of releases are shown for 50 trials.
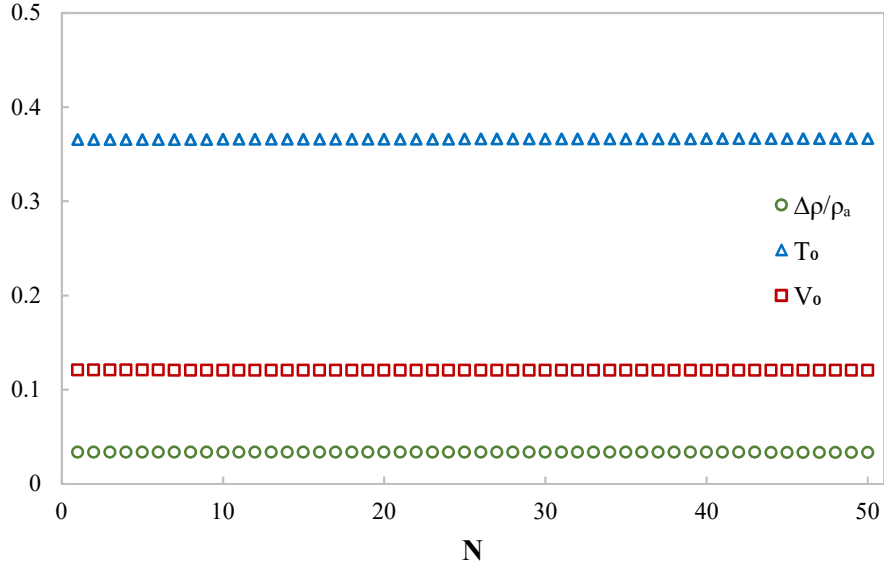
Figure 3.6: Variations of density difference, time scale and velocity scale versus the number of release tests

According to this figure, changes in $\Delta\rho/\rho_a$, T_0 and V_0 are not noticeable, after conducting 50 release experiments, there is a 0.6% decrease in $\Delta\rho/\rho_a$, 0.3% increase in T_0 and 0.3% decrease in V_0. Thus, it can be concluded that because of the small volume of dense fluid (0.362 L) compared to the ambient fluid volume (3000 L), changes in the values of these key parameters are very small and insignificant. It is worth noting that, after each trial, the mixing of dense and ambient fluids results in the increase of fluorescent dye concentration in the flow circuit and enhances the background intensity in PLIF images. To address this issue, before each release experiments, a new set of background images was captured and used for the calibration of raw PLIF pictures of that specific release experiment.

3.3   Results and discussion

3.3.1   flow fields of the stationary downbursts in the flume

The downburst release experiments of the previous chapter were conducted in a relatively small rectangular tank where the length and width of the tank were around 13 and 7 times the

characteristic length of the release mechanism (R_0), respectively. Because the purpose of those experiments was to compare the influence of various factors (the design of release cylinder wall, density difference and initial release height), the wall confinement effect associated with such a small tank was rightfully neglected. The current set of experiments were performed in a hydraulic flume (with the lateral dimension being 24 times R_0), thus the flow fields of stationary downbursts in this channel can be measured and compared to those of downbursts in the tank. Moreover, by having a larger environmental domain in the flume apparatus, the radial propagation of the downbursts can be recorded for a longer period.

The results of three stationary release tests in the hydraulic flume (Test 1 of Groups 1-3) were compared to each other and, as discussed in Chapter 2 (part 2.3.4), similar trends were obtained for the before and after-touchdown phases. As an example of comparison between release experiments in the flume and the tank, Figure 3.7 illustrates the dimensionless flow fields of downbursts in Test 1 of Group 3 and Test 6 of Chapter 2 in the same graphs. The reason for selecting these two specific tests is the closeness between their H_0/R_0 values. It is obvious that other pairs can also be compared as their before and after-touchdown behaviour are not affected by the release height.

(a)

(b)
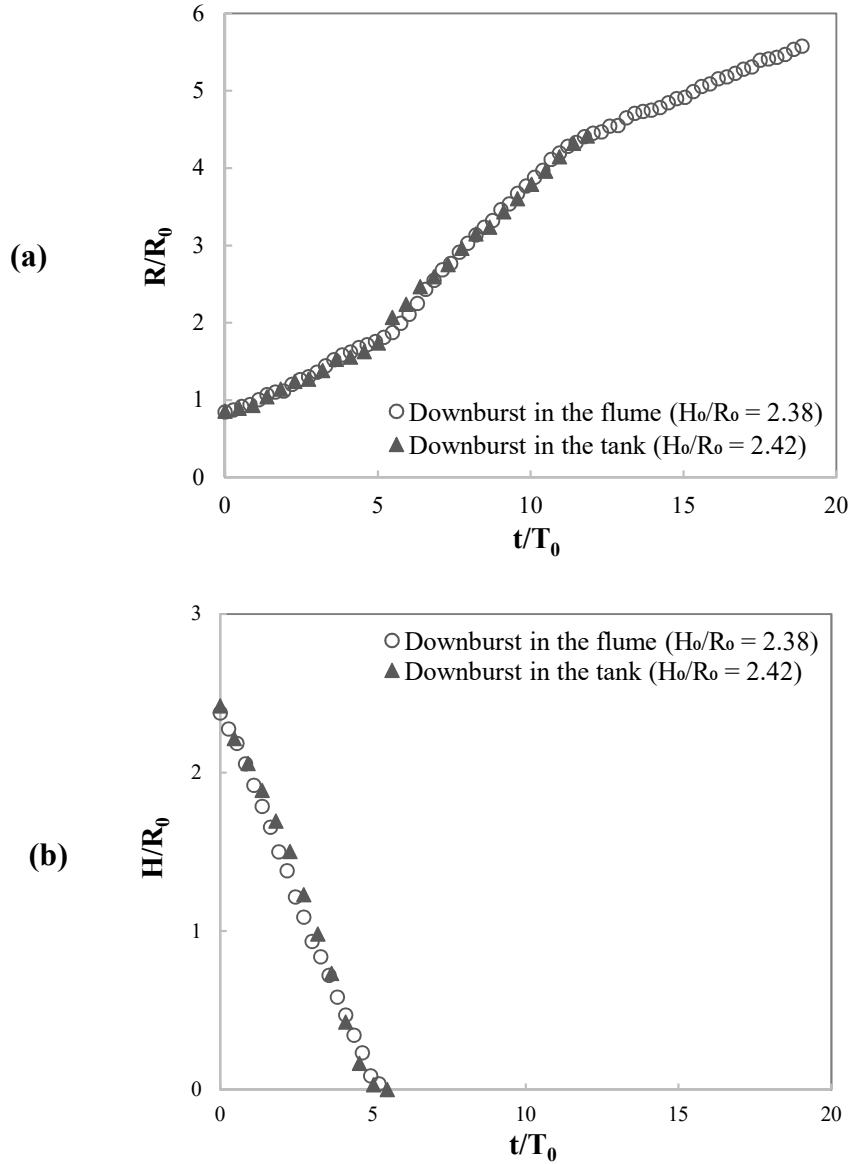
Figure 3.7: Comparing the flow fields of stationary downbursts in the hydraulic flume (Group 3-Test 1) and tank (Chapter 2-Test 6)

In Table 3.6, the characteristics of the resultant outflows of these two release tests are presented. The dimensionless speeds of the radial and vertical fronts ($\frac{1}{V_0}\frac{\overline{dR}}{dt}$ and $\left|\frac{1}{V_0}\frac{\overline{dH}}{dt}\right|$) are defined in Chapter 2 (part 2.3.1). It should be noted that the downburst outflow in the flume experiment was recorded for 6.9 s while for the tank experiment it was only recorded for 4.3 s. Thus, for a better comparison, the after-touchdown radial speeds of the outflow for both release tests were calculated between the touchdown time and 4.3 s.

Table 3.6: Results of the stationary downburst experiments in various setups

	Downburst in the flume	Downburst in the tank	Percentage difference
H_0/R_0	2.38	2.42	-
Ground impact time	$5.47T_0$	$5.47T_0$	-
$\dfrac{1}{V_0}\dfrac{\overline{dR}}{dt}_{BT}$	0.196	0.201	2.5%
$\dfrac{1}{V_0}\dfrac{\overline{dR}}{dt}_{AT}$	0.426	0.372	13.5%
$\left\|\dfrac{1}{V_0}\dfrac{\overline{dH}}{dt}\right\|$	0.473	0.480	1.5%

According to this table, the values of vertical and before-touchdown radial front speeds are similar for the two tests. But for the after-touchdown period, the downburst in the flume propagates with a slightly higher speed which can be attributed to the elimination of the wall confinement.

3.3.2 Comparing the radial flow of a stationary downburst to gravity currents

The life cycle of a thunderstorm downburst shows similarities to the thermals in the phase before ground impingement and to gravity currents in the after-touchdown radial propagation stage (Yao 1994; Alahyari 1995). Experimental simulations of gravity currents have been carried out in several studies; the methodology involved removing a gate behind which the dense fluid rests and allowing it to flow through a lighter ambient environment. Various stages of the development of gravity current flows (slumping, inertial and viscous phases) were first characterized and formulated by Huppert and Simpson (1980) and have been the subject of several numerical and experimental studies since then (Huppert 2006; Cantero et al. 2007; Nogueira et al. 2014; Sher and Woods 2015).

The moment that a downburst impacts on the surface, it can be considered as a gravity current when the holding gate is being lifted. Thus, the outward movement of the downburst fluid, after the touchdown, can be described by mathematical expressions defining gravity currents. According to Huppert and Simpson (1980), the radius of a gravity current during the inertial

phase, where there is a balance between inertial and buoyancy forces, is a function of the square root of time relative to the onset of the inertial phase (Equation (3.6)).

$$\left(\frac{R}{R_0}\right)^2 = \left(\frac{R_1}{R_0}\right)^2 + a\left(\frac{t}{T_0} - \frac{t_1}{T_0}\right) \tag{3.6}$$

In this semi-empirical equation, R_1 and t_1 are the radius and time at the beginning of inertial stage. Before the inertial phase (slumping phase), the radius increases linearly with time and, after the inertial phase, viscous forces become dominant further decreasing the radial speed (Huppert and Simpson 1980; Alahyari 1995; Cantero et al. 2007). Alahyari (1995) and Yao and Lundgren (1996) suggested that the inertial phase of gravity currents corresponds to the behaviour of downburst in the after-touchdown period when the radial propagation strength decreases. In Figure 3.8, the after-touchdown data of the stationary downburst in the flume (Group 3-Test 1) was fitted to the gravity current equation during the inertial stage. In one case, the impact point was considered as the beginning of the inertial phase ((R_1 , t_1) = (1.87R_0 , 5.47T_0)), and in the second case the point at which the radial propagation speed starts to decrease was assumed to be the onset of the inertial stage ((R_1 , t_1) = (4.28R_0 , 11.21T_0)).
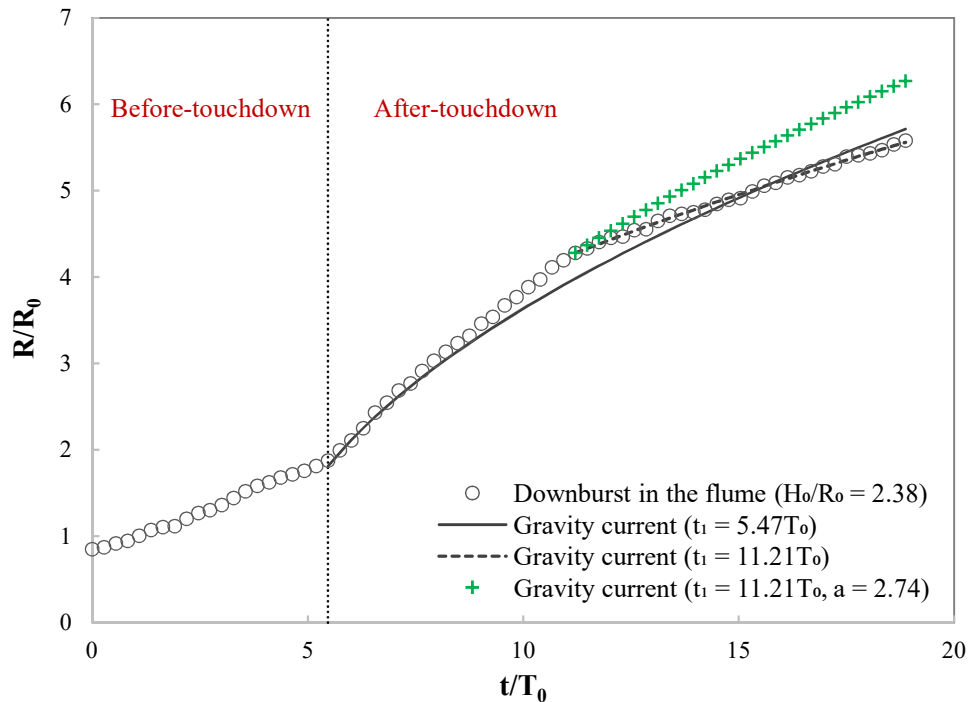

Figure 3.8: Comparison between the radial propagation of a stationary downburst (Test 1 of Group 3) and gravity currents

Table 3.7 presents the details of these two fittings.

Table 3.7: Comparing the downburst flow in Test 1 of Group 3 with gravity currents

Inertial phase onset (R_1, t_1)	Fitted equation	R-squared
$(1.87R_0, 5.47T_0)$	$\left(\dfrac{R}{R_0}\right)^2 = (1.87)^2 + 2.192\left(\dfrac{t}{T_0} - 5.47\right)$	0.973
$(4.28R_0, 11.21T_0)$	$\left(\dfrac{R}{R_0}\right)^2 = (4.28)^2 + 1.645\left(\dfrac{t}{T_0} - 11.21\right)$	0.997

As can be seen in Figure 3.8 and Table 3.7, considering the weakened phase of the after-touchdown period gives a better fit to the gravity current equation in the inertial stage. Thus, it can be said that the first ($t = 5.47T_0$ to $t = 11.21T_0$) and second ($t = 11.21T_0$ to $t = 18.87T_0$) parts of the after-touchdown period, respectively, correspond to the slumping phase (with a constant frontal radial speed) and the inertial phase (with a slower frontal radial speed which decreases with time).

For the rest of stationary downbursts in the flume, the above procedure was repeated and the weakened part of the after-touchdown period was fitted to Equation (3.6). The values of constant a for Test 1 of Group 1 and Test 1 of Group 2 were found to be 1.628 and 1.712, respectively. As pointed out in the previous part, for the stationary downbursts in the flume (Test 1 of Groups 1-3), the after-touchdown radial propagation is independent of the initial release height. Thus, obtaining close values for constant a in these three release experiments (1.628, 1.712 and 1.645 (standard deviation = 0.04)) is reasonable.

It is worth noting that the value of a in Equation (3.6) was 2.74 in the studies of Huppert and Simpson (1980), Alahyari (1995) and Yao and Lundgren (1996) (the green curve with + marker in Figure 3.8 shows the time variations of radial propagation in these studies), but in the current study a lower value (1.645) was obtained. This discrepancy can be related to the difference between release cylinders used in these experiments; as discussed in Chapter 2 (part 2.3.2), the openings in the wall of Cylinder 2 results in a more mixed and less homogeneous dense fluid parcel as it descends. In other words, when the downburst impacts on the ground, its density is lower than that of a downburst from Cylinder 1 (which has solid walls and is similar to that

used by other researchers), and, since the density difference between this fluid mass and its environment is the key to the following radial propagation strength, having a slower radial front speed in the current setup is completely expected.

3.3.3   Velocity measurements in the hydraulic flume using HFA

3.3.3.1   Velocity calibration

In order to find the relationship between the output voltage (E) and the velocity, a set of calibration experiments were conducted. Different values of DC motor duty cycle (D) were specified and the speed of trolley system (and the probe attached to it) was determined using the recorded data from the encoder. Figure 3.9 illustrates the variations of trolley position (x) along the hydraulic channel with time for each duty cycle, data were gathered for 1 m displacement and the probe speed in each case is equal to the slope of the corresponding line.
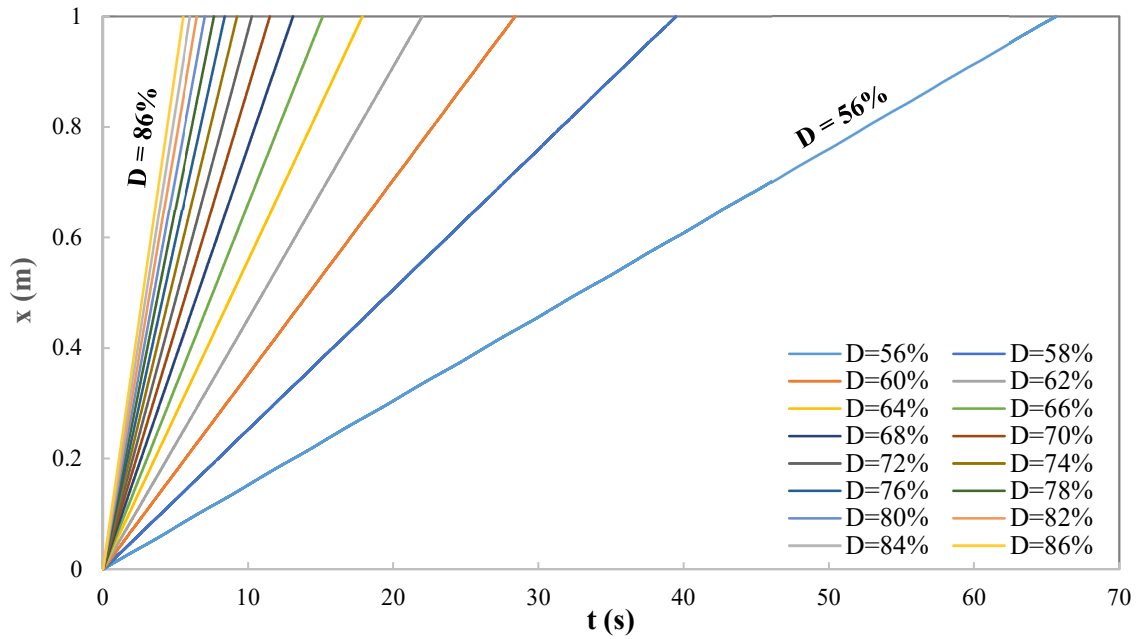

Figure 3.9: Trolley displacement versus time at different values of motor duty cycle

In Figure 3.10(a), the measured speed values at each duty cycle are depicted. On the other hand, in Figure 3.10(b), the average value of recorded voltages during the 1 m trolley displacement are shown for each calibration test. It is obvious that by increasing the motor duty

cycle, the values of both speed and the generated voltage increase. In Equation (3.7), a linear relationship between the velocity and motor duty cycle is presented.

(a)

(b)
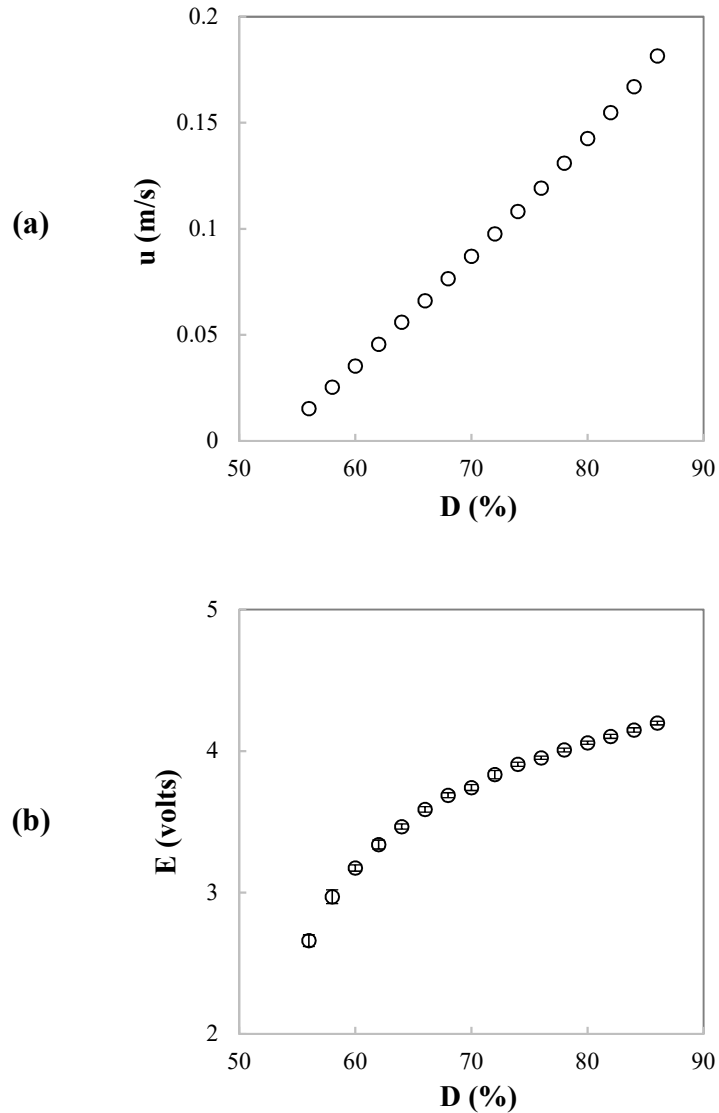
Figure 3.10: Variations of (a) trolley (probe) speed and (b) average hot film output voltage versus motor duty cycle for one set of calibration tests

$$u\left(\frac{m}{s}\right) = 0.0055D\text{-}0.2931 \qquad (R^2 = 0.998) \qquad (3.7)$$

As recommended in the manual of the miniCTA anemometer package, a fourth order polynomial equation (Equation (3.8)) was used to relate the velocity to its corresponding voltage (Equation (3.9)) (Perry 1982; Hultmark and Smits 2010).

$$u = C_0 + C_1E + C_2E^2 + C_3E^3 + C_4E^4 \qquad (3.8)$$

$$u\left(\frac{m}{s}\right) = 3.3958 - 4.3436E + 2.0822E^2 - 0.4446E^3 + 0.0361E^4 \quad (R^2 = 0.999) \quad (3.9)$$

The resultant calibration curve for the data presented in Figure 3.10 is shown in Figure 3.11.
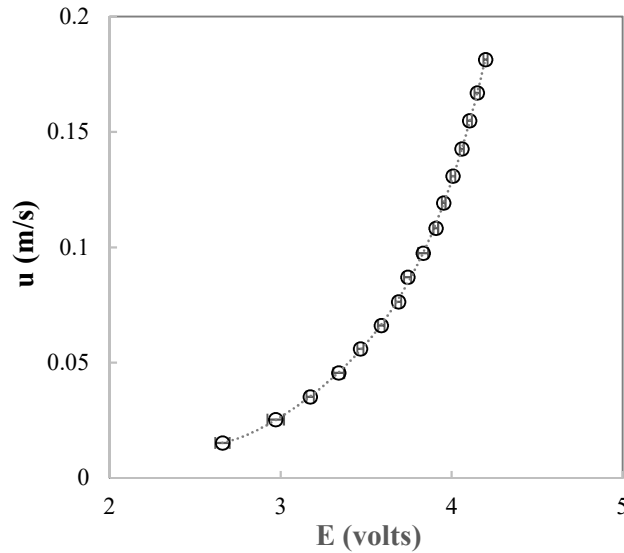
Figure 3.11: An Example of HFA calibration curve

3.3.3.2   Characterization of velocity profiles

For the main velocity measurements at each condition (probe position and pump flow rate), the output voltage was recorded for 60 seconds and, by having the calibration equation, the velocity magnitude was calculated for each voltage value. Then, the average value of these calculated velocities was determined and reported as the mean velocity for that condition. In the following sections, the velocity profiles of the hydraulic flume in different directions are characterized.

3.3.3.2.1   Longitudinal variations of velocity

The purpose of conducting these set of experiments was to both measure the variations of velocity along the flume centreline and to determine a specific distance (x value) after which the velocity remains constant. By having this information, the distance at which the downburst release takes place can be adjusted to avoid the longitudinal variations of ambient fluid velocity

and their possible impact on the resultant flow field. The vertical position of the hot film probe for each group of experiments (see Table 3.4) was determined based on the value of H_0/R_0. In other words, the probe height in each case corresponded to the vertical position of the release cylinder bottom.

As an example, in Figure 3.12, the results of such measurements for Group 1 are presented, the horizontal axis represents the distance from the flume inlet (see the cartesian axes in Figure 3.1(a)), and the values of standard deviation for the measured velocities are illustrated as error bars in the graph.
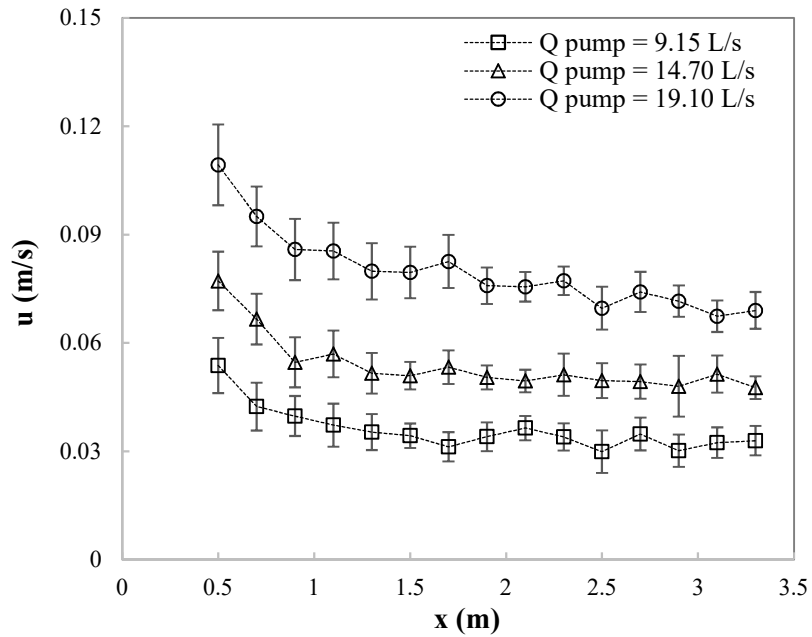
Figure 3.12: Velocity variations along the channel centreline (flow depth = 28 cm, probe height = 14.5 cm)

According to this figure, the velocity of ambient fluid in the centreline of the flume decreases at the beginning until reaching a stable phase at around x = 1.5 m. This initial drop can be attributed to the nonuniformity of the flow in the channel inlet which is directly related to the performance of flow straightener at the downstream end of the contraction in the flume inlet chamber (Figure 3.1(a)). Based on Figure 3.12, it can be said that the downburst release experiments can be done at any distance greater than 1.5 m to avoid the rapid initial velocity changes. Considering the physical structure of the support system attached to the channel floor

and the possibility of performing PLIF measurements, x = 1.9 m was chosen as the best longitudinal position for the release cylinder to drop the heavy fluid.

3.3.3.2.2 Vertical velocity profiles

After determining the appropriate distance at which the dense fluid drops (x = 1.9 m), the centreline vertical velocity profiles were characterized at that distance. In this regard, the hot film probe was positioned at certain heights and the voltage data were recorded. In order to define the boundary layer, more measurements were performed in the lower heights. These measurements were conducted for all the three groups of experiments (Table 3.4) at three different flow rates.

In Table 3.8, the major characteristics of the ambient fluid flow in the hydraulic channel are presented for different pump flow rates in Group 1. In should be noted that the theoretical values of Reynolds number (Re_x) and boundary layer thickness (δ_x) in this table were calculated based on the flat plate boundary layer formulations (Equations (3.10) and (3.11)) (Duncan et al. 1970; White 2016)).

$$Re_x = \frac{Ux}{\nu_a} \tag{3.10}$$

$$\frac{\delta_x}{x} = \frac{5.0}{Re_x^{1/2}} \qquad\qquad 10^3 < Re_x < 10^6 \tag{3.11(a)}$$

$$\frac{\delta_x}{x} = \frac{0.16}{Re_x^{1/7}} \qquad\qquad 10^6 < Re_x \tag{3.11(b)}$$

In Figure 3.13, the experimentally measured velocity profiles are shown for the Tests 2, 3 and 4 of Group 1. The horizontal red dashed line in this figure represents the height of release cylinder bottom (H_0), for each flow rate, the velocity value at this height was determined and used as the cylinder translation velocity (u_t) in the corresponding traveling release experiment. Figure 10(a) and Equation (3.7) were employed to calculate the required motor duty cycle value to achieve this translational velocity.
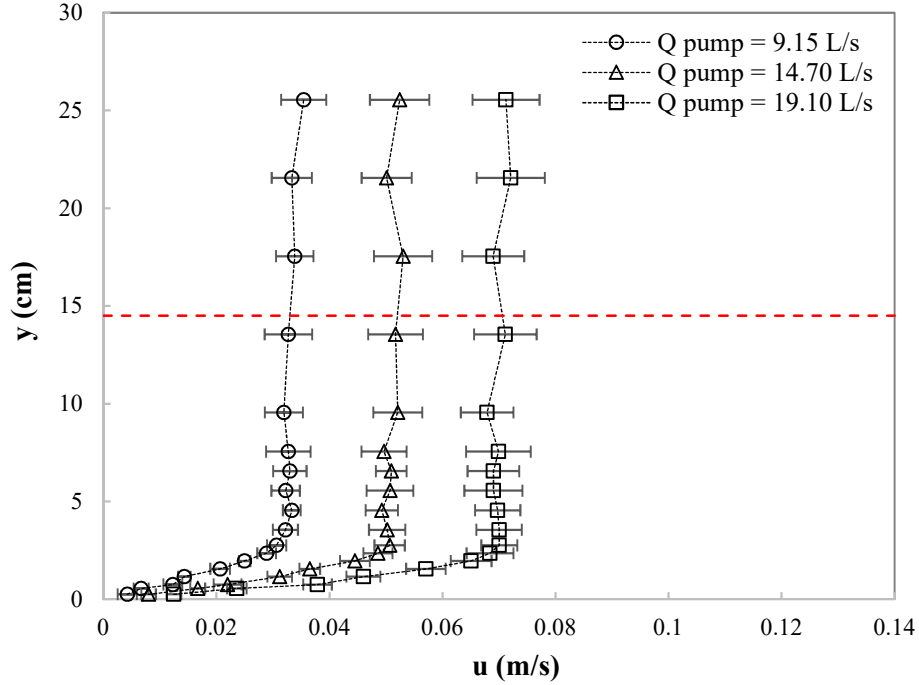
Figure 3.13: Vertical variations of velocity at x = 1.9 m (flow depth = 28 cm, probe height = 14.5 cm)

From this figure, the maximum velocity and boundary layer thickness values can be estimated, the vertical distance at which the difference between two consecutive velocities is less than 5% was assumed to be the thickness of boundary layer. In Table 3.8, these quantities are presented.

Table 3.8: Specifications of the ambient fluid flow at three different flow rates

	Q_{pump} **(L/s)**	9.15	14.70	19.10
	$A_{cross-section}$ **(m^2)**	0.2968	0.2968	0.2968
	$\bar{u}$ **(cm/s)**	3.08	4.95	6.42
	$Re_{x=1.9\ m}$	5.83×10^4	9.37×10^4	1.21×10^5
Theory	$\delta_{x=1.9\ m}$ **(cm)**	3.93	3.10	2.73
	Flow regime	Laminar	Laminar	Laminar
Experiment	$\delta_{x=1.9\ m}$ **(cm)**	3.55	2.75	2.35
	U ^{a} (cm/s)	3.31	5.13	7.00
	Difference between $\delta_{x=1.9\ m}$ values	10.2%	12.0%	15.0%

[a] U is the free stream velocity and was calculated by averaging the measured velocity values outside of the boundary layer.

By comparing the experimental values of this table to the theoretical ones in Table 3.8, a good agreement can be noticed. To further analyze the measured boundary layer data, in Figure 3.14, they were plotted against several established formulae describing the laminar boundary layer (Duncan et al. 1970; White 2016). These formulae are given in Table 3.9 and express the dimensionless velocity in the boundary layer (u/U) in terms of the dimensionless height (y/δ_x), it is obvious that the values of these parameters vary in the range of 0-1.
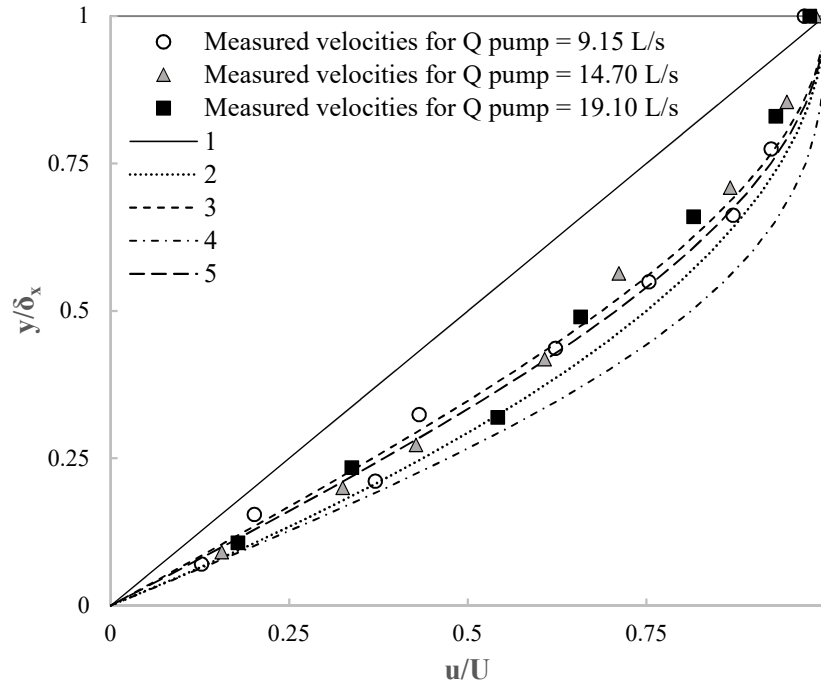
Figure 3.14: Laminar velocity profile in the boundary layer

Table 3.9: Results of fitting the boundary layer data

	Velocity profile formulation	Percentage difference
1	$\dfrac{u}{U} = \dfrac{y}{\delta_x}$	38.1%
2	$\dfrac{u}{U} = 2\left(\dfrac{y}{\delta_x}\right) - \left(\dfrac{y}{\delta_x}\right)^2$	7.8%
3	$\dfrac{u}{U} = \dfrac{3}{2}\left(\dfrac{y}{\delta_x}\right) - \dfrac{1}{2}\left(\dfrac{y}{\delta_x}\right)^3$	6.6%
4	$\dfrac{u}{U} = 2\left(\dfrac{y}{\delta_x}\right) - 2\left(\dfrac{y}{\delta_x}\right)^3 + \left(\dfrac{y}{\delta_x}\right)^4$	12.3%
5	$\dfrac{u}{U} = \sin\left(\dfrac{\pi}{2}\dfrac{y}{\delta_x}\right)$	5.6%

84

In this table, the percentage difference for each curve is also given. Based on these error values, it can be said that the sinusoidal function is the best expression for the experimentally measured velocity values in the boundary layer of the hydraulic channel. The values of momentum thickness (θ), thickness displacement (δ^*) and shape factor for this sinusoidal function can be calculated using Equations (3.12)-(3.14) (Duncan et al. 1970).

$$\theta = \int_0^\delta \frac{u}{U}\left(1-\frac{u}{U}\right) dy = \frac{0.654x}{Re_x^{1/2}} \tag{3.12}$$

$$\delta^* = \int_0^\delta \left(1-\frac{u}{U}\right) dy = \frac{1.741x}{Re_x^{1/2}} \tag{3.13}$$

$$\text{Shape factor} = \frac{\delta^*}{\theta} \tag{3.14}$$

In table 3.10, these theoretical values are compared with the experimentally calculated quantities (numerical integration was used to compute θ and δ^* for the experimental velocity profiles.). Agreement between theory and experiments is evident from this table.

Table 3.10: Laminar flow boundary layer properties

	Q_{pump} (L/s)	9.15	14.70	19.10
Theory	θ (cm)	0.515	0.406	0.357
	δ^* (cm)	1.370	1.081	0.951
	Shape factor	2.66	2.66	2.66
Experiment	θ (cm)	0.505	0.411	0.351
	δ^* (cm)	1.339	1.047	0.896
	Shape factor	2.65	2.55	2.55
	Difference between θ values	1.9%	1.2%	1.9%
	Difference between δ^* values	2.3%	3.1%	6.0%
	Difference between shape factors	0.4%	4.3%	4.1%

3.3.3.2.3 Velocity variations across the flume

In Figure 3.15, variations of velocity in the lateral direction of the channel are shown for the three different pump flowrates in Group 1 (theses velocity values were measured at $y = H_0 = 14.5$ cm and $x = 1.9$ cm.).
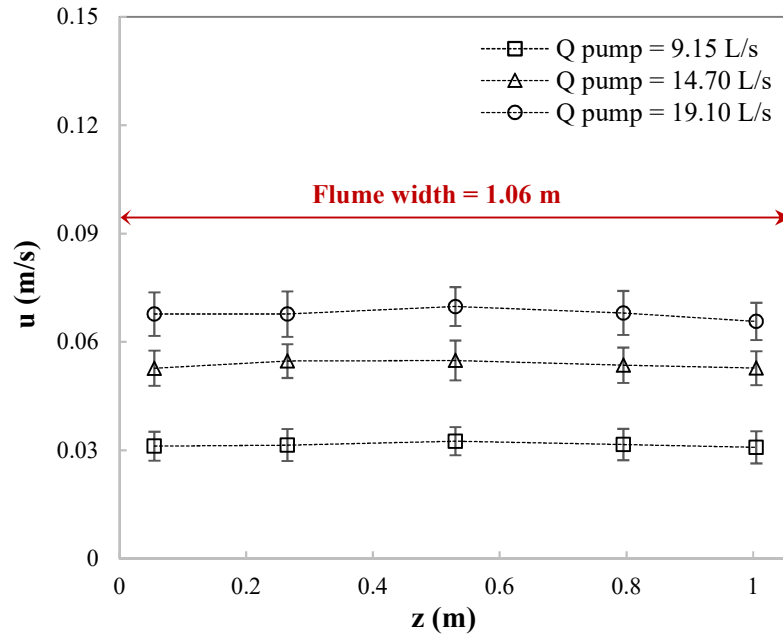

Figure 3.15: Velocity variations across the channel (flow depth = 28 cm, probe height = 14.5 cm)

3.3.4 Evolution of traveling downbursts

By having the velocity profiles of the ambient fluid flow in the hydraulic channel, proper settings can be determined for each traveling downburst experiment. In this regard, as discussed in the experimental procedure (part 3.2.4), specific values of motor duty cycle and release distance were assigned for each pump flow rate used. Figure 3.16 schematically shows the position of the release cylinder within the field of view for the stationary and traveling experiments when the dense fluid drops into the ambient environment. In the stationary tests (Test 1 of Groups 1-3), the release cylinder was placed in the middle of the field of view. By increasing the ambient flow velocity, the release location (the distance at which the iris gates open) was shifted to the right side of the field of view to make it possible to record the

downburst evolution in an environment with a non-zero background velocity for as long as possible.

In Figures 3.17-3.20, the visual development of downburst outflows in Group 1 is illustrated using the calibrated PLIF images, the white line in the bottom of each image represents the channel floor. In these figures, the first, second, third and fourth images were, respectively, captured at 0.3 s, 0.9 s, 2.8 s and 3.8 s following the opening of the release mechanism; for a typical natural downburst (see part 3.2.4), these times, respectively, correspond to 0.6, 1.9, 5.8 and 7.9 min after the acceleration of downdraft toward the ground. The influence of environmental flow on the displacement of the descending dense fluid can be clearly seen in these pictures as the unidirectional flow in the flume (from right to left) intensifies the horizontal propagation of the downburst on one side and weakens it on the opposite side, resulting in an asymmetric flow field.
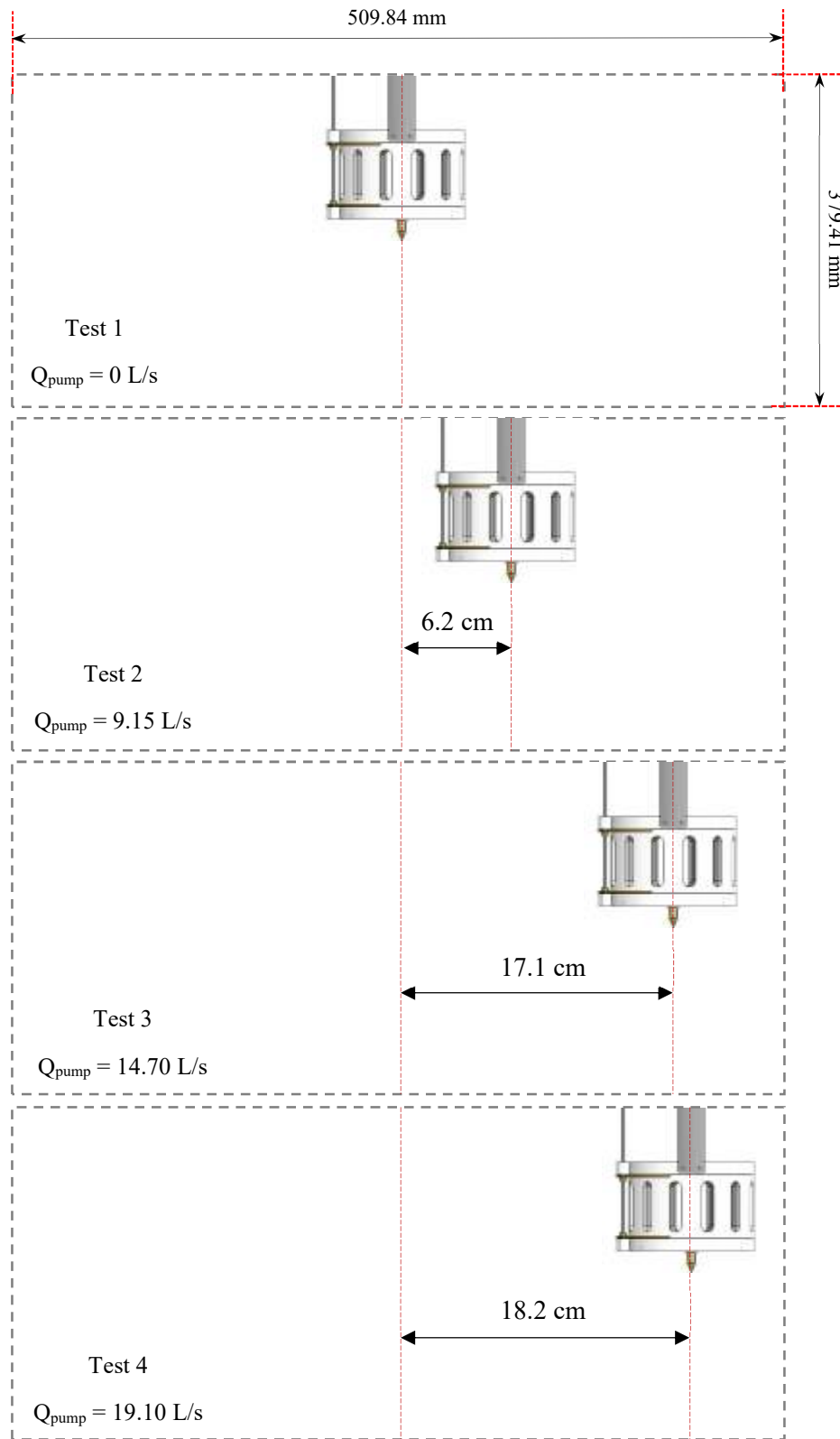
Figure 3.16: Position of Cylinder 2 within the field of view of the camera at the time of release for Tests 1-4

509.84 mm

379.41 mm

t = 0.3 (0.82 T_0) s

t = 0.9 (2.46 T_0) s

t = 2.8 (7.66 T_0) s

t = 3.8 (10.39 T_0) s

$C_{relative} = 0$ $C_{relative} = 1$
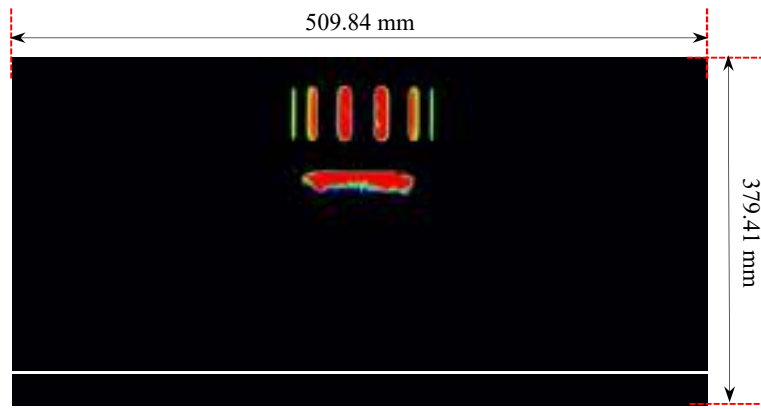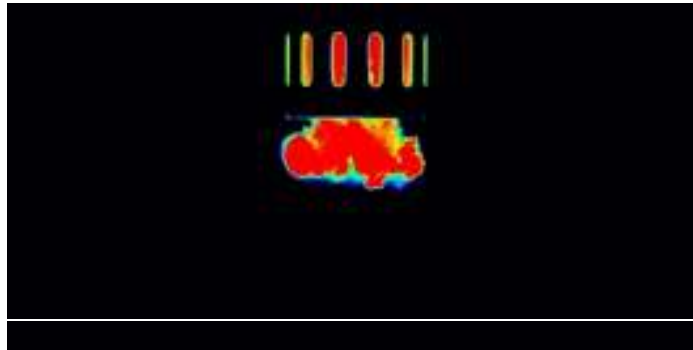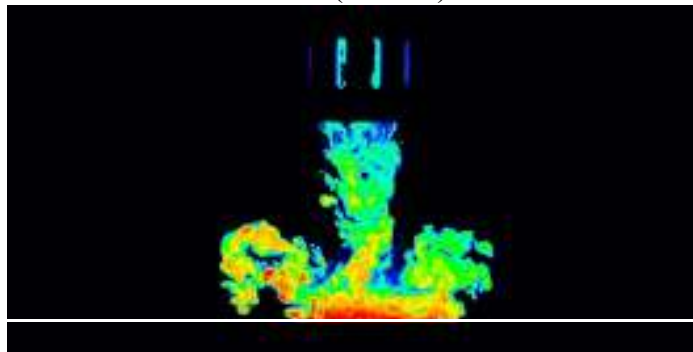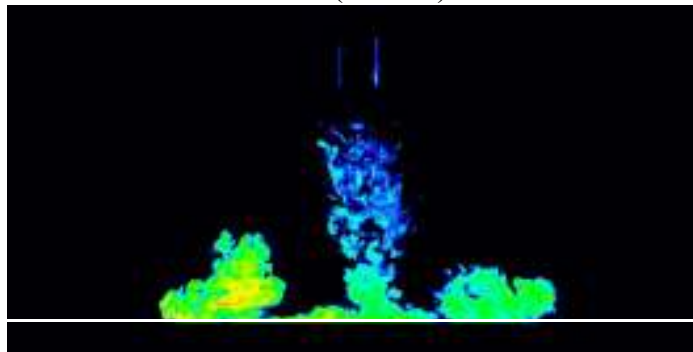
Figure 3.17: Time series of the calibrated PLIF images captured during Test 1 of Group 1 ($Q_{pump} = 0$ L/s, $u_t/V_0 = 0$ cm/s)

509.84 mm

379.41 mm

t = 0.3 (0.82 T_0) s

t = 0.9 (2.46 T_0) s

t = 2.8 (7.66 T_0) s

t = 3.8 (10.39 T_0) s

$C_{relative} = 0$ $C_{relative} = 1$
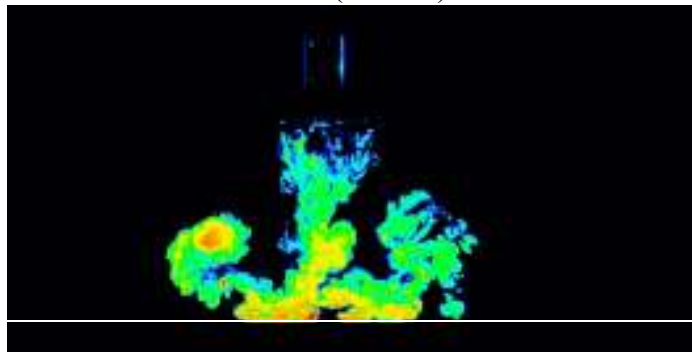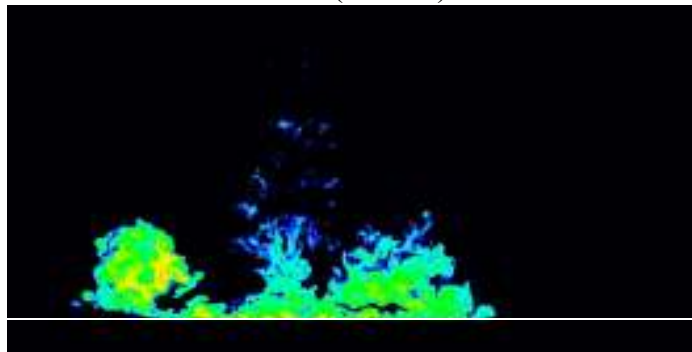
Figure 3.18: Time series of the calibrated PLIF images captured during Test 2 of Group 1 (Q_{pump} = 9.15 L/s, u_t/V_0 = 0.274)

90

509.84 mm

379.41 mm

t = 0.3 (0.82 T_0) s

t = 0. 9 (2.46 T_0) s

t = 2.8 (7.66 T_0) s

t = 3.8 (10.39 T_0) s

$C_{relative} = 0$ $C_{relative} = 1$
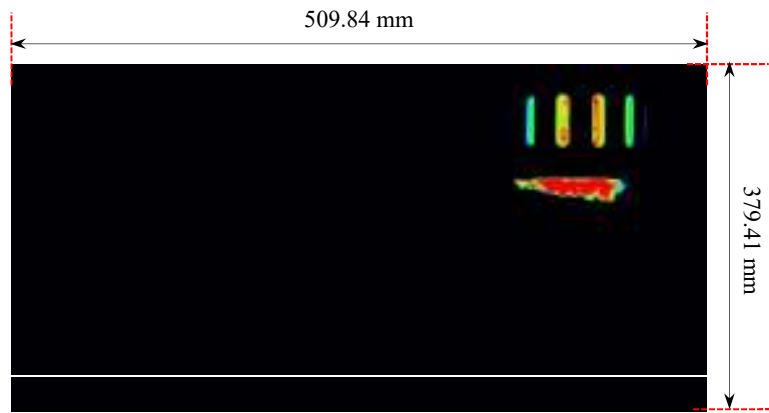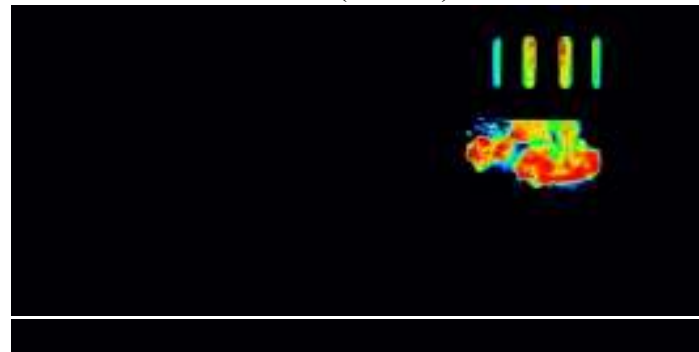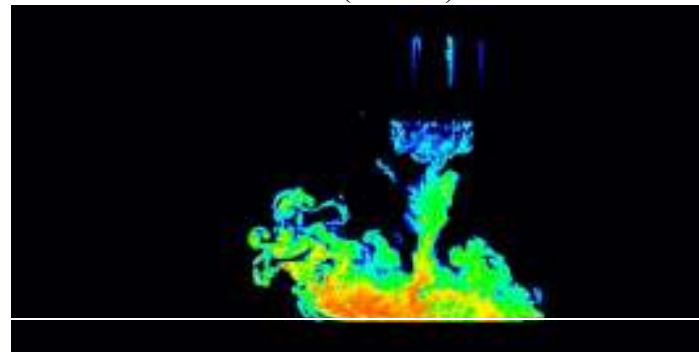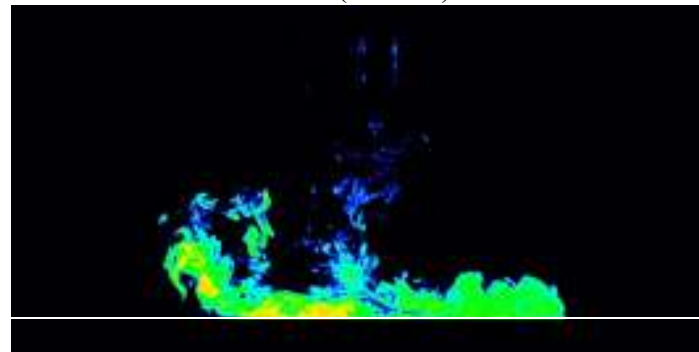
Figure 3.19: Time series of the calibrated PLIF images captured during Test 3 of Group 1 (Q_{pump} = 14.70 L/s, u_t/V_0 = 0.423)

509.84 mm

379.41 mm

t = 0.3 (0.82 T_0) s

t = 0.9 (2.46 T_0) s

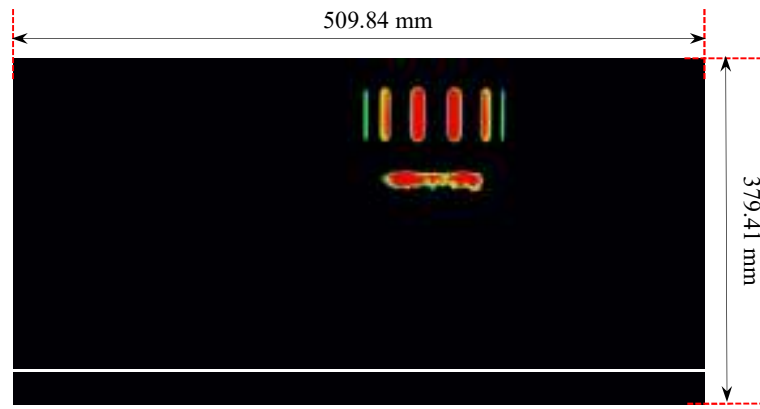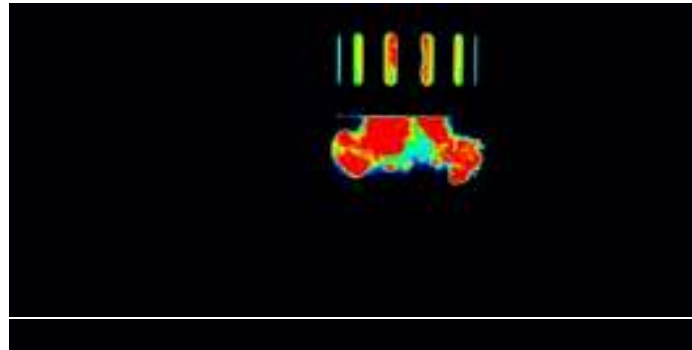t = 2.8 (7.66 T_0) s

t = 3.8 (10.39 T_0) s

$C_{relative} = 0$

$C_{relative} = 1$
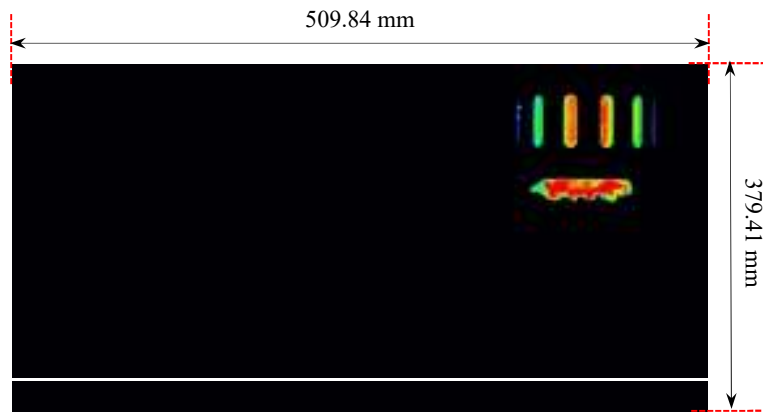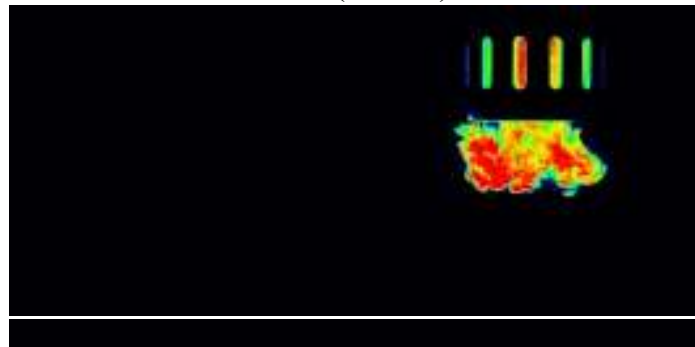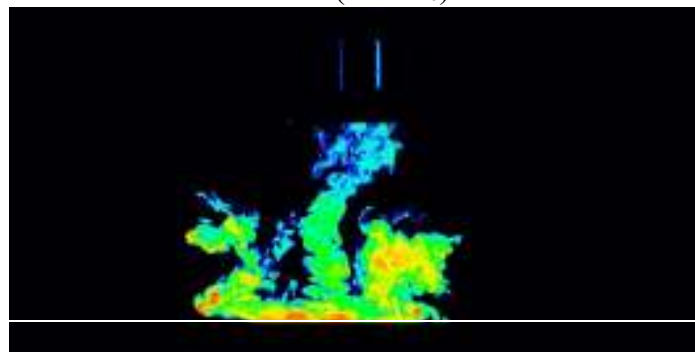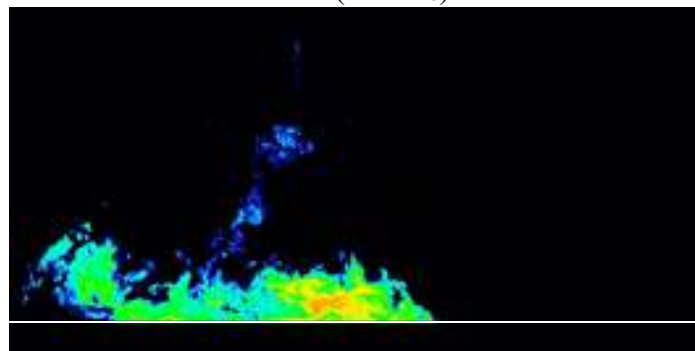
Figure 3.20: Time series of the calibrated PLIF images captured during Test 4 of Group 1 (Q_{pump} = 19.10 L/s, u_t/V_0 = 0.579)

3.3.4.1 Displacement of the outflow in traveling downbursts

To quantify the displacement of traveling downbursts, the central point of the bottom iris gate, at the time of release, was considered as the origin (Figure 3.21), and a vertical line passing through it was used to measure the lateral distance of the right (R_L) and left (R_R) ends of the produced outflow from the origin. In the stationary release experiments, this vertical line is the same as the axis of symmetry of the outflow, thus the values of R_L and R_R are always similar. But in the traveling downburst tests, because of the resultant asymmetrical outflow structure, the above-mentioned distances are not equal at any given time. It should be noted that the distance between the downburst front and the ground (H) was also monitored during each release experiment (based on the method described in Chapter 2-Figure 2.8).
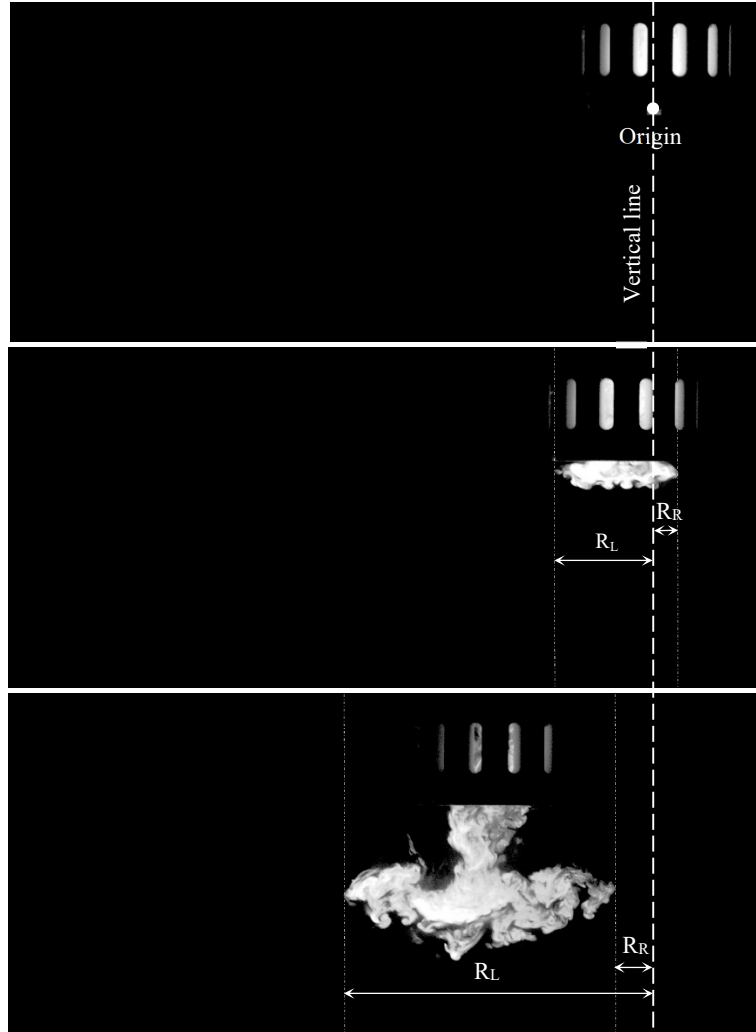
Figure 3.21: Measuring the shape parameters in the traveling downbursts

The dimensionless form of the variations of these geometrical parameters with time for the experiments in Group 3 are illustrated in Figure 3.22(a)-(c), Table 3.11, summarizes the details of these traveling tests.

Table 3.11: Ambient fluid flow and translation velocities for the tests of Group 3

	Test 1	Test 2	Test 3	Test 4
Q_{pump} (L/s)	0	9.15	14.70	19.10
$\bar{u}$ (cm/s)	0	3.60	5.78	7.49
u_t (cm/s)	0	3.87	6.04	8.16
$\bar{u}/V_0$	0	0.298	0.478	0.619
u_t/V_0	0	0.320	0.500	0.675

As can be seen in Figure 3.22(c), for a constant initial release height ($H_0 = 2.38R_0 = 10.5$ cm in Group 3), increasing the environmental flow velocity (from zero to an average value of 7.49 ($0.619V_0$) cm/s) does not change the variations of frontal height with time in a significant way. According to this graph, the touchdown time for the stationary downburst (Test 1) is 2.00 (5.47 T_0) s while all the traveling downbursts (Tests 2-4) impact on the ground at 1.90 (5.20 T_0) s. Such similar trends were also observed for the tests in the other two groups of release experiments in Table 3.4.

Figure 3.22(a) shows how the position of the left end of the downburst outflow varies with time. For the stationary experiment ($u_t/V_0 = 0$), the presented data are identical to those in Figure 3.7(a). As the flow rate increases, the produced downburst also moves in the direction of flow resulting in higher values of R_L compared to the stationary test. On the other hand, the right end of the downburst approaches to the vertical line (see Figure 3.21) and if the environmental shear is strong enough, moves to the left side of the line (Figure 3.22(b)). It should be noted that the R_L and R_R values were considered as positive to the left and right sides of the vertical line, respectively; and as they move to the opposite side, a negative value was assigned.
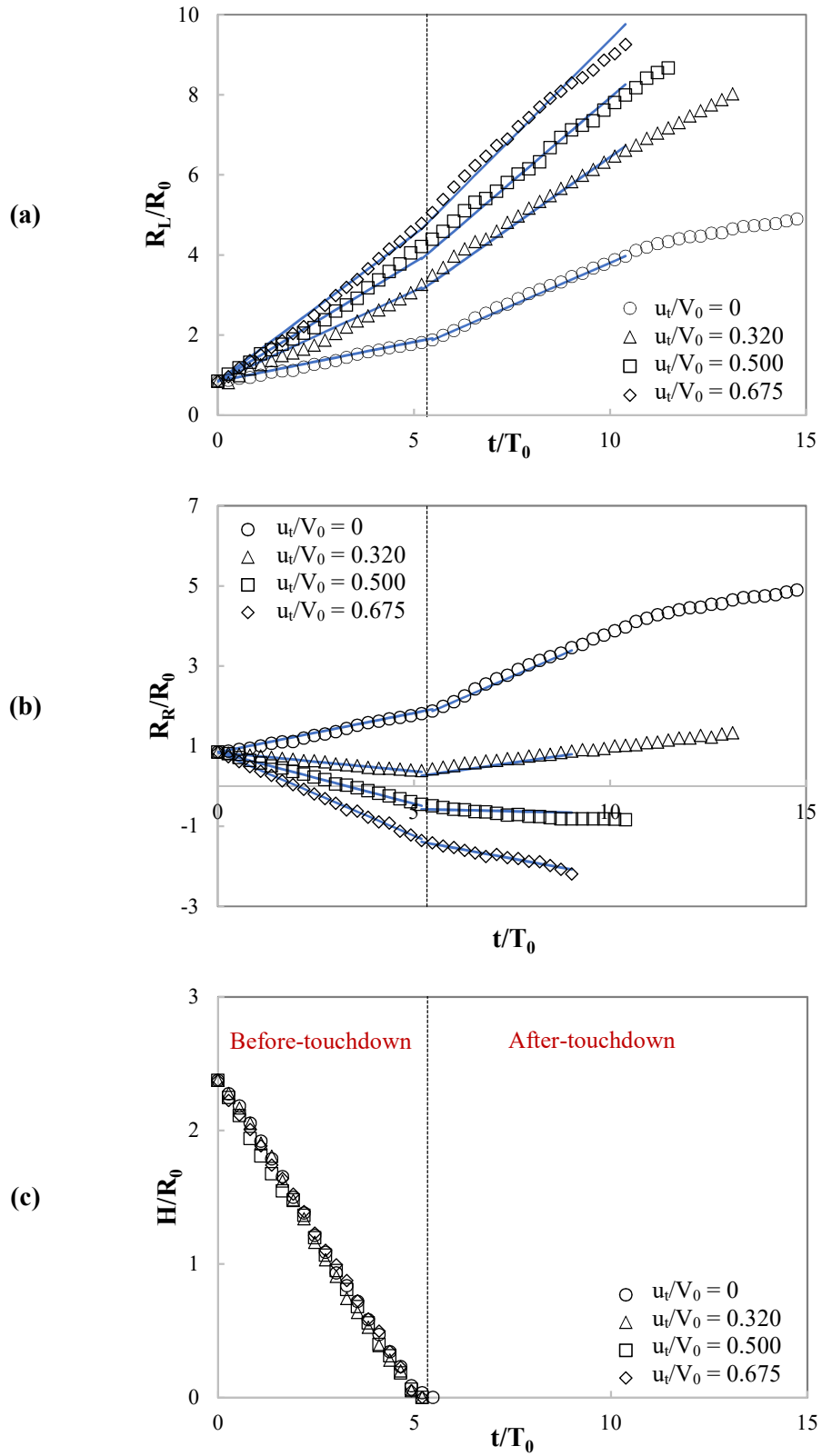
Figure 3.22: Time variations of the shape parameters for the tests in Group 3: (a) R_L/R_0, (b) R_R/R_0 and (c) H/R_0

By quantifying the position of the downburst outflow as a function of time, its width (W) and central point (x_{CP}) can also be determined, Figure 3.23 depicts how these quantities are measured in each PLIF image.
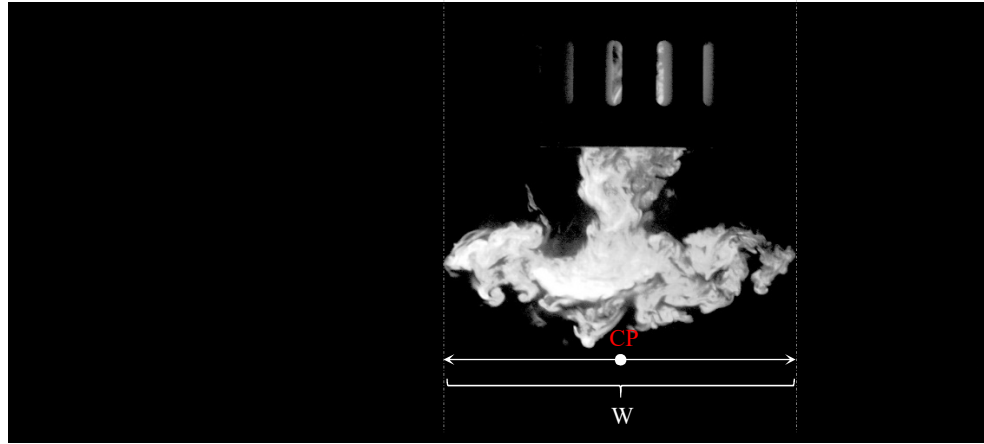
Figure 3.23: Calculating the outflow width and its central point position

In Equations (3.15) and (3.16), the mathematical relationships between theses quantities and shape parameters are presented, and in Figure 3.24(a)-(b), the width and horizontal location of the central point are plotted against the dimensionless time.

$$W = R_L + R_R \tag{3.15}$$

$$x_{CP} = \frac{R_L - R_R}{2} \tag{3.16}$$
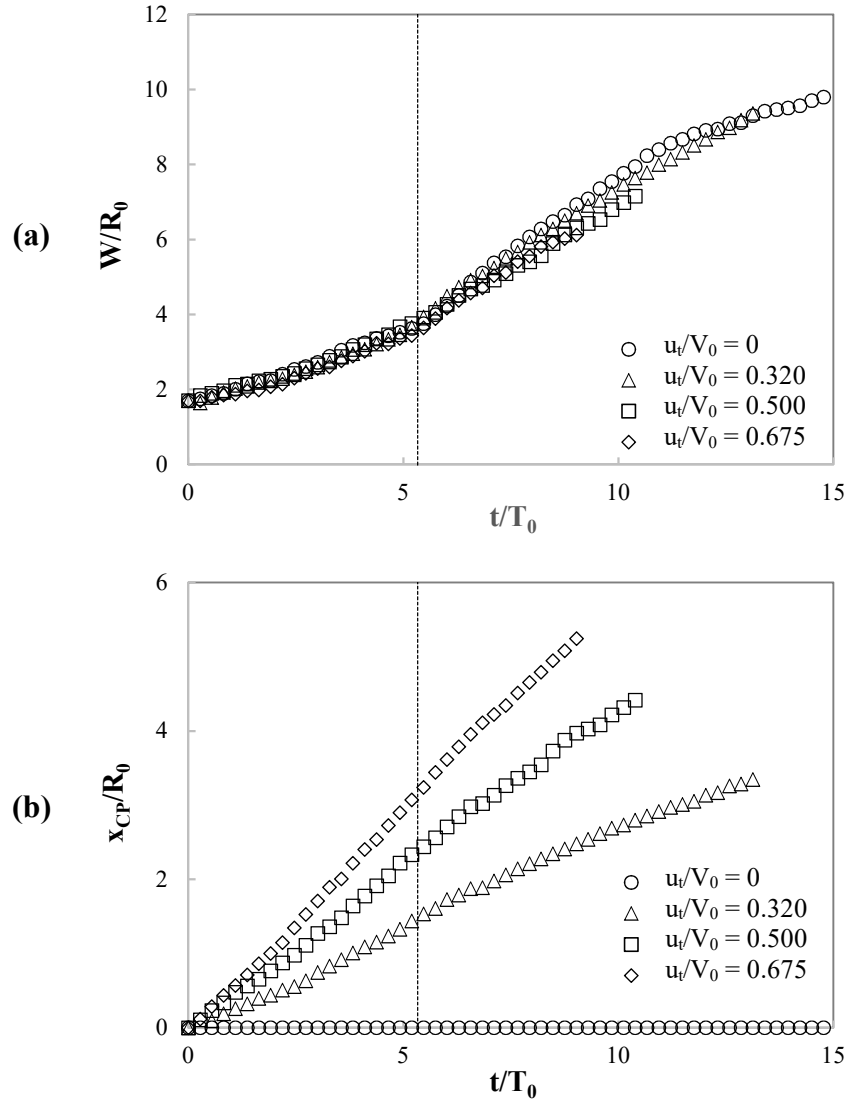
Figure 3.24: Time variations of (a) W and (b) x_{CP} for the tests in Group 3

To investigate the influence of ambient flow velocity on the displacement of the produced downburst, the radial speeds of the outflow front, on both the left and right sides, were calculated for the before and after-touchdown phases. In Table 3.12, these values are presented for the stationary and traveling release experiments in Group 3 (Lines 5-8 and 12-15). The difference between radial front speeds in the before (BT) and after (AT)-touchdown periods are also given in this table (Lines 9 and 16). For the left side of the outflow, this difference decreases from 2.64 cm/s to 0.82 cm/s as the flow rate increase from zero to 19.10 L/s (Line 9), this can also be clearly observed in Figure 3.22(a) where the plot of R_L/R_0 versus t/T_0 approaches a straight line by increasing the flow rate. Thus, it can be said that for the traveling downbursts, the radial front speed for one side of the outflow, which propagates in the direction

98

of ambient fluid flow, is not affected by impact on the ground as much as the radial speed of a stationary downburst. But for the right side of the outflow, according to this table and Figure 3.22(b), the difference between the radial front speeds of the before and after-touchdown phases remains the same (Line 16) suggesting that the radial speed of the side of the outflow which propagates in the opposite direction to the environmental flow is affected by impact on the ground in the same way as a stationary downburst.

To asses the relationship between the radial front speeds of the stationary and traveling downbursts, the average value of ambient flow velocity in the channel for each of the three flow rates used in Tests 2-4 (Line 2) was added to the radial front speed of the stationary release experiment. According to this table, the before-touchdown speed of the left side (line 7) is in a very good agreement with the values resulting from adding the average velocity to the radial speed of the stationary test (Line 10). But for the after-touchdown point, the measured radial speeds (Line 8) are lower than the added values (Line 11). This finding is consistent with the fact that, for the traveling tests, the radial speeds of the left side in the before and after-touchdown phases are very close and their difference decreases with increasing flow rate. For the right side of the outflow, the measured frontal radial speeds for both before and after-touchdown phases (Lines 14 and 15) are in agreement with the added values (Lines 17 and 18). It should be noted that, for the right side which moves in the opposite direction to the channel flow, the average flow velocities were subtracted from the radial front speeds of the stationary downburst.

Based on these results, it can be expected that the width of the outflows in the traveling experiments remains unchanged in the before-touchdown phase. In other words, the ambient flow affects the left and right sides of the outflows in the same way and there is no total expansion or contraction in this phase. Figure 3.24(a) shows how the outflow width in all the stationary and traveling downbursts are the same before impacting on the ground. For the after-touchdown phase, the outflow width is slightly lower in the traveling experiments which can be explained by the weak influence of ground impact on the radial front speed of the left side.

The rate of the horizontal displacement of the outflow central point was also calculated using the data in Figure 3.24(b) and presented in Table 3.12. It is obvious that for the stationary downburst, the outflow is symmetrical and the central point is stationary as well, but for the

traveling tests, this point moves in the direction of environmental flow. The displacement speed is close to the average flow velocity in the channel before impacting on the ground (Line 19) and slightly decreases in the after-impact phase (Line 20).

Table 3.12: Radial front speeds for the traveling downbursts in Group 3

			Test 1	Test 2	Test 3	Test 4
	1	Q_{pump} (L/s)	0	9.15	14.70	19.10
	2	$\bar{u}$ (cm/s)	0	3.60	5.78	7.49
	3	$\dfrac{u_t}{V_0}$	0	0.320	0.500	0.675
	4	$\dfrac{\delta_{x=1.9\,m}}{H_0}$	0	0.296	0.233	0.191
	5	$\dfrac{1}{V_0}\dfrac{\overline{dR_L}}{dt}\Big|_{BT}$	0.196	0.466	0.638	0.778
	6	$\dfrac{1}{V_0}\dfrac{\overline{dR_L}}{dt}\Big|_{AT}$	0.414	0.589	0.721	0.846
	7	$\dfrac{\overline{dR_L}}{dt}\Big|_{BT}$ (cm/s)	2.37	5.63	7.71	9.41
Left	8	$\dfrac{\overline{dR_L}}{dt}\Big|_{AT}$ (cm/s)	5.01	7.12	8.72	10.23
	9	$\dfrac{\overline{dR_L}}{dt}\Big|_{AT} - \dfrac{\overline{dR_L}}{dt}\Big|_{BT}$	2.64	1.49	1.01	0.82
	10	$\dfrac{\overline{dR_L}}{dt}\Big|_{BT,Test1} + \bar{u}$	2.37	5.97	8.15	9.86
	11	$\dfrac{\overline{dR_L}}{dt}\Big|_{AT,Test1} + \bar{u}$	5.01	8.61	10.79	12.5
	12	$\dfrac{1}{V_0}\dfrac{\overline{dR_R}}{dt}\Big|_{BT}$	0.196	-0.093	-0.253	-0.418
	13	$\dfrac{1}{V_0}\dfrac{\overline{dR_R}}{dt}\Big|_{AT}$	0.414	0.115	-0.073	-0.176
	14	$\dfrac{\overline{dR_R}}{dt}\Big|_{BT}$ (cm/s)	2.37	-1.12	-3.06	-5.06
Right	15	$\dfrac{\overline{dR_R}}{dt}\Big|_{AT}$ (cm/s)	5.01	1.39	-0.88	-2.13
	16	$\dfrac{\overline{dR_R}}{dt}\Big|_{AT} - \dfrac{\overline{dR_R}}{dt}\Big|_{BT}$	2.64	2.51	2.18	2.93
	17	$\dfrac{\overline{dR_R}}{dt}\Big|_{BT,Test1} - \bar{u}$	2.37	-1.23	-3.41	-5.09
	18	$\dfrac{\overline{dR_R}}{dt}\Big|_{AT,Test1} - \bar{u}$	5.01	1.41	-0.77	-2.45
	19	$\dfrac{\overline{dx_{CP}}}{dt}\Big|_{BT}$ (cm/s)	0	3.38	5.39	7.23
	20	$\dfrac{\overline{dx_{CP}}}{dt}\Big|_{AT}$ (cm/s)	0	2.86	4.85	6.70

One conclusion that can be drawn from this analysis is that in the traveling downburst experiments, the environmental flow that embodies the outcoming dense fluid displaces its path without deforming the vortex in a significant way. In other words, the size of the downburst event does not change with the ambient velocity, but the flow speeds in the two sides of the downburst are affected accordingly. In this study the velocity fields of the simulated release experiments were not measured making it impossible to comment of the influence of ambient flow on the radial velocity magnitudes. Instead, the role of the environmental flow on the dislocation of the event footprint was examined. However, in studies by Hjelmfelt (1987) and Holmes and Oliver (2000), the information on the velocity field of real downburst events were analysed and the environmental flow velocity was subtracted from the asymmetric wind velocity field of the moving downbursts. The results showed that after subtraction, a symmetric velocity field was obtained. This observation of the ambient flow effect on the wind velocity field is similar to the results of this study regarding the effect of ambient flow on the displacement of downburst event. Although the velocities were not measured, the results support the idea that the traveling downbursts are embedded in an external environmental flow and their pattern assimilates one resulting from addition of two vector fields.

With that said, finding a mathematical expression for correlating the outflows of all the stationary and traveling experiments (Tests 1-4) with the translation velocity can help in summarizing the above discussion. Based on the results presented in Table 3.12, a linear relationship (Equation (3.17)) was employed and its coefficients and constants were obtained by fitting the data in the before and after-touchdown phases for the left and right sides of the downbursts (Table 3.13). in Figure 3.22(a)-(b), the solid lines represent the results of such correlations.

$$\frac{R_{L/R}}{R_0} = \left(a + b\left(\frac{u_t}{V_0}\right)\right)\frac{t}{T_0} + c \tag{3.17}$$

Table 3.13: Correlating the data from Figure 3.22(a)-(b) with the translational velocity of the release cylinder

	a	b	c	R-squared
Left-BT	0.196	0.793	0.848	0.989
Right-BT	0.196	-0.908	0.848	0.998
Left-AT	0.426	0.825	-0.456	0.991
Right-AT	0.426	-0.898	-0.456	0.997

According to this table, the values of a in the before and after-ground impact periods are 0.196 and 0.426, respectively. These quantities are equal to $\frac{1}{V_0}\frac{d\bar{R}}{dt}\Big|_{BT}$ and $\frac{1}{V_0}\frac{d\bar{R}}{dt}\Big|_{AT}$ for the stationary downburst (see Table 3.6). Thus, Equation (3.17) originally describes the radial propagation speeds of Test 1 ($u_t/V_0 = 0$) and incorporates the translation effect by adding the term $b(u_t/V_0)$ to the coefficient of t/T_0 for the traveling experiments.

3.3.4.2 Entrainment measurements

By calibrating the PLIF images, the concentration of fluorescent dye in each pixel can be quantified and related to the maximum dye concentration at the beginning of the release experiments. Thus, variations of the average dye concentration in the expanding outflow can be used as an indication of how the dense ($C_{relative}=1$) and ambient ($C_{relative}=0$) fluids are mixed together during a downburst release test. Determining the degree of such mixing shows the rate of the entrainment of ambient fluid by the descending and radially spreading dense fluid parcel. To calculate the average relative concentration ($\bar{C}_{relative}$) for each calibrated image, the following steps were taken:

(1) The border separating the downburst and its environment was defined.
(2) Number of pixels within the border (N_p) was counted and the total area (A) was calculated.
(3) The relative concentration was integrated for all the pixels inside the border.
(4) The result was divided by the total area to get the average relative concentration.

As an example, Figure 3.25 illustrates the outflow border lines in PLIF images taken at different times following the opening of the release cylinder for one of the stationary tests. The total area inside the border was computed by multiplying the number of pixels within the border by the area of each pixel (a_p) (Equation (3.18)). By having the downburst area in each image, the average relative concentration can also be calculated for that image (Equation (3.19)).

$A = 53.4 \text{ cm}^2$

$A/R_0^2 = 2.73$

t = 0.9 (2.46 T_0) s

$A = 105.9 \text{ cm}^2$

$A/R_0^2 = 5.42$

t = 1.7 (4.65 T_0) s

$A = 174.05 \text{ cm}^2$
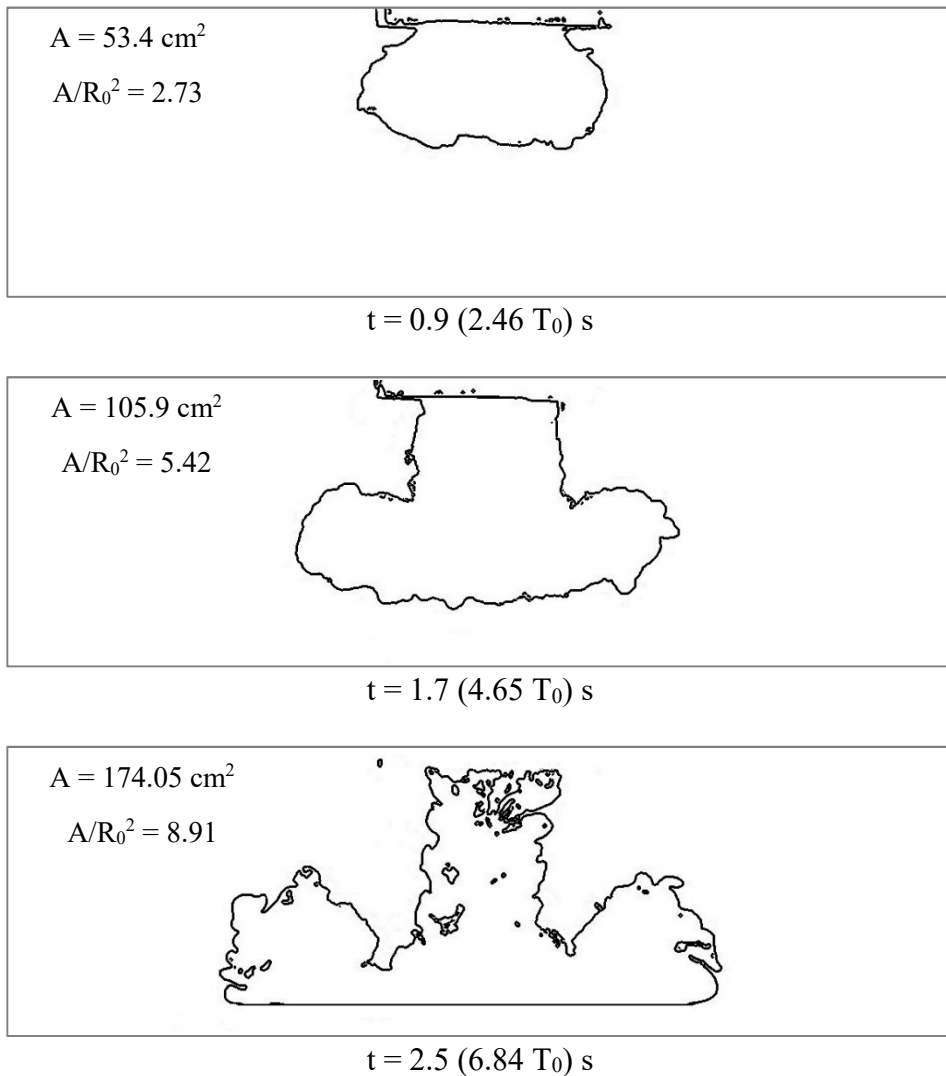
$A/R_0^2 = 8.91$

t = 2.5 (6.84 T_0) s

Figure 3.25: Calculation of the area of the produced outflows

$$A = N_p \times a_p = N_p \times \frac{\text{area of the field of view}}{\text{number of pixels in each image}}$$ (3.18)

103

$$\overline{C}_{relative} = \frac{\int C_{relative}dA}{A} = \frac{\sum_{i=1}^{N_p} C_{relative\ at\ pixel\ i} \times a_p}{A} \tag{3.19}$$

In Figures 3.26 and 3.27, the outflow area and average relative concentration are plotted against the dimensionless time for the Tests 1-4 in Group 2. In these set of experiments, the initial release height and ground touchdown time are 12.5 cm and 2.3 (6.29T_0) s, respectively. According to Figure 3.26, following the opening of the release mechanism, the area continuously increases, but the rate of such increase is higher from t = 0 s to t = 2.60 (7.11T_0) s and, after that, it grows at a slower rate. The average relative concentration, on the other hand, remains almost constant from t = 0 s to t = 1.90 (5.20T_0) s and decreases after that (Figure 3.27).

It is obvious that after quickly opening the iris gates and wall slots in the release cylinder, the volume of the descending dense fluid increases and its density decreases due to the mixing with lighter ambient fluid. The observation that the average value of relative concentration does not change until 1.90 (5.20T_0) s can be attributed to the specification of the new release cylinder (Cylinder 2). As discussed in Chapter 2 (part 2.3.2), the dense fluid from Cylinder 2 is more mixed and less homogeneous compared to the dense fluid from a release cylinder with solid walls. Thus, its initial average concentration is lower than unity (around 0.94) and, because of its slower downward movement, the concentration decrease does not start right after the opening of the mechanism.

Another important observation is that the area and average relative concentration of travelling downbursts, at any given time, are equal to the corresponding values in a stationary release experiment. In other words, ambient flow velocity does not influence the total area of the event and the degree of entrainment of ambient fluid.

It should be noted that these observations apply to a vertical plane parallel to the environmental flow direction (see the laser sheet in Figure 3.5). Thus, drawing conclusions about the general behaviour of the downburst, which is a 3D event, using the current data is not possible. This argument also applies to the radial front speeds of the traveling experiments that were discussed in the previous part. Another important point regarding the predictions of the flow field of natural downbursts based on the results of present study is the characteristics of the simulated

ambient flow and boundary layer in the laboratory. As explained in part 3.3.3.2.2, the channel flow for these traveling experiments is laminar, and, unlike natural events, mixing of ambient and downburst fluids due to turbulence effects is absent for the present release experiments.
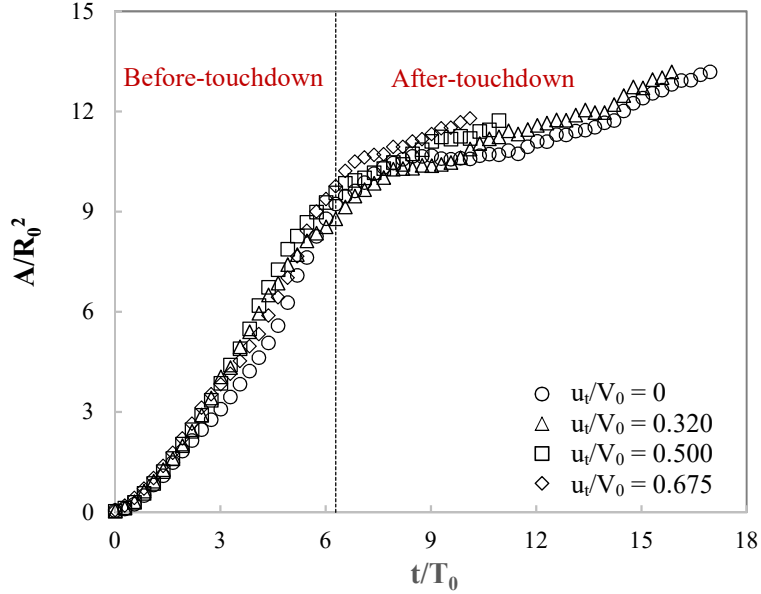

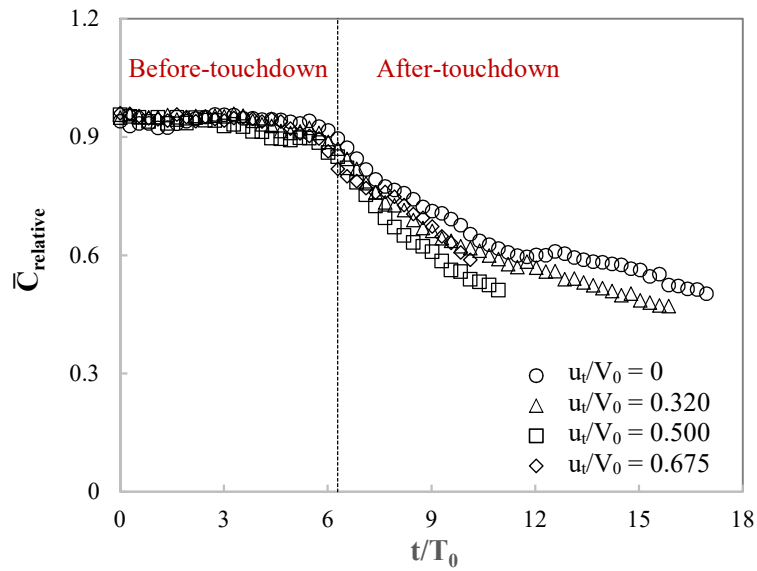**Figure 3.26: Time variations of the area of the produced outflows in Group 2**

Figure 3.27: Time variations of the average relative concentration in the produced outflows in Group 2

3.4   Summary

In this chapter, the flow fields of stationary and travelling downbursts were compared and the influence of the environmental flow velocity on the behaviour of the resultant outflow was quantified. For the first time, the specifications of real downburst events (storm translation and wind field in the ambient environment) were implemented in the laboratory. In this regard, a hydraulic flume was utilized to simulate the environmental flow and the velocity field within this channel was characterized using hot film anemometry. The findings of these traveling downburst release experiments in the new setup can be summarized as follows:

(1) In the after-touchdown period, the stationary downburst in the flume propagates with slightly higher speed compared to the stationary downburst in the smaller tank.

(2) The weakened phase of the after-touchdown period of the stationary downburst in the flume can be described using the gravity current formulations in the inertial phase.

(3) The vertical speed of the downburst front remains unchanged for different ambient flow velocities in the flume.

(4) The left and right sides of the traveling downbursts displace within the ambient environment according to the strength of the background flow.

(5) The area of the downburst in the captured PLIF images increases with time while the average relative concentration decreases.

(6) The value of initial release height does not affect the general behaviour of traveling downbursts.

3.5   References

Alahyari AA (1995) Dynamics of laboratory simulated microbursts. PhD Dissertation, University of Minnesota

Alahyari AA, Longmire EK (1994) Particle image velocimetry in a variable density flow: application to a dynamically evolving microburst. Exp Fluids 17:434-440

Bruun HH (1995) Hot-wire anemometry: Principles and signal analysis. Oxford University Press, Oxford, UK

Burlando M, Romanic D, Solari G, Hangan H, Zhang S (2017) Field data analysis and weather scenario of a downburst event in Livorno, Italy, on 1 October 2012. Mon Wea Rev 145:3507-3527

Cantero MI, Lee JR, Balachandar S, Garcia MH (2007) On the front velocity of gravity currents. J Fluid Mech 586:1-39

Chay MT, Letchford CW (2002) Pressure distributions on a cube in a simulated thunderstorm downburst-Part A: stationary downburst observations. J Wind Eng Ind Aerodyn 90:711-732

Crimaldi JP (2008) Planar laser induced fluorescence in aqueous flows. Exp Fluids 44:851-863

Duncan WJ, Thom AS, Young AD (1970) Mechanics of fluids, 2nd edn. American Elsevier Publication Company, New York, USA

Eilts MD, Doviak RJ (1987) Oklahoma downbursts and their asymmetry. J Climate Appl Meteor 26:69-78

Elawady A, El Damatty A (2016) Longitudinal force on transmission towers due to non-symmetric downburst conductor loads. Eng Struct 127:206-226

Fujita TT (1985) The downburst. The University of Chicago Press, Chicago, USA

Fujita TT (1986) DFW downburst. The University of Chicago Press, Chicago, USA

Hjelmfelt MR (1987) Structure and life cycle of microburst outflows observed in Colorado. J Appl Meteorol 27:900-927

Holmes JD, Oliver SE (2000) An empirical model of a downburst. Eng Struct 22:1167-1172

Hultmark M, Smits AJ (2010) Temperature corrections for constant temperature and constant current hot-wire anemometers. Meas Sci Thechnol 21:1-4

Huppert HE (2006) Gravity currents: a personal perspective. J Fluid Mech 554: 299-322

Huppert HE, Simpson JE (1980) The slumping of gravity currents. J Fluid Mech 99: 785-800

Letchford CW, Chay MT (2002) Pressure distributions on a cube in a simulated thunderstorm downburst. Part B: moving downburst observations. J Wind Eng Ind Aerodyn 90:733-753

Lundgren TS, Yao J, Mansour NN (1992) Microburst modelling and scaling. J Fluid Mech 239:461-488

Mason MS, Letchford CW, James DL (2005) Pulsed wall jet simulation of a stationary thunderstorm downburst, Part A: Physical structure and flow field characterization. J Wind Eng Ind Aerodyn 93:557–580

Mason MS, Wood GS, Fletcher DF (2009) Numerical simulation of downburst winds. J Wind Eng Ind Aerodyn 97:523-539

Nogueira HIS, Adduce C, Alves E, Franca MJ (2014) Dynamics of the head of gravity currents. Environ Fluid Mech 14:519-540

Orf LG, Anderson JR, Straka JM (1996) A three-dimensional numerical analysis of colliding microburst outflow dynamics. J Atmos Sci 53:2490-2511

Orf LG, Anderson JR (1998) A numerical study of traveling microbursts. Mon Wea Rev 127:1244-1258

Orf LG, Kantor E, Savory E (2012) Simulation of a downburst-producing thunderstorm using a very high-resolution three-dimensional cloud model. J Wind Eng Ind Aerodyn 104-106:547-557

Orf LG, Oreskovic C, Savory E, Kantor E (2014) Circumferential analysis of a simulated three-dimensional downburst-producing thunderstorm outflow. J Wind Eng Ind Aerodyn 135:182-190

Perry AE (1982) Hot-wire anemometry. Oxford University Press, Oxford, UK

Pistotnik G, Holzer AM, Kaltenbock R, Tschannett S (2010) An F3 downburst in Austria-A case study with special focus on the importance of real-time site surveys. Atmos Res 100: 565-579

Rouse H, Hassan MM (1949) Cavitation free inlets and contractions. Mech Eng 71: 213-216

Rumble JR (ed) (2017) CRC handbook of chemistry and physics, 98th edn. CRC press, Boca Raton, USA

Sengupta A, Sarkar PP (2008) Experimental measurement and numerical simulation of an impinging jet with application to thunderstorm microburst winds. J Wind Eng Ind Aerodyn 96: 345-365

Shehata AY, El Dammatty AA, Savory E (2005) Finite element modeling of transmission line under downburst wind loading. Finite Elem Anal Des 42:71-89

Sher D, Woods AW (2015) Gravity currents: entrainment, stratification and self-similarity. J Fluid Mech 784:130-162

Vermeire BC, Orf LG, Savory E (2011) Improved modelling of downburst outflows for wind engineering applications using a cooling source approach. J Wind Eng Ind Aerodyn 99:801-814

White FM (2016) Fluid mechanics, 8th edn. McGraw-Hill Education, New York, USA

Yao J (1994) Experiments on microbursts. PhD Dissertation, University of Minnesota

Yao J, Lundgren TS (1996) Experimental investigation of microbursts. Exp Fluids 21:17-25

Zhang Y, Hu H, Sarkar PP (2013) Modeling of microburst outflows using impinging jet and cooling source approaches and their comparison. Eng Struct 56: 779-793

<div align="center">Chapter 4</div>

4 Conclusions and Recommendations for Future Work

This chapter summarizes the findings of the present research study and gives recommendations for the future investigations of downbursts based on the two-fluid model.

4.1 Summary and conclusions of the current study

In this study, thunderstorm downbursts, which are extreme weather events initiated by the negative buoyancy, were experimentally simulated in the laboratory using the two-fluid model. In general, the experimental setup of the two-fluid model consists of a volume holding the dense fluid and a less dense ambient environment in which this volume is submerged. Two liquids with different densities were used to, respectively, represent the descending mass of cold air and the ambient environment surrounding it. This research work aimed to address the shortcomings and limitations of previous experimental studies of downbursts based on the two-fluid model. The important findings and accomplishments of this work are as follows:

(1) The first part of this study was focused on the improvement of the features of a cylindrical structure used by previous researchers for holding the dense solution. Iris gates were installed at the top and bottom of the cylinder, the quick and consistent operation of these irises helped in overcoming the repeatability issues associated with previous release mechanisms. Moreover, the solid wall of the cylinder was re-designed to introduce a porosity of 25%, this was an attempt to partially eliminate the wall effect as in real downburst events, there is no wall separating the two fluids. The downburst release experiments of the first part of this study (Chapter 2) were conducted using two different cylinder designs with wall porosities of zero (Cylinder 1) and 25% (Cylinder 2) and a small tank filled with the ambient solution. Since, the ambient environment was quiescent, these experiments were called the stationary downbursts.

   (a) Planar laser induced fluorescence technique was used to visualize the evolution of the simulated downbursts in a vertical plane passing through the middle of the release mechanism.

   (b) The influence of cylinder wall elimination was studied by comparing the flow fields of downbursts produced by the two release cylinders. The outflow from Cylinder 2

<div align="center">110</div>

was less homogeneous and more mixed and had a 23.2% lower descending speed compared to the outflow of Cylinder 1. This suggests that even eliminating a quarter of cylinder solid wall makes a significant impact on the resultant flow field, thus, Cylinder 2 was utilized for conducting the rest of experiments of this study.

(c) The effect of density difference between the two fluids on the evolution of downbursts was investigated using three different $\Delta\rho/\rho_a$ values (1.95%, 3.37% and 5.51%), and similar behaviours were observed when the scalar fields were nondimensionalized using the previously developed length and time scales (R_0 and T_0).

(d) To assess the impact of the height of the thunderstorm cloud base on the produced downbursts, various initial release heights ($2.42R_0$, $3.26R_0$ and $3.62R_0$) were employed and the patterns of downburst radial propagation were compared for the resultant outflows. For the initial heights used in this study, similar vertical and radial front speeds were measured in the before and after-touchdown periods, and changing the release height only affected the ground impact time.

(2) In the previous studies and, also in the first part of the current work, a tank filled with ambient solution was utilized to represent the environment in which the downburst occurs. But in real conditions, the downburst producing thunderstorm clouds are not always motionless and there is a non-zero background velocity field in the sub-cloud environment. In the second part of this research (Chapter 3), experimental setup was fundamentally modified to incorporate the environmental flow and cloud translation conditions. In this regard a hydraulic channel equipped with a trolley system holding the release cylinder (Cylinder 2) was used. Three groups of experiments with different initial release heights (Group 1-3) were conducted, and four different environmental flow velocities (Tests 1-4) were used in each group of experiments. Because of the ambient fluid flow in the channel and the translation of release mechanism, these experiments were called the traveling downbursts.

(a) Both ambient flow rate and trolley speed in the first release test (Test 1) of each group were zero. The purpose of conduction such stationary experiments in the flume was to compare the outflows produced in a small tank and in the larger environment of the hydraulic flume and examine the wall confinement effect.

111

Similar descending and radial propagation behaviours were observed in the before-touchdown phase, and a 13.5% increase was reported for the after-touchdown radial front propagation speed for the downburst in the flume.

(b) The after-touchdown phase of the stationary downbursts in he flume was compared with the gravity currents, and the weakened part of it (starting at $t = 11.21T_0$) was correlated with the gravity current formula in the inertial phase.

(c) For the traveling release tests in each group (Tests 2-4), different values of ambient fluid flow rate (9.15 L/s, 14.70 L/s and 19.10 L/s) were used. To specify the longitudinal, vertical and lateral velocity profiles in the channel, a hot film anemometer was employed and the results were used in the selection of the appropriate trolley translation velocities and also in the analysis of the displacement of traveling downbursts.

(d) Time variations of the positions of both left and right ends of the produced outflows were determined, and the width and central point of the downbursts were measured. Such data were used to correlate the dislocation of the simulated traveling downbursts with the trolley translational velocity.

(e) A MATLAB code was used to calculate the outflow area in each PLIF image and the average relative concentration within this area. A continuous increase was observed for the downburst area, although the rate of increase was not constant and dropped at $t = 7.11T_0$. On the other hand, the average relative concentration, which was an indication of the entrainment of the ambient solution by the downburst, remained constant until $t = 5.20T_0$ and decreased after that.

4.2 Recommendations for future research

The new experimental apparatus designed in the present research work can be utilized for further explorations of the downburst phenomenon. In this regard, the following investigations are recommended:

(1) Employing the PLIF technique to study the development of the descending downburst in a horizontal plane. This can be done by forming a horizontal laser sheet and changing the camera orientation accordingly. Access to the such information is of great importance to the study of traveling downbursts as their flow field is not symmetric.

(2) The hydraulic flume and trolley system, deigned in the present research work, allow the experimental simulation of downburst lines. A downburst line consists of two or more downburst events that have small spatial or temporal separations. It is obvious that such events can result in larger footprints and higher wind velocities. Multiple release mechanisms can be attached to the trolley and their spatial proximity can be adjusted by changing the distance between the cylinder holders. Different values of temporal separation can also be assigned by modifying the LabVIEW code for the downburst lines.

(3) In this study, the scalar field of the downbursts were measured using the PLIF method. The velocity field of the stationary and traveling downbursts (in the form of a singular downburst or a downburst line) can be characterized using the Particle image velocimetry (PIV) technique. The data from such measurements can be used to specify the influence of ambient flow velocity and occurrence of more than one downburst on the resultant wind speeds.

Appendix 1: The LabVIEW VI front panel for controlling the operation of the release mechanism and trolley system
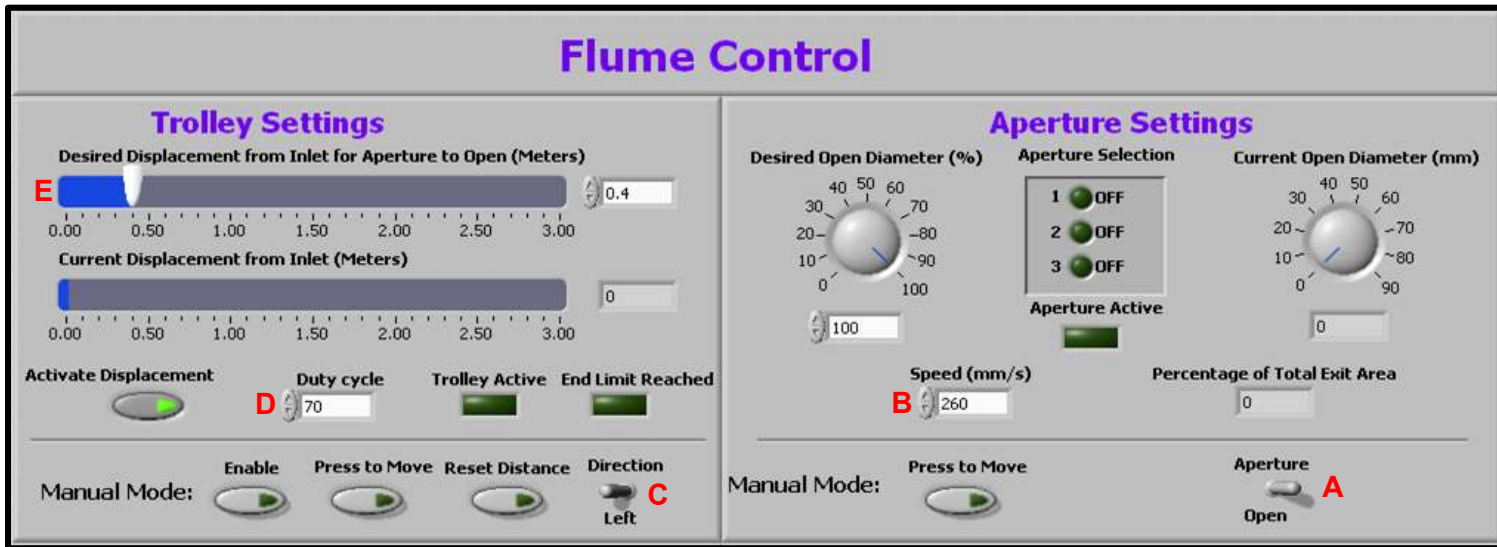
This part controls:

1- Trolley movement direction **(C)**
2- Trolley speed **(D)**
3- The distance of dropping the dense liquid **(E)**

This part controls:

1- Opening/closing of the release cylinder **(A)**
2- The speed of opening/closing **(B)**

Curriculum Vitae

Name:	Roghayyeh Babaei koli

Post-secondary Education and Degrees:

Western University, London, Ontario, Canada
MSc (2016 – 2018)
Thesis Title: Experimental Simulation of Density-Driven Thunderstorm Downbursts

Amirkabir University of Technology, Tehran, Iran
PhD (2010 – 2015)
Thesis Title: Hydrodynamic Characterization of Activated Sludge Bioreactors Using Electrical Resistance Tomography

Amirkabir University of Technology, Tehran, Iran
MSc (2007 – 2010)
Thesis Title: The Study of Styrene Biodegradation Kinetics in Synthetic Petrochemical Wastewaters Using an Industrial Activated Sludge

Amirkabir University of Technology, Tehran, Iran
BSc (2003 – 2007)
Undergraduate Project: Applications of Bio-Nanotechnology in Medical Sciences

Publications:

Babaei R, Boakdarpour B, Ein-Mozaffari F (2015) Analysis of gas phase behavior and mixing performance in an activated sludge bubble column using electrical resistance tomography. Chem Eng J 279: 874-884

Babaei R, Boakdarpour B, Ein-Mozaffari F (2015) The use of electrical resistance tomography for the characterization of gas holdup inside a bubble column bioreactor containing activated sludge. Chem Eng J 268: 260-269

Babaee R, Boakdarpour B, Nasernejad B, Fallah N (2015) Kinetics of styrene biodegradation in synthetic wastewaters using an industrial activated sludge. J Hazard Mater 184: 111-117

Teaching Assistantship:	Kinematics and Dynamics of Machines (Fall 2016)
	Introduction to Fluid Mechanics & Heat Transfer (Winter 2017)
	Kinematics and Dynamics of Machines (Fall 2017)
Work Experience:	**Advanced Research Company**, Tehran, Iran
	(2010 – 2011)
	Project manager for the study of septage treatment in cities of Rasht and Anzali
	Pardazesh Educational Institute, Tehran, Iran
	(2008 – 2009)
	Prepared an electronic educational medium for Chemical Engineering courses (Heat Transfer, Thermodynamics, Reactor design and Process Control)
	Iranian Oil Pipeline and Telecommunication Company (a branch of National Iranian Oil Refining and Distribution Company), Tehran, Iran
	Summer Intern (2007)